Search for Supersymmetric Particles from Z Decays

by

Susan Mary Gascon-Shotkin

M.S. (Physics), Michigan State University (1989)
B.S. (Industrial Engineering and Operations Research), School of
Engineering and Applied Science, Columbia University (1979)
B.A. (Mathematics), Barnard College, Columbia University (1978)

()

Submitted to the Department of Physics
in partial fulfillment of the requirements for the degree of

Doctor of Philosophy

at the

MASSACHUSETTS INSTITUTE OF TECHNOLOGY

January, 1995

Author ....
Department of Physics
Januarv 9. 1995

Certified by ....
Min Chen
Professor
Thesis Supervisor

Accepted by ....
George F. Koster
Chairman, Departmental Committee on Graduate Students
Department of Physics

Search for Supersymmetric Particles from Z Decays
by
Susan Mary Gascon-Shotkin

Submitted to the Department of Physics
on January 9, 1995, in partial fulfillment of the
requirements for the degree of
Doctor of Philosophy

Abstract

Using data recorded by the L3 detector at LEP during 1991, 1992 and 1993, corresponding to 67.9 pb^{-1} of integrated luminosity at c.m.s. energies around the Z pole ($\sim$ 1.9 million Z decays), a search for supersymmetric particles, in particular the two lightest neutralinos, χ and χ', via the reactions $e^+e^- \longrightarrow Z \to \chi\chi'$ and $e^+e^- \longrightarrow Z \to \chi'\chi'$ has been performed. The assumption is made that the χ' decays into a stable and only weakly-interacting (hence invisible) χ plus a fermion pair via $\chi' \longrightarrow \chi + Z^*$, $Z^* \longrightarrow f\bar{f}$. The signature searched for is an electron, muon or hadronic jet pair or monojet recoiling against isolated missing energy and significant missing transverse momentum. No significant excess of signature events over predicted rates from Standard Model background processes has been found in the data sample. Model-independent limits at 95% confidence on the branching ratios of Z into neutralinos of a few 10^{-5} have been set, with maximum values at $Br(Z \to \chi\chi') < 5.5 \times 10^{-5}$ and $Br(Z \to \chi'\chi') < 5.2 \times 10^{-5}$.

These model-independent results have been interpreted in the context of the Minimal Supersymmetric Standard Model (MSSM), currently the most widely-accepted specific model of supersymmetry. The theory has been excluded for triplet points $(M, \mu, \tan\beta)$ in the MSSM parameter space where either a) The number of MSSM-predicted Z decays into neutralinos exceeds the experimentally-determined Poisson upper limit at 95% confidence or b) the MSSM-predicted width from either all Z decays into neutralinos or those into only invisible final states exceeds the current L3 upper limits on $\Delta\Gamma_Z(37.5$ GeV) or $\Delta\Gamma_{inv}(15$ GeV), respectively. For $\tan\beta \geq 4$ the MSSM has been totally excluded at LEP I energies. Lower limits at 95% confidence on the neutralino masses m_χ and $m_{\chi'}$ have been established for $\tan\beta \geq 2$. These are, for $\tan\beta = 2, 4, 8$ respectively, ($m_\chi > 20$ GeV; $m_{\chi'} > 44$ GeV), ($m_\chi > 25$ GeV; $m_{\chi'} > 53$ GeV), and ($m_\chi > 26$ GeV; $m_{\chi'} > 54$ GeV).

Thesis Supervisor: Min Chen
Title: Professor

Acknowledgments

In order to adequately thank all the many people who have given me their help and support, I would need to write a volume at least as long as this thesis. I hope that those who read the relatively few words that follow will realize that each one that appears on the page represents at least a hundred more that have been spoken from the heart at some point or another.

First, I would like to thank my thesis advisor, Prof. Min Chen, for his overall guidance and broad knowledge of physics, for the opportunity to do research and development on liquid xenon electromagnetic calorimetry, for his patient teaching of his methodology of physics analysis, and most importantly, for helping me to become more independent and self-sufficient in physics.

I would like to express my thanks to Prof. S.C.C. Ting for his suport and encouragement during my five years at MIT and at CERN. His scientific insight and intuition, and his ability to organize experiments and motivate people have been at the heart of the L* and L3 collaborations, of which I consider it a privelege to have been a part. He is someone for whom I hold a great respect.

I thank Prof. Ulrich Becker for his guidance and support as a teacher, supervisor of my work on the L3 Forward/Backward Muon Chambers, and finally as a member of my thesis committee. His combination of a deep understanding of physics, innovative ideas, thorough work and painstaking attention to detail have resulted in extremely successful groundbreaking particle detectors.

The remarkably capable and diversified group of people with whom I worked at MIT and whom I then followed to CERN are very special to me. I would like to thank Dr. Tiesheng Dai for helping me with everything from field theory to understanding and working on the muon trigger to valuable physics discussions. Special thanks to Profs. Gregor Herten, Yuan-Hann Chang, Bing Zhou, Bolek Wyslouch and H.S. Chen for getting me started in the fundamentals of physics analysis,patiently entertaining my numerous questions and being a source of moral support. I would like to also thank Drs. Joe Burger and Alexei Lebedev for a productive and challenging work environment and for sharing their extensive knowledge during the installation of the first set of forward/backward muon chambers. In particular, I have been very thankful for the comeradeship and support of my MIT classmates who later became colleagues: Drs. Soo Chung, André Rubbia and Miltos Sarakinos.

I would like to express my gratitude to the leaders of the L3 New Particle Search group, past and present: Prof. Jianming Qian and Drs. Sergey Shevchenko and Yannis Karyotakis, the "godfathers" of this thesis. I appreciated their guidance and greatly benefitted from their immense knowledge and breadth of experience. I would also like to express a special thank-you to Dr. Marta Felcini, whose talent as a physicist and willingness to talk physics at any hour were only rivaled by her sincerity as a friend. I am also grateful to my other colleagues in the NP group: Drs. Rudolf Starosta, Alfons Weber, Vitali Shoutko, Anwarul Hasan, Jingbo Ye, Prof. Jerry Busenitz and also Abdel Boucham. Through them I really started to learn the meaning of scientific collaboration, and I don't think this thesis would have been completed without their help. I also appreciated fruitful and constructive discussions with Jean-

Table of Contents

List of Tables

Chapter 1

Introduction

Since their introduction in the 1960's by Glashow, Weinberg and Salam [1-1], the electroweak and quantum chromodynamics (QCD) theories of particle physics (together commonly known as the "Standard Model") have enjoyed enormous sucess due to experimental confirmation of many of their predictions, notably the discovery of the predicted intermediate vector bosons $W^\pm$ and Z at CERN in 1983 by the UA1 followed by the UA2 Collaborations [1-2], and most recently the suggestions for evidence of the top quark found by the CDF Collaboration [1-3] at FermiLab. In particular, since 1989, the LEP e^+e^- collider at CERN has provided an unparalleled environment for precision tests of the electroweak theory; with its luminosity of $\sim 10^{31}/cm^{-2}s^{-1}$ and relatively background-free (compared to $p\bar{p}$ machines) conditions it is a veritable Z factory, having produced upwards of 2 million of the particles to date, running at center-of-mass energies around 91.2 GeV.

However, the electroweak theory, which unifies the electromagnetic and weak interactions based on the symmetry group $SU(2) \otimes U(1)$ with spontaneous symmetry breaking through the Higgs mechanism [1-4], suffers from some important theoretical problems. For instance, when radiative corrections to the Higgs boson mass are considered, the theory becomes unrenormalizeable, since the amplitudes of the Feynman diagrams corresponding to the loop corrections contribute terms whose sum diverges [1-5]. To address this problem some extension to the Standard Model is necessary. Some theoretical solutions that have been proposed are compositeness of quarks, leptons and gauge bosons [1-6], the technicolor (composite Higgs) model [1-7], and supersymmetry (SUSY) [1-8]. SUSY theories provide a "clean" solution to the renormalizeability problem without the technical difficulties encountered by some of the other alternatives such as technicolor, which may lead to flavor-changing neutral currents [1-9]. In SUSY, each Standard Model particle is assigned a supersymmetric partner differing in spin by one-half a unit (but identical in terms of all other quantum numbers except for mass). Because these boson-fermion pairs couple identically to the Higgs boson in these models, the divergent one-loop diagrams from particle and superparticle enter the calculation of the scalar mass correction with a relative minus sign and cancel up to a finite quantity which is a function of the boson-fermion mass difference at energies E_C well above these masses. In order to preserve unitarity, E_C must be $<<1$ TeV. Thus the masses of the SUSY particles must also be $<< 1$ TeV,

hence possibly observable at LEP.

Just as the LEP "Z factory" provides a nearly ideal environment for experimental verification of the Standard Model and measurement of its parameters, its potential for the discovery of new physics at energies up to the Z pole ($\sqrt{s} = 91.25$ GeV) is just as great. As far as SUSY hypotheses are concerned, the Lightest Supersymmetric Particle (LSP) should be only weakly interacting (since its participation in strong or electromagnetic interactions would have already been signaled by its presence in exotic heavy nuclear isotopes [1-10]), and therefore could couple to the Z. The high statistics present at LEP make the detection of a Z decay into SUSY particles possible at the 10^{-5} level. If SUSY particles do not exist at LEP energies, these same high statistics can be used to set significantly tighter limits on the Z branching ratio into such particles. Table 1.1 gives a summary of current mass limits on SUSY particles (all at 95% confidence except those from CDF at 90%) [1-11].

SUSY Particle	Mass Limit [GeV]	Experiment (Year)
χ (Lightest Neutralino)	> 20	ALEPH (1992)
χ' (Neutralino)	> 45	ALEPH (1992)
$\chi^{\pm}$ (Charginos)	> 45.2	ALEPH (1992)
$\tilde{\nu}$ (Sneutrino)	> 41.8	L3 (1993)
$\tilde{e}$ (Selectron)	> 45	ALEPH (1992)
$\tilde{\mu}$ (Smuon)	> 45	ALEPH (1992)
$\tilde{\tau}$ (Stau)	> 45	ALEPH (1992)
$\tilde{q}$ (Squark)	> 90	CDF (1992)
$\tilde{g}$ (Gluino)	> 100 with window $1 - 4$	CDF (1992)

Table 1.1: *Current lower limits at 95% confidence (90% confidence for CDF) on the masses of SUSY particles.*

To date, production of equal-mass pairs of SUSY particles (charginos, sleptons, squarks and gluinos) has not been observed and, as can be seen above, has therefore already been excluded up to at least the LEP beam energy (45 GeV). However, the neutralinos, a spectrum of 4 Majorana fermions (denoted $\chi, \chi', \chi'', \chi'''$ in order of increasing mass), linear combinations of the SUSY counterparts of the Z, γ and Higgs bosons, of which the lightest, χ, is a candidate for the LSP, can be produced in either identical or non-identical pairs via decay of the Z, according to SUSY theories. This unique property of the neutralinos enables the search for SUSY particles to be extended above the LEP I beam energy and nearly to the center-of-mass energy corresponding to the Z resonance.

This work presents a search for the lightest and next-to-lightest neutralinos, χ and χ', via the reactions: $e^{+}e^{-} \longrightarrow Z \to \chi\chi'$ or $\chi'\chi'$, where $\chi' \longrightarrow \chi + Z^{*}$, $Z^{*} \longrightarrow f\bar{f}$ [where Z^{*} is a virtual Z and f is any quark or lepton]. The study is based on $\sim 68pb^{-1}$ of integrated luminosity collected by the L3 detector at LEP in 1991,1992 and 1993, corresponding to approximately 1.9 million Z decays. First, a model-independent search is performed in the phase space of the χ and χ' masses. Contours corresponding to limits on Br$(Z \to \chi + \chi')$ are then determined in this space (the

most recent published limit prior to this analysis was of order 10^{-4} [8-2] based on 1990 and 1991 data). Then, an interpretation is done in the context of the Minimal Supersymmetric Standard Model(MSSM); exclusion of area in the $m_\chi - m_{\chi'}$ plane in the model-independent analysis is combined with current Z-lineshape data which impose limitations on $\Gamma_{newphysics}$, to exclude regions of the MSSM parameter space (characterized by the three quantities M, μ and $\tan\beta$), within the kinematical limits imposed by LEP I.

Chapter 2

Theory

This chapter presents some of the theoretical considerations underlying the search for SUSY particles in general and neutralinos in particular. SUSY theories are motivated by the inability of the Standard Model to deal with loop corrections to scalar particle masses in a non-pathological way. In general, any super-gauge group can be created via an extension of the Lie algebra underlying the Standard Model. The net result is a doubling of the existing SM particle spectrum. Already at this stage decay modes of the Z into neutralinos can be envisioned. By imposing restrictions on supersymmetry-breaking in the low-energy (M_W) limit, the Lagrangian of the Minimal Supersymmetric Standard Model (MSSM) can be constructed, the masses and couplings of the neutralinos specified, and the production cross-sections from $e^+e^- \longrightarrow Z \to \chi\chi'$ or $\chi'\chi'$ and the decay widths of $Z \longrightarrow \chi\chi'$ or $\chi'\chi'$ and $\chi' \longrightarrow \chi + Z^*$, $Z^* \longrightarrow f\bar{f}$ predicted in terms of the three model parameters: M, μ and $\tan\beta$.

2.1   Motivation for SUSY theories–Unitarity, the Hierarchy Problem and Naturalness

One of the outstanding problems in the Standard Model concerns the renormalizeability of the electroweak theory, which demands that the sum of partial cross-sections resulting from a partial wave expansion (representing the contribution of different Feynman diagrams i, involving initial-state particles with possibly different values of relative angular momentum j, to a physics process) not exceed a certain value, called the Froissart bound [2-1] (the general case of the unitary bound):

$$\sum_{i,j}^{\infty} \sigma_{i,j} < (ln[s])^2 \qquad (2.1)$$

where s is the center-of-mass energy implicated in the process. This translates into the requirement that the mass of the scalar Higgs boson needed in the theory not exceed $\sim$1 TeV. Renormalizeability comes into jeopardy when amplitudes of diagrams representing radiative corrections to the mass are considered; the sum diverges quadratically, the one-loop correction diagrams contributing terms of the form [2-2]

$$\partial m^2 = \vartheta(\alpha/\pi)\Lambda^2 \qquad (2.2)$$

where $\alpha = e^2/\hbar c = 1/137$ (the fine-structure constant) and Λ is the mass scale used. Not only is unitarity thus endangered, but a condition known as "unnaturalness" also arises, namely that the correction to the Higgs mass is larger than the value itself, i.e.

$$\partial m_H > m_H \qquad (2.3)$$

This condition presents grave problems in the context of Grand Unified Theories (GUT's). Such theories are forced to presuppose the existence of two radically different mass scales; one, the mass of the physical Higgs particle associated with electroweak symmetry-breaking (M_W), constrained by unitarity, the other, the mass of the Higgses associated with GUT symmetry-breaking, constrained by the theoretical masses of the GUT bosons which would be needed for proton decay. These two mass scales correspond to a hierarchy of different vacuum expectation values which the scalar potential must yield; thus the so-called "hierarchy problem". The quadratic divergences coming from the Higgs radiative correction diagrams translate into a quadratic dependence of the square of the "running" Higgs mass on the mass scales used in the solution to the Renormalization Group Equations (RGE) [2-3]:

$$M^2(\mu_2) = M^2(\mu_1) + Cg^2(\mu_2^2 - \mu_1^2) + g^2 R + \vartheta(g^4) \qquad (2.4)$$

where g is a coupling, C a dimensionless constant and R a quantity which grows at most logarithmically as $\mu_1 - \mu_2 \longrightarrow \infty$. In the case of Grand Unified Theories the two mass scales are $\mu_1 = M_X$ (the GUT symmetry-breaking scale–0.9 × 10^{15} GeV) and $\mu_2 = M_W$ (the electroweak symmetry-breaking scale). Since $\mu_1 \gg \mu_2$, the above evaluated at the electroweak symmetry-breaking scale reduces to: [2-3]

$$M_H^2(M_W) \simeq M_H^2(M_X) - Cg^2 M_X^2 \qquad (2.5)$$

Because unitarity requires that $M_H(M_W) \sim \vartheta(M_W)$, we see that "unnaturalness" forces us into a situation where we must choose the parameters C and g to an accuracy of 10^{-26} [2-3] in order to assure that the two terms on the right-hand side of the above equation cancel up to a factor of M_W^2, which is clearly undesirable.

Theories of Supersymmetry (SUSY) provide a relatively clean way to restore renormalizeability to the electroweak theory and address the naturalness problem faced by GUT's. A supersymmetric partner differing in spin by one-half a unit, but identical in terms of all other quantum numbers (except eventually for mass), is assigned to each Standard Model particle. Because they couple identically to the Higgs, the one-loop radiative correction diagrams contributed by these superpartners are also quadratically divergent, but enter the calculation of the scalar mass correction with a relative minus sign. If supersymmetry were an exact symmetry, the terms contributed by particle and superparticle would cancel exactly [2-2], viz.:

$$\partial m^2 = \vartheta(\alpha/\pi)\Lambda^2 - \vartheta(\alpha/\pi)\Lambda^2 \qquad (2.6)$$

14

However, to date no superpartner of any SM particle has been observed, leading to the assumption that SUSY particles must be much heavier than their SM partners, and hence that SUSY is a broken symmetry. In this case the relation becomes [2-2]:

$$\partial m^2 = \vartheta(\alpha/\pi)|m_b^2 - m_f^2| \tag{2.7}$$

where m_b and m_f are masses of the bosonic and fermionic partners. Therefore supersymmetry, even though broken, will respect unitarity, since the right-hand-side of the above equation is a finite quantity. The naturalness problem is also solved if in addition [2-2]

$$|m_b^2 - m_f^2| \sim \vartheta(1 TeV^2) \tag{2.8}$$

SUSY models therefore predict the existence of an entire spectrum of new particles well below the energy of 1 TeV.

2.2 Construction of Supergroups, Supermultiplets and the Superparticle Spectrum

The mathematical foundation underlying the Standard Model is a Lie algebra formed by the generators T_a of a non-abelian internal symmetry (SU(3)), characterized by the internal commutation relation [2-4]

$$[T_a, T_b] = if_{abc}T_c \tag{2.9}$$

(where $a \in \{1, \ldots, 8\}$ over the gluons and the f_{abc} are the structure constants of the group) and by its relation to the space-time translation (P^μ) and rotation ($M^{\mu\nu}$) generators of the Poincaré group via the commutators: [2-4]

$$[T_a, H] = [T_a, P^\mu] = [T_a, M^{\mu\nu}] = 0 \tag{2.10}$$

The generators of a supergroup of dimension N are self-conjugate spin-1/2 Majorana 4-spinors Q_α^i ($i = 1, \ldots, N; \alpha = 1, \ldots, 4$) which turn boson fields into fermion fields, viz.: [2-4]

$$Q_\alpha |boson\rangle = |fermion\rangle \tag{2.11}$$

changing the total angular momentum J by one-half a unit. They are linked to the above SM Poincaré generators by the following set of both commutation and anticommutation relations which are therefore said to form an extended or "graded" Lie algebra: [2-4]

$$[Q_\alpha, M^{\mu\nu}] = i(\sigma^{\mu\nu}Q)_\alpha \qquad [Q_\alpha, P^\mu] = 0 \tag{2.12}$$
$$\{Q_\alpha, \bar{Q}_\beta\} = -2(\gamma_\mu)_{\alpha\beta}P^\mu \quad \{Q_\alpha, Q_\beta\} = \{\bar{Q}_\alpha, \bar{Q}_\beta\} = 0$$

where $\sigma^{\mu\nu} = \frac{1}{4}[\gamma^\mu, \gamma^\nu]$ and $\bar{Q}_\alpha = Q_\alpha^T\gamma^0$. In particular, the commutation relation between the Q_α and $M^{\mu\nu}$ assures the spinor nature of the Q_α, while those between

15

the Q_α and P^μ assure that a particle and its superpartner share the same gauge quantum numbers (except for mass because of the broken symmetry, and, of course, spin) [2-5].

All supergroups with dimension greater than N=1 are ruled out because they do not allow fermions in chiral representations [2-4]. The N=1 SUSY generator Q_α acts on the chiral, spin-1 and spin-2 Standard Model fields to produce the following spin superfields or "supermultiplets", where $\tilde{p}$ denotes an SM field's superpartner field: [2-4]

$$\begin{array}{ccc} \text{chiral} & \text{gauge} & \text{graviton/gravitino} \end{array} \qquad (2.13)$$

$$\begin{array}{ccc} f \begin{pmatrix} \frac{1}{2} \\ 0 \end{pmatrix} & \mathcal{G} \begin{pmatrix} 1 \\ \frac{1}{2} \end{pmatrix} & G \begin{pmatrix} 2 \\ \frac{3}{2} \end{pmatrix} \\ \tilde{f} & \tilde{\mathcal{G}} & \tilde{G} \end{array}$$

One might consider the possibility of the superpartners of the chiral fermions $\tilde{f}$ above having spin 1 instead of spin 0 as shown. Given that all known spin-one particles in interacting quantum field theories are gauge bosons [2-2], the commutation relations between the SUSY and Poincaré groups would then imply that the chiral fermions are also gauge particles, which is false.

The neutralinos have their origin in the weak gauge supermultiplets involving the W and B fields:

$$\begin{pmatrix} W \\ \tilde{W} \end{pmatrix} \begin{pmatrix} B \\ \tilde{B} \end{pmatrix} \qquad (2.14)$$

Because of the conservation of most quantum numbers between particles and superpartners in SUSY models, the supersymmetric partners of the γ and the Z, the photino ($\tilde{\gamma}$) and the zino ($\tilde{Z}$), are formed from linear combinations of the gaugino fields $\tilde{W}^3$ and $\tilde{B}$ in the same way as the photon and Z are formed using their partner gauge fields W^3 and B, viz: [2-4]

$$\tilde{\gamma} = \sin\theta_W \tilde{W}^3 + \cos\theta_W \tilde{B} \quad \tilde{Z} = \cos\theta_W \tilde{W}^3 - \sin\theta_W \tilde{B} \qquad (2.15)$$

The above chiral and gauge particles acquire mass via the Higgs Mechanism [2-6], operating somewhat differently than in the Standard Model. A single Higgs doublet giving mass to all fermions, as in the Standard Model, results in the presence of flavor changing neutral currents (FCNC) at tree level [2-7]. To solve this problem two chiral Higgs superfields are introduced: [2-8]

$$\begin{pmatrix} \phi_1 \\ \tilde{\phi}_1 \end{pmatrix} \begin{pmatrix} \phi_2 \\ \tilde{\phi}_2 \end{pmatrix} \qquad (2.16)$$

each containing one of the following complex spin-0 Higgs doublet fields: [2-9]

$$\phi_1 = \begin{pmatrix} H_1^+ \\ H_1^0 \end{pmatrix} \quad \phi_2 = \begin{pmatrix} H_2^0 \\ H_2^- \end{pmatrix} \qquad (2.17)$$

with their respective vacuum expectation values v_1, v_2, as well as a corresponding complex spin-1/2 superpartner "Higgsino" doublet field:

$$\tilde{\phi}_1 = \begin{pmatrix} \tilde{H}_1^+ \\ \tilde{H}_1^0 \end{pmatrix} \quad \tilde{\phi}_2 = \begin{pmatrix} \tilde{H}_2^0 \\ \tilde{H}_2^- \end{pmatrix} \tag{2.18}$$

For the spin-0 doublets ϕ_1 and ϕ_2, the Higgs potential becomes [2-10]:

$$\begin{aligned} V(\phi_1, \phi_2) &= \lambda_1(\phi_1^\dagger\phi_1 - v_1^2)^2 + \lambda_2(\phi_2^\dagger\phi_2 - v_2^2)^2 \\ &\quad + \lambda_3[(\phi_1^\dagger\phi_1 - v_1^2) + (\phi_2^\dagger\phi_2 - v_2^2)]^2 \\ &\quad + \lambda_4[(\phi_1^\dagger\phi_1)(\phi_2^\dagger\phi_2) - (\phi_1^\dagger\phi_2)(\phi_2^\dagger\phi_1)] \\ &\quad + \lambda_5[Re(\phi_1^\dagger\phi_2) - v_1 v_2 \cos\xi]^2 \\ &\quad + \lambda_6[Im(\phi_1^\dagger\phi_2) - v_1 v_2 \sin\xi]^2 \end{aligned} \tag{2.19}$$

Since the phase ξ is not an independent parameter and is usually set to 0, the Higgs potential is left with 8 degrees of freedom (the two vev's and the 6 λ's). Three of these are absorbed ("eaten") when the charged components of the isotriplet W vector field and one of the two physical fields which diagonalize the $W^3 - B$ basis acquire longitudinal polarization vector components, thus giving mass to the corresponding $W^\pm$ and Z bosons. Therefore the spin-0 Higgs doublets produce 5 "normal" (as opposed to supersymmetric) physical particles– the charged $H^\pm$, the neutrals H^0 and h^0, and the CP-odd A^0.

The spin-1/2 doublets $\tilde{\phi}_1$ and $\tilde{\phi}_2$ contribute their charged and neutral components to create the gauginos (the supersymmetric counterparts of the SM gauge bosons) in the following manner: When the mass symmetry is broken, the two charged higgsino fields $\tilde{H}_1^+$ and $\tilde{H}_2^-$ mix with the charged wino fields $\tilde{W}^\pm$ to form the charginos $\chi_{1,2}^\pm$, and the two neutral higgsino fields $\tilde{H}_1^0$ and $\tilde{H}_2^0$ with the $\tilde{B}$ and $\tilde{W}^3$ to form the neutralinos $\chi_{1,2,3,4}$: [2-11]

$$\chi_i \equiv \alpha_i\tilde{W}^3 + \beta_i\tilde{B} + \gamma_i\tilde{H}_1^0 + \delta_i\tilde{H}_2^0 \text{ where } i = (1, \ldots, 4) \tag{2.20}$$

The charginos and the neutralinos become the actual physical states.

Even at this point, without assuming a specific model, couplings of the neutralinos to the Z and to fermions can be imagined. Because of the conservation of most gauge quantum numbers between particles and their superpartners, the neutralinos, through their higgsino components, could couple to other particles as the Higgs does, including the Z. They could also then couple to fermions and sfermions mainly via their gaugino components (the contribution from the higgsino components being related to the Yukawa couplings, as in the Standard Model [2-12]). These two couplings translate into the vertices which are the building blocks of the Feynman diagram describing the reactions searched for in this study (see Figure 2-1). (The coupling of both neutralinos and standard-model fermions to sfermions could also result in neutralino production via the t-channel exchange of a sfermion. However, at LEP I energies which are very close to the Z pole (~ 91.25 GeV), the t-channel contribution is assumed to be

17
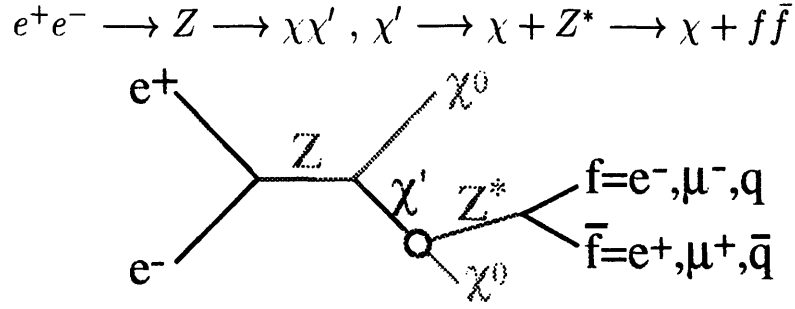
$$e^+e^- \longrightarrow Z \longrightarrow \chi\chi' \ , \ \chi' \longrightarrow \chi + Z^* \longrightarrow \chi + f\bar{f}$$

Figure 2-1: *Feynman diagram for the process* $e^+e^- \longrightarrow Z \longrightarrow \chi\chi'$, $\chi' \longrightarrow \chi + Z^* \longrightarrow \chi + f\bar{f}$.

insignificant compared to that of the s-channel process which proceeds via the decay of the Z.)

This then completes the minimal particle content needed for a supersymmetric theory, which is summarized in Table 2.1. The total particle spectrum consists of the non-SUSY states plus the SUSY physical (mixed) states.

Non-SUSY States	Add'l SUSY States (unmixed)	SUSY Physical States (mixed)
q	$\tilde{q}_L, \tilde{q}_R$	$\tilde{q}_1, \tilde{q}_2$
l	$\tilde{l}_L, \tilde{l}_R$	$\tilde{l}_1, \tilde{l}_2$
ν	$\tilde{\nu}$	$\tilde{\nu}$
g	$\tilde{g}$	$\tilde{g}$
$W^\pm, H^\pm$	$\tilde{W}^\pm, \tilde{H}_1^+, \tilde{H}_2^-$	$\chi_{1,2}^\pm$
γ, Z, H^0, A^0, h^0	$\tilde{B}, \tilde{W}^3, \tilde{H}_1^0, \tilde{H}_2^0$	$\chi_{1,2,3,4}$

Table 2.1: *Minimal Particle Content of a SUSY Model.*

2.3 The Minimal Supersymmetric Standard Model (MSSM)

It is the manner in which SUSY is broken which differentiates the different models from each other. Among them, the Minimal Supersymmetric Standard Model (MSSM) [2-13] is currently the most widely studied , and is generally considered to be the reference model. It proposes a global N=1 supersymmetry, spontaneously broken at high energies by a super-Higgs sector containing a Goldstone fermion (or "goldstino") which is "eaten" by the gravitino. At low ($\sim M_W$) energies, this breaking is transmitted to the ordinary observable sector by the introduction of "soft" explicit symmetry-breaking terms in the Lagrangian which neither spoil the high-energy behavior of the theory (i.e. reintroducing the quadratic divergences the theory was originally conceived to solve), nor introduce explicit chiral particle masses. This is

because the coupling between super-Higgs and ordinary sectors is relatively weak since it proceeds uniquely through gravitational interactions. In the low-energy limit, the "effective" symmetry-breaking scale is obtained by fixing the gravitino mass ($m_{3/2}$) as follows [2-13]:

$$m_{3/2} = (\frac{8\pi}{3})^{1/2}\frac{M_S^2}{M_p} \tag{2.21}$$

where M_S^2 is the SUSY-breaking scale (presumed to be $\sim \vartheta(10^{11}GeV/c^2)$ [2-2] in order to yield an effective breaking scale of $\sim \vartheta(1TeV/c^2)$ to satisfy unitarity) and M_p the Planck scale ($\sim \vartheta(10^{19}GeV/c^2)$). This low-energy approximation leads to a Lagrangian of the following form [2-14]:

$$L = L_{supersymm} + L_{breaking} \tag{2.22}$$

where

$$L_{supersymm} = L_{supersymm}[SU(3) \otimes SU(2) \otimes U(1); f] \tag{2.23}$$

with $\qquad f = f_Y + \mu H_1 H_2$

where f_Y are the Yukawa couplings and $\mu H_1 H_2$ a mass coupling between the 2 Higgs chiral superfields,

$$L_{breaking} = -m^2\sum_i |\phi_i|^2 - M\sum_\alpha \lambda_\alpha\lambda_\alpha + (Amf_Y + Bm\mu H_1 H_2 + \text{hermitian conjugate})$$
$$\tag{2.24}$$

where m is a universal mass for all scalars ϕ_i, M is likewise a universal mass for all gauginos λ_α, and A and B are real parameters. In addition, the ratio of the vacuum expectation values v_1 and v_2 of the required two Higgs doublets,

$$\tan\beta = \frac{v_2}{v_1} \tag{2.25}$$

is a model parameter.

In addition, this Lagrangian rests on the following assumptions [2-15]:

- There is no violation of baryon number, lepton number, or CP except in the Yukawa couplings–the so-called Universality Hypothesis.

- A discrete parity known as R-parity, defined as:

$$R|\text{Standard Particles} > \quad = \quad +|\text{Standard Particles} > \tag{2.26}$$
$$R|\text{Superpartners} > \quad = \quad -|\text{Superpartners} >$$

is conserved. Under this assumption SUSY particles can only be produced in pairs and the Lightest Supersymmetric Particle (LSP) must be stable.

After the Lagrangian is renormalized at a scale of order M_W, the mass terms for the gaugino-higgsino fields become [2-16]:

19

$$L_m(gaugino - higgsino) = -\frac{1}{2}M_3\bar{\lambda}_\alpha\lambda_\alpha - \frac{1}{2}\bar{\chi}M^{(0)}\chi - (\bar{\psi}M^{(c)}\psi + h.c.) \qquad (2.27)$$

where $\lambda_\alpha, \alpha = 1, \ldots, 8$ are gluino fields,

$$\chi = \begin{pmatrix} \tilde{B} \\ \tilde{W}^3 \\ \tilde{H}_1^0 \\ \tilde{H}_2^0 \end{pmatrix}, \psi = \begin{pmatrix} \tilde{W}^+ + (\tilde{W}^-)^c \\ \tilde{H}_1^+ + (\tilde{H}_2^-)^c \end{pmatrix} \qquad (2.28)$$

the Majorana neutralino and Dirac chargino fields, respectively, and

$$M^{(c)} = \begin{pmatrix} M_2 & \sqrt{2}M_W\sin\beta \\ \sqrt{2}M_W\cos\beta & \mu_R \end{pmatrix} \qquad (2.29)$$

and

$$M^{(0)} = \begin{pmatrix} M_1 & 0 & -M_Z\cos\beta\sin\theta_W & M_Z\sin\beta\sin\theta_W \\ 0 & M_2 & M_Z\cos\beta\cos\theta_W & -M_Z\sin\beta\cos\theta_W \\ -M_Z\cos\beta\sin\theta_W & M_Z\cos\beta\cos\theta_W & 0 & -\mu_R \\ M_Z\sin\beta\sin\theta_W & -M_Z\sin\beta\cos\theta_W & -\mu_R & 0 \end{pmatrix} \qquad (2.30)$$

with

$$M_i = Z_i M \quad Z_i = \frac{\alpha_i(M_W)}{\alpha_i(M_X)} = (3, 0.8, 0.4) \quad Z_R = c(1 - 2KM_t^2)^{1/4}$$

$$\mu_R = Z_R\mu \qquad c = 1.4 \qquad K = (1.2 \times 10^{-5})GeV^{-2}$$

$$M_t = \sqrt{2}h_t/gM_W \qquad (2.31)$$

(where h_t is the Yukawa coupling for the top quark and $M_X = 3 \times 10^{16}$ GeV) the chargino and neutralino mixing matrices. The four physical neutralino states and their masses are taken to be the eigenstates and eigenvalues of the neutralino mixing matrix.

Assuming neutralino pair production through the decay of a Z, the partial width of $Z \to \chi_i\chi_j$ is given by [2-17]:

$$\Gamma_{\chi_i\chi_j} = \frac{G_F M_Z^3}{6\sqrt{2}\pi}A_{ij}^2[1 - \frac{(\eta_i m_{\chi_i} + \eta_j m_{\chi_j})^2}{s} + \frac{1}{2}\frac{(\eta_i m_{\chi_i} - \eta_j m_{\chi_j})^2}{s} - \frac{1}{2}(\frac{m_{\chi_i}^2 - m_{\chi_j}^2}{s})^2]$$

$$\times \sqrt{1 - 2\frac{m_{\chi_i}^2 + m_{\chi_j}^2}{s} + (\frac{m_{\chi_i}^2 - m_{\chi_j}^2}{s})^2} \qquad (2.32)$$

where $A_{ij} = N_{i3}N_{j3} - N_{i4}N_{j4}$, N_{ij} being a real 4×4 matrix which diagonalizes the neutralino mass matrix, viz.: [2-18]

$$(NM^{(0)}N^T)_{ij} = m_{\chi_i}\delta_{ij}, \qquad (2.33)$$

m_{χ_i} and m_{χ_j} are the masses and $\eta_i\eta_j = \pm1$ is the relative CP of χ_i and χ_j. The coupling $|A_{ij}|^2$ has a maximum value of 1 which is attainable when χ_i and χ_j are pure Higgsino states, and falls to zero if either χ_i or χ_j is a pure gaugino state [2-19]. As an example, for $(M, \mu_R, \tan\beta) = (100, 50, 2)$, corresponding to $(m_\chi, m_{\chi'}) = (13.2$ GeV,60.7 GeV$)$, $|A_{11}|^2 = 0.090$ and $|A_{12}|^2 = 0.075$, i.e. the $Z\chi\chi$ coupling is 20.5% greater than the $Z\chi\chi'$ coupling in this case.

The production cross section for the two states χ_i, χ_j is given by [2-18]:

$$\frac{d\sigma}{d\cos\theta}(e^+e^- \to \chi i\chi j) = A_{ij}^2 \frac{g^4}{2^{11}\pi} \frac{1 + (4\sin^2\theta_W - 1)^2}{\cos^4\theta_W} \times$$

$$\frac{s}{(s - M_Z)^2 + \Gamma_Z^2 M_Z^2}[1 - 2\frac{m_i^2 + m_j^2}{s} + (\frac{m_i^2 - m_j^2}{s})^2]^{1/2} \qquad (2.34)$$

$$\times[1 - 4\frac{m_i m_j}{s} - \frac{m_i^2 - m_j^2}{s} + (1 - 2\frac{m_i^2 + m_j^2}{s} + (\frac{m_i^2 - m_j^2}{s})^2)\cos\theta]$$

The partial decay width of $\chi' \to \chi + Z^* \to \chi + f\bar{f}$ where the fermion has weak isospin T_3 and charge Q is then [2-18]:

$$\Gamma(\chi_i \to \chi_j f\bar{f}) = \frac{m_i A_{ij}^2}{3(2^9)\pi^3} \frac{g^4}{\cos^4\theta_W}[(T_3 - Q\sin^2\theta_W)^2 + Q^2\sin^4\theta_W] \times \qquad (2.35)$$

$$\int_0^{(1-|x|)^2}[-t^2 + \frac{1}{2}(1 + 6x + x^2)t + \frac{1}{2}(1 - x^2)^2]\frac{[t^2 - 2(1+x^2)t + (1-x^2)^2]^{1/2}}{(t - M_Z^2/m_i^2)^2}dt$$

where $x = m_j/m_i$ and A is the same coupling matrix as described above. This expression must be multiplied by 3 when $f = q$ because of color. The fermion mass is considered negligible.

Thus, for any triplet of MSSM parameter values $(M, \mu_R$(henceforth known as $\mu)$ and $\tan\beta)$, the mixing matrix $M^{(0)}$ can be diagonalized, the neutralino masses m_{χ_i} and the couplings A_{ij} between them uniquely determined and the theoretical production cross-sections and decay widths for Z into a pair of neutralinos of those masses and then the decay width of a neutralino into the lightest neutralino plus any fermion pair computed. These can then be used to calculate, for a given integrated luminosity, the number of MSSM-predicted Z decays into neutralinos for a given final-state channel, which can be compared against experimental data. The MSSM-predicted decay width for Z into neutralinos can be compared with the total width currently available for Z decays via new physics processes (calculated from the difference between the current measurement of the Z width and the theoretical Z width predicted by the Standard Model).

21

Chapter 3

The LEP e^+e^- Collider

In searches for new particles and new physics processes, three factors are of prime importance–the attainment of particle collisions at high center-of-mass energies (under the assumption that the particles associated with new physics processes are more massive than known particles and hence require higher energies for their creation), the rate of such collisions (luminosity), especially important for the detection of rare processes. and the clarity of the anticipated signatures. The optimization of these three factors often involves trading them off against each other, and balancing them against economic considerations. Today the standard apparatus for attaining high rates of collision at high center-of-mass energies has become the charged-particle acclerator, of either the fixed-target or colliding-beam type. Although fixed-target machines in general yield higher luminosities by several orders of magnitude, energy considerations favor colliding-beam accelerators; to attain the same center-of-mass energy as two colliding beams of identical-mass particles, a single beam incident on a fixed-target must have an energy proportional to the square of that of either colliding beam. Charged-particle colliders exist in either the linear or storage-ring configurations; at the present time, economic factors have favored the latter because of the ability to recirculate and effectively "re-use" the same particle beams for periods of many hours. An important trade-off involves the choice of charged particles to accelerate. Proton-antiproton and proton-proton colliders provide a good environment to study strong interactions, but because the initial state is not composed of elementary particles, there is significant background which must be distinguished from the particles actually participating in the reactions of interest. This is not true for electron-positron colliders, which are relatively background-free and thus provide the best environment for the study of electroweak interactions and the search for new particles participating in those interactions.

The Large Electron-Positron Collider [3-1] is currently the highest center-of-mass energy (currently $\sim$ 45 GeV per beam) accelerator in this category, in operation since August 1989. Located in an approximately 100m-deep underground tunnel straddling the French-Swiss border near Geneva (See Figure 3-1), it has a circumference of 26.7 km, and is composed of 8 circular sections of length 2840 m each, equipped with 3304 dipole (beam-bending) magnets, 8 straight sections of length 490 m each, of which 4 are occupied by the four experiments (ALEPH, DELPHI, L3, and OPAL),

and 2 additional straight sections housing radio-frequency (RF) cavities with a total power of 16MW. These accelerate the beam to collision energy and compensate for energy lost due to synchrotron radiation, which amounts to 117 MeV per turn at 45 GeV [3-2]. A total of nearly 2000 quadrupole (focussing) magnets continually correct the beam position as it circulates around the ring. Some additional principal LEP parameters are shown in Table 3.1.
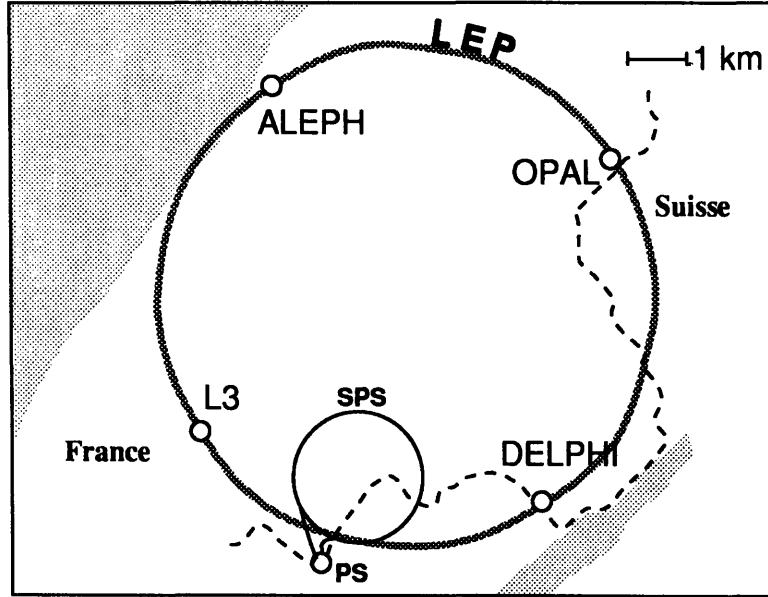
Figure 3-1: *The geographical location of the LEP e^+e^- collider complex and the four LEP experiments*

Circumference	26658.883 m
Dipole bending radius	3096.175 m
Phase advance/period	60°
Horizontal betatron wave number	70.44
Vertical betatron wave number	78.20
Number of bunches per beam	4 (1991-Sept '92) 8 (Sept '92-1993)
Number of interaction points	4
Number of RF cavities	128
RF frequency	352.20904 MHz
Injection energy	20 GeV
Maximum beam energy	$\sim$ 60 GeV
Peak luminosity (3 mA beam current)	$1.6 \times 10^{30} cm^{-2} s^{-1}$

Table 3.1: *Principal LEP parameters*

The sequence of beam production-injection-acceleration is as follows: Positrons are created in one of the two LEP injector linear accelerators (LIL), which accelerates

a 100 Hz pulsed electron beam to an energy of 200 MeV and directs it onto a tungsten target. The second linear accelerator accelerates the emitted positrons to 600 MeV along with electrons that have been directly injected from a cathode-ray tube. These are then injected into the Electron-Positron Accumulation Ring (EPA), where they are stored until enough have been accumulated ($\sim 2 \times 10^{11}$) for injection into the Proton Synchrotron (PS). The PS in turn accelerates the particles to an energy of 3.5 GeV prior to injecting them to the Super Proton Synchrotron (SPS), which boosts them to an energy of 20 GeV. Finally, the electrons and positrons are injected into LEP, where either four or eight (see Table 3.1) bunches of each circulate in opposite directions, are simultaneously accelerated to the final beam energy (~ 45 GeV), and are focused to collide at the four interaction points (Figure 3-2 shows a schematic of the entire sequence). The approximate bunch size in the horizontal, vertical and beam directions is $\sigma_x \approx 250\mu m$, $\sigma_y \approx 15\mu m$ and $\sigma_z \approx 15mm$, respectively; the typical single-beam current is 0.5mA [3-3]. The instantaneous luminosity decreases slowly with time after injection due to beam-beam interactions via the bremsstrahling process; the typical beam lifetime is ~ 20 hours. Table 3.2 shows typical instantaneous luminosities delivered by LEP from 1991 through 1993, the years during which the data for this study was collected. The switch from 4-bunch to 8-bunch mode towards the end of the 1992 data-taking period is reflected in the more than 60% increase in instantaneous delivered luminosity between 1992 and 1993.
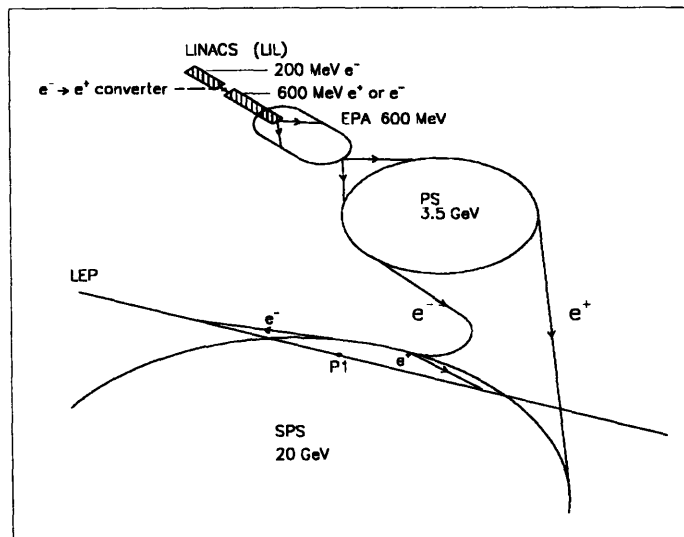
Figure 3-2: *Schematic of the process by which electron and positron beams are created, accumulated, accelerated and injected into the LEP storage ring*

The LEP beam energy is measured with great precision using the resonant depolarization technique, in which the frequency with which the spins of transversely polarized electrons precess about a vertical bending field, a variable related to the

Year	L $(cm^{-2}s^{-1})$
1991	5.19×10^{30}
1992	6.49×10^{30}
1993	1.06×10^{31}

Table 3.2: *Instantaneous delivered luminosity (L) delivered to the L3 detector by LEP during 1991-1993*

beam energy, is measured. A relative energy precision of $\pm 5.7 \times 10^{-5}$, corresponding to ± 5.2 MeV at $\sqrt{s} = M_Z$, is thus obtained. [3-4]

Chapter 4

The L3 Detector

With its high hermeticity (99% coverage of 4π for hadrons), so important in the determination of missing energy, and its excellent ability to detect and resolve electrons and and photons ($\Delta p/p = 1\%$), muons , and hadronic jets, the L3 detector [4-1] (shown in Figures 4-1 and 4-2), one of the four large multipurpose particle detectors [4-2] at LEP, stands in a position to discover new particles and new physics processes, should they be present at LEP I energies. The detector is located in an experimental hall approximately 50m underground at LEP interaction point 2, near the village of St-Genis-Pouilly, France. Proceeding outward from the interaction point, it consists of the following major components:
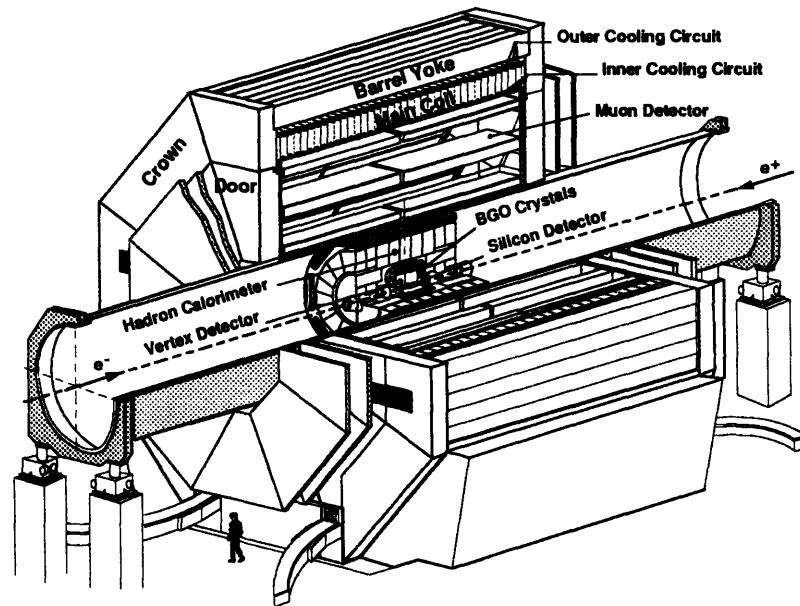
Figure 4-1: *A schematic view of the L3 detector*

- A Silicon Microvertex Detector (SMD) [4-3], which measures the position of charged particle tracks in 3-space for the determination of transverse momenta,
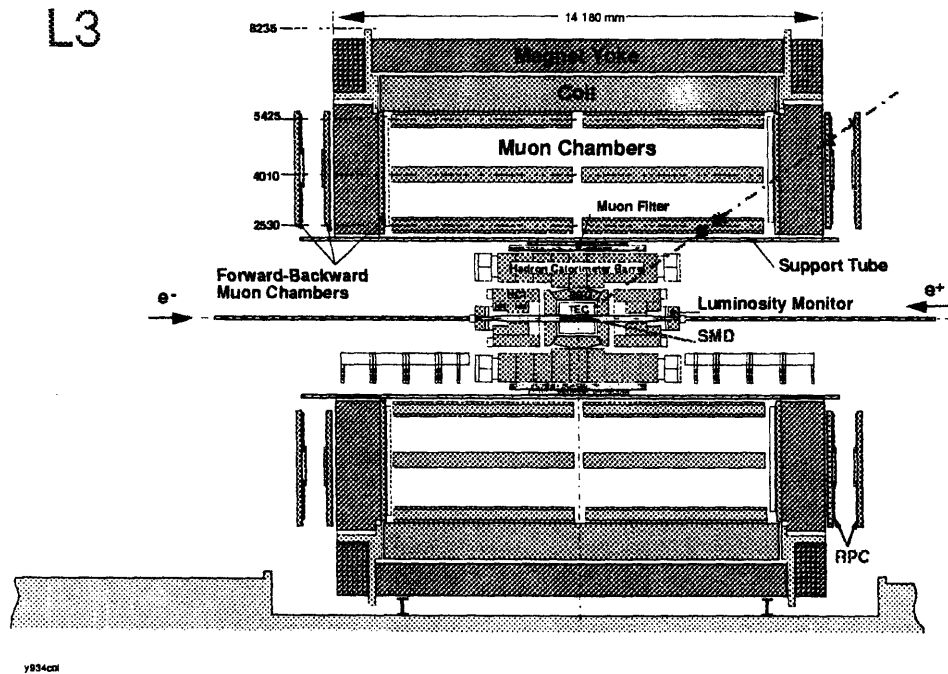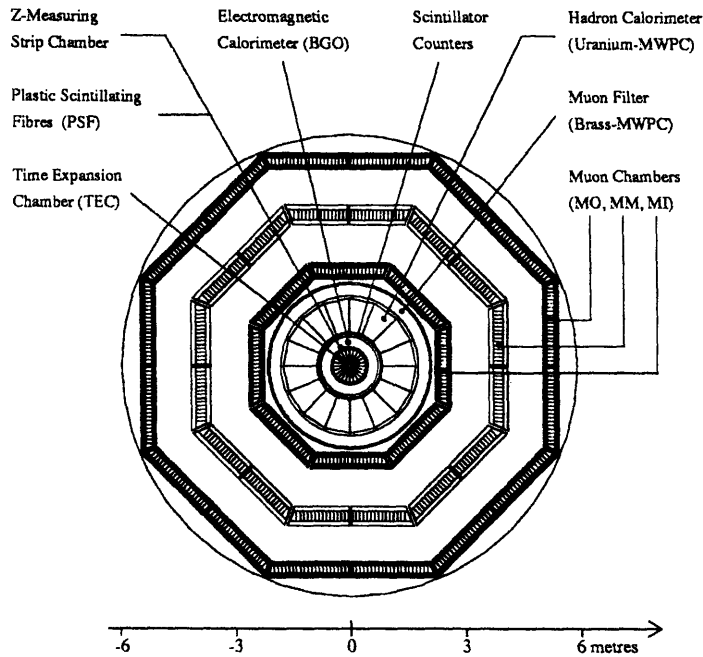
Figure 4-2: *End (top) and side (bottom) views of the L3 detector, showing the scale and positions of the various subdetectors.*

impact parameters and identification of secondary vertices from decays of heavier particles such as τ leptons and b hadrons, complementing the function of the Time Expansion Chamber (TEC) described below. It consists of 2 radial layers of double-sided silicon strip detectors capable of providing $R - \phi$ and $R - z$ coordinate measurements over the polar angle range $|\cos\theta| \leq 0.93$ and over the full range of azimuth, with a coordinate resolution of $\sim 10\mu m$. It was installed in the L3 detector in 1993 and hence was not used for this analysis; therefore it will not be discussed further.

- A Time Expansion Chamber (TEC), which measures the position of charged particle tracks with a single-wire resolution of $50\mu m$ in the $R - \phi$ (bending) plane and an overall resolution of $320\mu m$ in the $R - z$ plane, over the polar angle range $|\cos\theta| \leq 0.88$.

- An Electromagnetic Calorimeter (BGO), consisting of $22X_o$ of Bismuth Germanium Oxide crystals, which measure the energy of electromagnetically interacting particles with an energy resolution of $\frac{\Delta E}{E} = 1.34\%$ at 45 GeV, and a spatial resolution of better than 2mm above 2 GeV. It covers the polar angle ranges $|\cos\theta| \leq 0.743$ (barrel portion) and $0.788 \leq |\cos\theta| \leq 0.980$ (endcap portions).

- Forward Tracking Chambers (FTC) [4-4] located in front of each BGO endcap, which measure the positions of charged particle tracks behind the TEC end flange with an angular resolution of better than 10 mrad.

- Luminosity Monitors (LUMI), consisting of two BGO calorimeters and two sets of proportional wire chambers, with energy resolution of $\frac{\Delta E}{E} = 2\%$ at 45 GeV, and angular resolution of 0.4 mrad in θ and 0.5^o in ϕ, covering the polar angle range $0.998 \leq |\cos\theta| \leq 0.999$, for the purpose of tagging small-angle Bhabha scattering events in order to determine the integrated luminosity delivered to the L3 detector by LEP.

- An azimuthal layer of 30 plastic single scintillation counters (SCI), which reject cosmic-ray muon events with a time-of-flight resolution of 0.46 ns as well as trigger hadronic events (see section 4.7.1). The counters cover the polar angle range $|\cos\theta| \leq 0.83$ and 93% of the azimuth.

- A Hadronic Calorimeter (HCAL), consisting of depleted uranium absorber plates with indispersed proportional-wire chambers as the sampling medium, amounting to a total of between 6 and $7\lambda_I$. It measures the energies of strongly-interacting (hadronic) particles with a resolution of $\frac{\Delta E}{E} = (55/\sqrt{E} + 5)\%$, the total energy of hadronic events from Z decays with a resolution of better than 10%, and the axes of hadronic jets with a resolution of $\sim 2.5^o$, and covers the polar angle ranges $|\cos\theta| \leq 0.819$ (barrel portion) and $0.819 \leq |\cos\theta| \leq 0.995$ (endcap portions), along with the full azimuthal range.

- A Muon Filter (MUFL) [4-1, 4-4], made of an additional 1.03 λ_I of 65-35 Cu-Zn absorber plates sandwiched with proportional wire tubes, which supplements

the hadronic calorimeter and in particular prevents showering particles from reaching the muon chambers (see below).

- A steel Support Tube (ST) [4-1, 4-4] which encloses and supports all the sub-detectors described above and which allows their alignment relative to the LEP beams.

- A precision Muon Spectrometer (MUCH) consisting of three layers of large drift chambers which measure the momenta of muons with a resolution of $\frac{\Delta p}{p} = 2.49\%$ at 45 GeV, covering the polar angle range $|\cos\theta| \le 0.719$. It is currently being augmented by a system of Forward/Backward Muon Chambers (FBMUCH) constructed according to the same principles, which will increase the polar angular acceptance down to $|\cos\theta| \le 0.927$.

- A resistive solenoidal magnet [4-1, 4-4] (the world's largest), composed of a coil made of welded octagonal aluminum plates, enclosing a magnetic flux return yoke of soft iron containing 0.5% carbon, and doors that serve as the pole pieces. It provides a central field of 0.5T, which is measured with Hall-effect probes for the volume within the support tube and, for the muon chambers, with permanently-mounted magnetoresistors.

A somewhat more detailed description of the sub-detectors particularly relevant to this analysis are given below, as well as a short description of the trigger and online data acquisition system.

4.1 The Time Expansion Chamber

The Time Expansion Chamber (TEC) [4-1, 4-4] is designed to precisely determine the location, direction and sign of charged particles (up to E=50 GeV) originating at or near the interaction point. It consists of two concentric cylindrical drift chambers 1 meter in length (see Figure 4-3) for the measurement of coordinates in the $R - \phi$ plane; the inner one extending from R=9cm, divided into 12 sectors of $\Delta\phi = 30°$; the outer one from R=15cm to R=36cm, divided into 24 sectors of of $\Delta\phi = 15°$. These chambers feature a small high-field detection/amplification region at the center of each sector separated from a low-field drift region, and are fitted with sense (anode) wires for the determination of $R - \phi$ coordinates, charge division wires which aid determination of the z coordinate by measuring the charge accumulated at each end of the wire, and groups of grid wires on each side of the amplification region, which by measuring induced currents aid to resolve left-right ambiguities between the sector halves. The drift gas used is 80-20% $CO_2 - C_4H_{10}$. The drift time is calculated by the center-of-gravity method, and Flash ADC's are used to sample and digitize the anode pulses. A system of plastic scintillation fiber (PSF) ribbons, one attached to each sector, monitors the drift velocity.

The TEC inner and outer chambers are surrounded by two layers of cylindrical multiwire proportional chambers with cathode-strip readout (known as the TEC z-chamber) which provide the z-coordinate of the track just outside the outer $R - \phi$
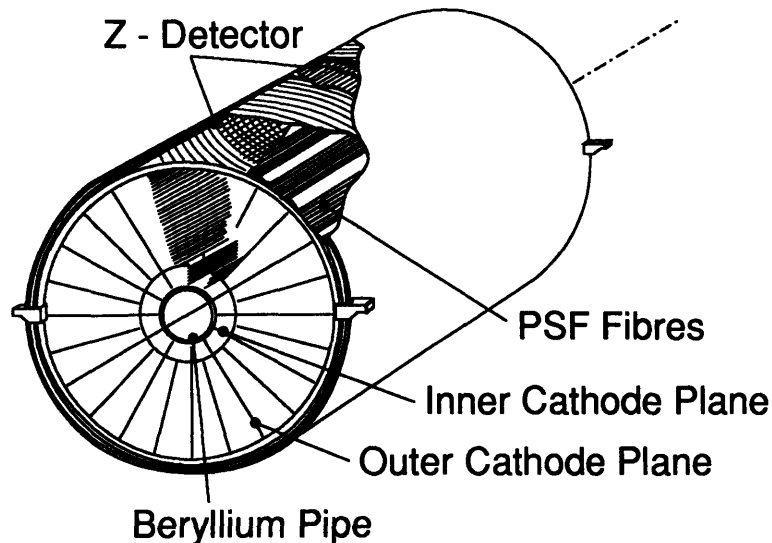
Figure 4-3: *A schematic view of the L3 inner tracking system showing the Time Expansion Chamber (TEC) (indicating inner and outer cathode planes) and the z-chamber.*

chamber. The drift gas used is 80-20% $ArCO_2$. Figure 4-4 shows an $R - \phi$ view of a charged particle's passage through inner and outer TEC sectors and the z-chamber.

4.2 The Electromagnetic Calorimeter

The homogeneous Electromagnetic Calorimeter (BGO) [4-1, 4-4] is designed to measure the position and energy of photons and electrons (from 100 MeV to 100 GeV) by total containment of the electromagnetic showers they produce. It consists of two symmetric half-barrels and two endcaps (see Figure 4-5) of scintillating bismuth germanium oxide ($Bi_4Ge_3O_{12}$) crystals, about 11,000 in all. The crystals are 24cm-long ($22X_o$) truncated pyramids (of area 2×2 cm at the inner end and 3×3 cm at the outer end), arranged in cylindrical rings and pointing to the interaction region. BGO was chosen for its short radiation length (1.12 cm), high density (comparable with that of iron), relative radiation hardness and chemical stability, which favors a compact configuration with a long useful life. Each crystal was calibrated in a CERN SPS test beam, and the test-beam-observed resolutions at 180 MeV, 2 GeV and 50 GeV were 4%, 1.5% and 0.6% respectively [4-5]. The resolution as measured from di-electron events during actual LEP data-taking (see Figure 4-6) is $\Delta E/E = 1.34\%$.

The readout system for each crystal consists of two 1.5 cm^2 magnetic-field-insensitive silicon photodiodes glued to the rear face coupled to charge-sensitive amplifiers, the signals from which are digitized via wide-dynamic-range, short-memory-time ADC's. A xenon light monitor [4-6] is used to monitor the transparency of the crystals and
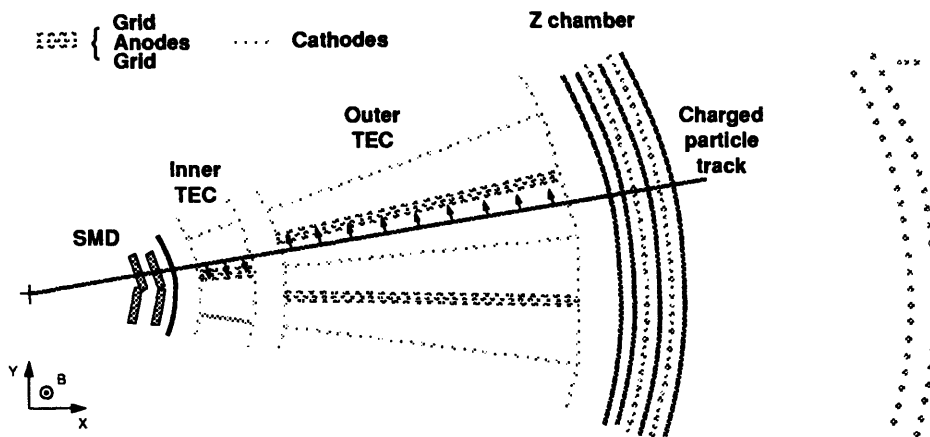
Figure 4-4: *View of the passage of a charged particle through inner and outer TEC sectors and z chamber, indicating the positions of the different types of wires.*
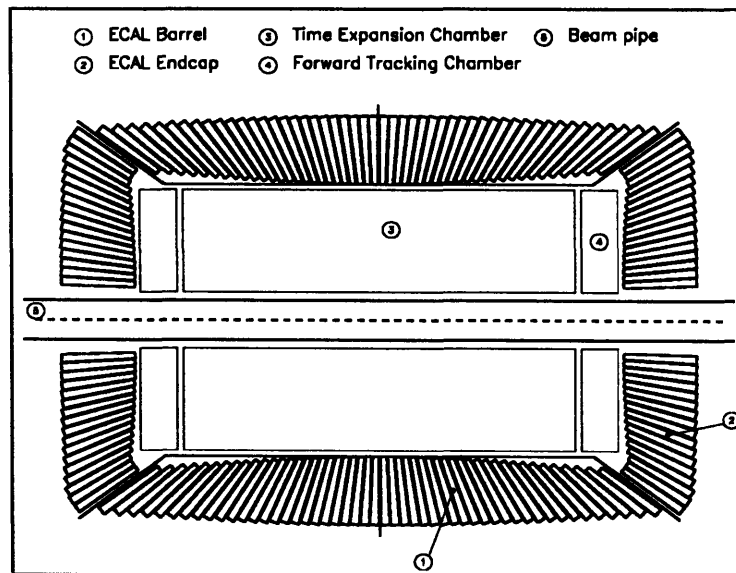
Figure 4-5: *A schematic view of the BGO electromagnetic calorimeter.*
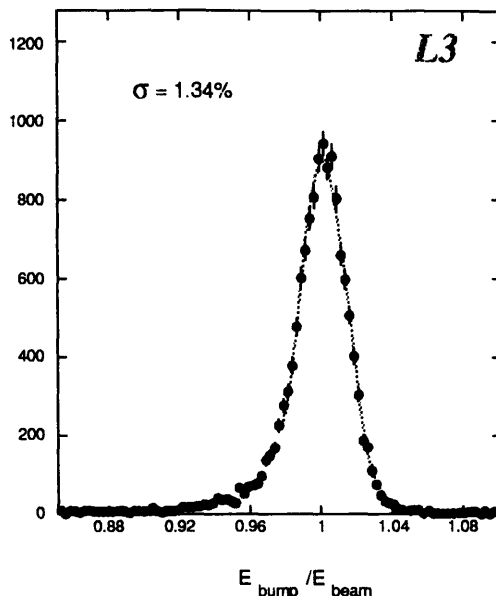
Figure 4-6: *Distribution of the ratio of electromagnetic clusters ("bumps") in the BGO to beam energy, from di-electron events, showing a resolution of $\sigma = 1.34\%$.*

to monitor their response relative to each other.

4.3 The Luminosity Monitors

The luminosity monitoring system (LUMI) [4-1, 4-4] is designed to track and measure the energy of electrons coming from small-angle Bhabha scattering events, which are counted to determine the integrated luminosity delivered to the L3 experiment. It consists of two identical cylindrical BGO electromagnetic calorimeters, each containing 304 crystals arranged in 8 rings parallel to the beam direction, along with two sets of proportional wire chambers (see Figure 4-7), on either side of the interaction point. The forward polar angular region covered, $0.998 \leq |\cos\theta| \leq 0.999$, corresponds to an effective Bhabha cross-section of ~ 100 nb.

4.4 The Scintillation Counters

The scintillation counters (SCI) [4-1, 4-4] reject cosmic muons which coincidentally pass through the interaction point by measuring the time-of-flight from that point relative to the beam crossing. This time, corrected for the expected finite time-of-flight of a vertex muon, is known as t_{cor} and should be zero for primary non-cosmic muons. The distribution of t_{cor} as measured from dimuon events is shown in Figure 4-8, and has a resolution of $\sigma = 0.46$ ns. Therefore muons with time-of-flight greater than ~ 2 ns ($\sim 4\sigma$) have less than a 1% probability of being primary vertex muons,
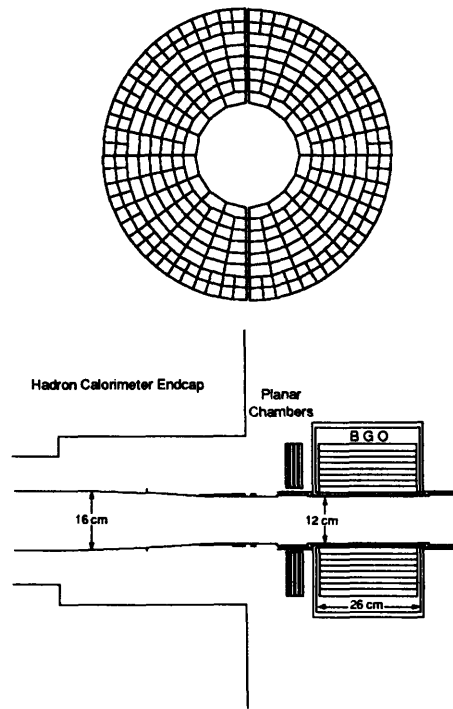
Figure 4-7: *(Top) End view of one of the two BGO calorimeters of the L3 luminosity monitor. (Bottom) Side view (parallel to the beam direction) of the layout of the components of the luminosity monitoring system.*

and cosmic veto criteria can be formulated on this basis. The scintillation light from the 30 single plastic counters is amplified by photomultiplier tubes at each end and the resulting signals are read out by TDC's.

4.5 The Hadronic Calorimeter

The fine-sampling hadronic calorimeter (HCAL) [4-1, 4-4] is designed to measure the energy of hadronic (strongly-interacting) particles by total containment of the cascades they produce through their inelastic collisions with nuclei. It consists of modules made of depleted uranium plates as the absorber medium indispersed with brass-tube proportional-wire chambers (which use 80-20 $ArCO_2$ as the drift gas) as the active medium. The tubes and wires are arranged in planes parallel and perpendicular to the beam direction in the barrel to allow position measurement in the ϕ and z directions, and azimuthally in the endcaps to allow measurement of θ. There are a total of 7968 chambers and 370000 wires. A typical module is shown in Figure 4-9. The modules are arranged into rings of 16 modules each (see Figure 4-10), 9 of which form the barrel and 3 (two inner and one outer) each endcap. For readout purposes the wires are grouped into "towers", of segmentation $\Delta\theta = 2^o$, $\Delta\phi = 2^o$, and are read out by ADC's. Calibration of the chambers is accomplished by gamma rays from the radioactive uranium [4-7].
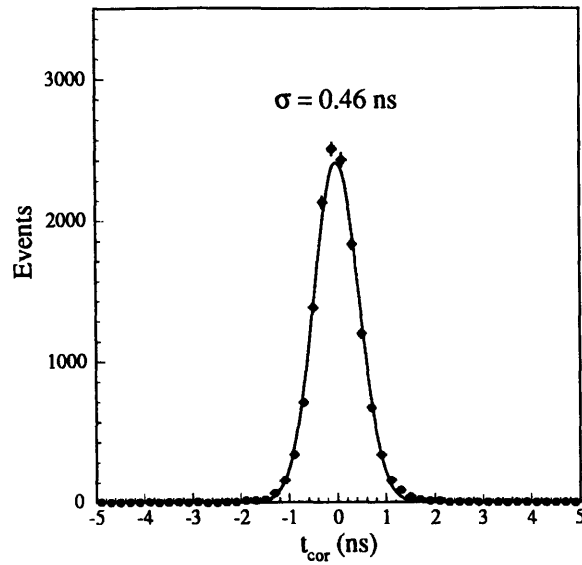
Figure 4-8: *Distribution of* t_{cor}, *the muon time-of-flight corrected for the finite tof of a vertex muon, as measured from dimuon events, showing a resolution of* $\sigma = 0.46$ *ns.*
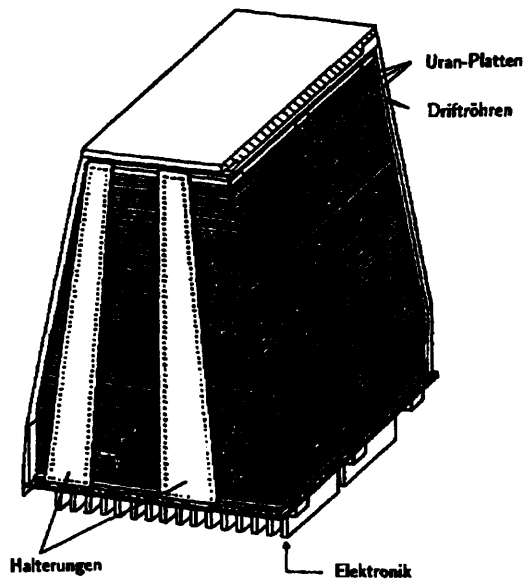
Figure 4-9: *A typical L3 hadronic calorimeter module; uranium absorber plates and brass-tube proportional-wire chambers are alternated in a "sandwich" structure.*
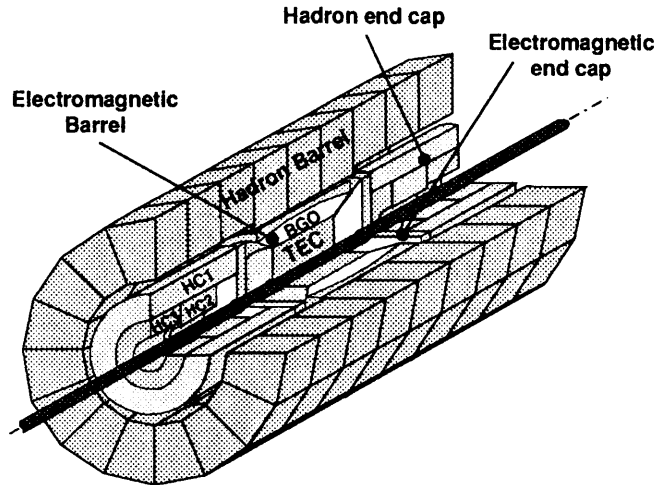
Figure 4-10: *A schematic of the L3 hadronic calorimeter, showing the arrangement of modules into barrel and endcaps.*

4.6 The Muon Chambers

The L3 muon chamber system (MUCH) [4-1, 4-4, 4-8] is designed to provide precise measurements of muon momenta by measurement of the bending of their trajectories in the field of the L3 magnet in the region outside the support tube. The system consists of two sets or "ferris wheels" of 8 "octants" (so-called because each covers 1/8 of the azimuth), which, located one behind the other lengthwise along the beam direction (see Figure 4-11), cover the entire cylindrical volume of the L3 detector. Each octant has three layers of "p" drift chambers (see Figure 4-12) which determine track coordinates in the bending $(R - \phi)$ plane, contained within a special mechanical structure: one inner chamber (MI) divided into 19 drift cells, two middle (MM) each with 15 cells and two outer (MO) chambers, each with 21 cells. The drift gas used is 61.5-38.5 Argon-Ethane, in which the drift velocity is $50\mu m/ns$ with a Lorentz angle of $18.8°$. Additional drift chambers known as Z chambers, with wires stretched perpendicular to the beam direction, are mounted on the top and bottom of the MI and MO chambers; they measure the z coordinate of the muon position. Each is composed of two layers of drift cells offset with respect to one another by one half-cell to help resolve left-right ambiguities. The drift gas is 91.5-8.5 Argon-Methane with drift velocity $35\mu m/ns$. The single-wire resolution for the z- chambers is better than $500\mu m$. The deformation of tracks due to multiple scattering is kept to a minimum $(< 30\mu m$ on the sagitta at 50 GeV) by the use of thin aluminum honeycomb to cover the MI chambers, amounting to only 0.9% X_o for the two layers. Both p- and Z-chambers are read out by amplifiers coupled to discriminators, and the data digitized

35

by TDC's.

Chambers Area : 900 m^2
Alignment : 30 μm
Total Wires : 250 000
TDC : 24 000

e$^-$

e$^+$

≈ 86 t complete

≈ 86 t complete

L3 - Central Muon Detector
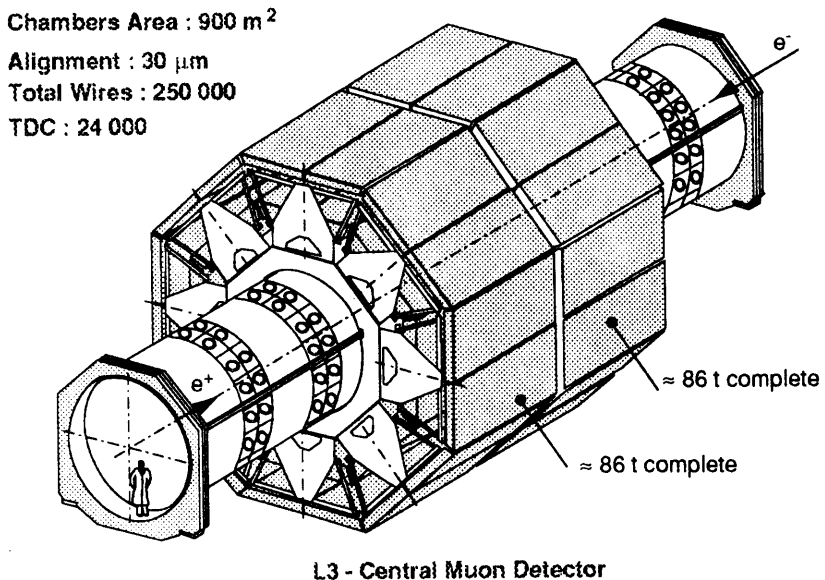
Figure 4-11: *A schematic of the L3 muon chamber system, showing the two "ferris-wheel" structures, each with 8 octants.*

MO

Beam Steering Element

MN

N$_2$ Laser

MI

Position Sensitive Photodiodes
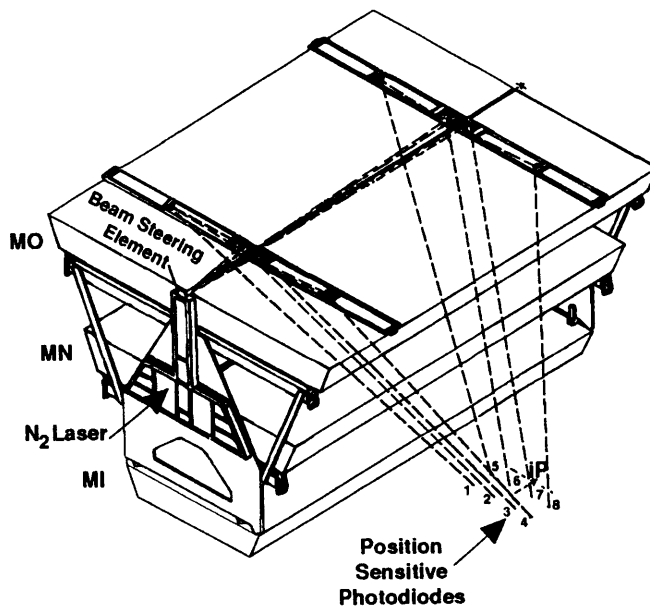
Figure 4-12: *A schematic of an octant. The three layers of drift chambers are shown along with the laser alignment-monitoring system.*

36

The cell design of the p chambers, shown in Figure 4-13, is optimized for a uniform nominal electric field of 1140 V/cm in the active region. The MI and MO chambers contain 16 sense (anode) wires/cell and the MM chambers 24, located at 9mm intervals and indispersed with field wires. The cathode wires located at 2.25mm intervals are located in planes 50.75mm from the sense wire plane. In addition, 8 guard wires are located beyond the extreme sense wires in each cell; their function is to equalize the drift time of the sense wires to within $\pm 0.2 ns$. All the wires are supported by precision pyrex glass and carbon fiber bridges aligned by an optical alignment system to better than $10 \mu m$. The single-wire resolution is better than $200 \mu m$.
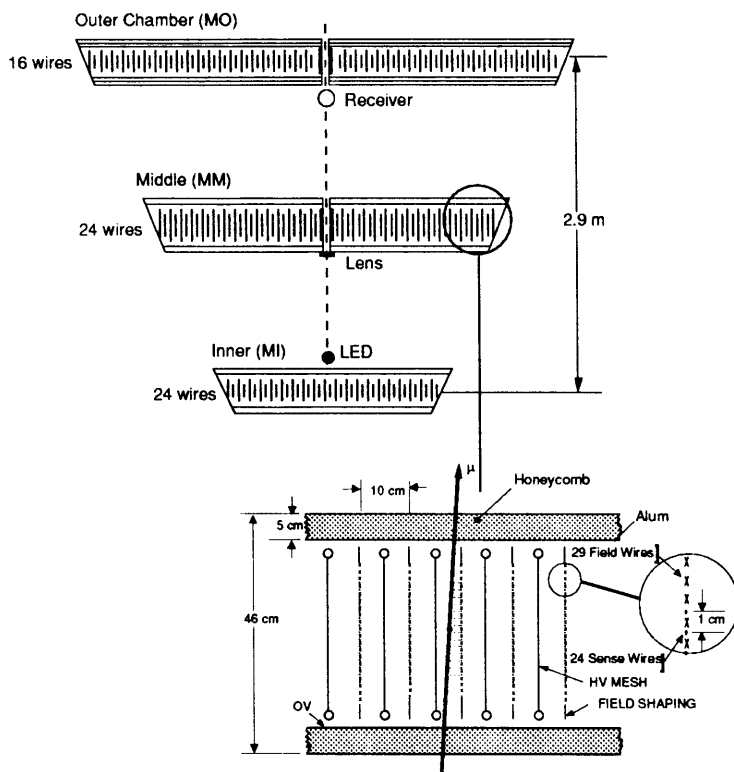
Figure 4-13: *The layout of the three layers of p drift chambers in an octant, highlighting the cell structure.*

Muon momentum is measured by the p-chambers in the following manner: the transverse momentum (p_T) of the muon is given by the following relation:

$$p_T = \frac{0.3BL^2}{8s} \tag{4.1}$$

where B[T] is the magnetic field (0.5T), L[m] is the radial distance over which the measurement is done (2.9m), and s[m] is the sagitta or deviation of the muon trajectory from a straight line (see Figure 4-14–the muon trajectory shown corresponds to that of a low-momentum muon for visibility). This last quantity is given by

37

$$s = x_{MM} - \frac{(x_{MI} + x_{MO})}{2} \qquad (4.2)$$

where x_{MM}, x_{MI} and x_{MO} are the measured positions of the muon track given by the middle, inner and outer chambers, and is 3.5 mm for a muon of p_T=45 GeV.
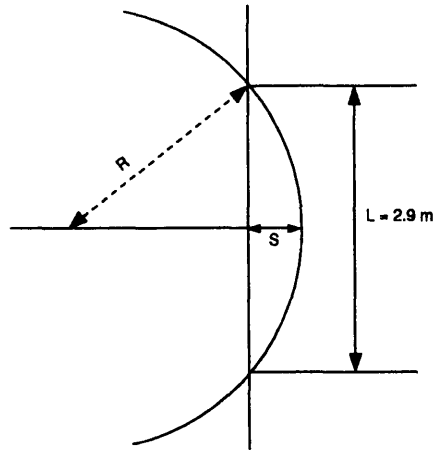
Figure 4-14: *Geometrical variables s and L used in calculation of the muon momentum. The muon trajectory shown is that of a low-momentum muon, for visibility.*

Alignment of the 3 layers of chambers within an octant is kept to within $30\mu m$ by the use of a laser beacon system to monitor the angle between the center lines at the two ends of the MO and MM chambers. This system is cross-checked by a built-in UV laser on each octant which sends a beam, simulating an infinite momentum vertex muon, through all three chamber layers by eight different trajectories to the interaction point, where the intensity and position of the beam centroid is measured and the sagitta, which should be zero for such "particles", calculated.

The momentum resolution obtained is $\Delta p/p = 2.47\%$ as determined during actual LEP data-taking from di-muon events (shown in Figure 4-15). In the regions of polar angle $0.719 \leq |\cos\theta| \leq 0.819$ muons only pass through two chambers, and a resolution of $\Delta p/p = 21.8\%$ is achieved.

4.7   The Trigger and Data Acquisition System

The function of the three-level L3 trigger system [4-1, 4-4, 4-9] is to reduce the rate of acquired data from the 45kHz beam crossing rate (90kHz in 8-bunch operation) to a workable few Hz, feasible for writing onto tape. It must decide whether or not an
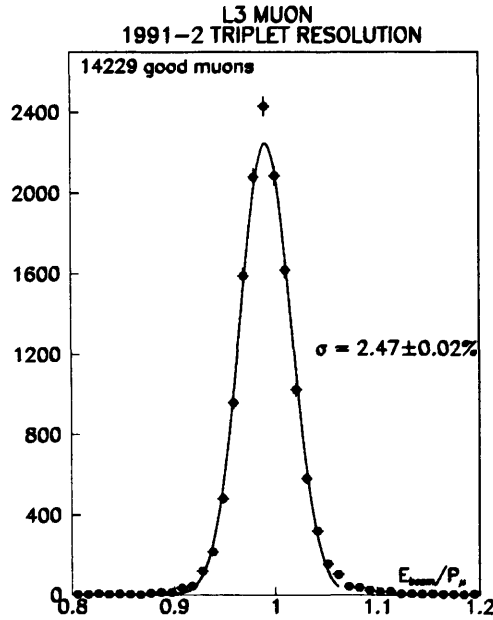
Figure 4-15: *Distribution of the ratio of beam energy to muon momentum, from dimuon events collected during 1991 and 1992, showing a resolution of* $\Delta p/p = 2.47\%$.

e^+e^- interaction took place, and reject noise and beam-gas events while preserving potentially "interesting" physics events, all within this $22.2(11.1)\mu s$ decision gate. To accomplish this, the readout electronics of each L3 subdetector provide, in addition to the main data acquired from each beam-crossing, a set of coarser (10^4 low-resolution channels as opposed to 10^5 high resolution) data known as "trigger data", capable of being processed by the Level 1 trigger system within a few micro-seconds. On a positive level-1 decision, the digitization of the main data begins; on a negative decision the readout electronics are cleared with no dead time incurred. The trigger data and level-1 decisions are passed to the level-2 trigger; on a positive decision there the digitized main data from the various subdetectors are combined for the first time into an "event" and sent to the level-3 trigger, where tighter requirements can be imposed. Events which pass level-3 are stored in a buffer on a central online computer (a VAX 7000), after which they are read and written on tape; some are selected for monitoring by one of ten programs. This computer is part of a larger online VAXcluster (L3ONCL), containing seperate machines for each subdetector which control the data-taking, monitor data quality and subdetector parameters, and perform calibrations.

Because of intermediate buffering between the trigger levels, the dead time of the L3 DAQ system is limited to the data digitization time, which, at a typical rate of less than 8Hz, results in a livetime of greater than 95%.

39

4.7.1 The Level-1 Trigger

The Level-1 trigger, whose operation was described above, consists of four hardwired subtriggers: the Energy, Muon, Scintillator and TEC triggers, for which a short description including typical rates is given below (the stated threshholds are typical; they may vary slightly from year to year). The decisions from all four subtriggers are OR'd together by the Trigger Control system (TBOX) to yield the overall level-1 decision, which it communicates to the Level 2 and 3 triggers. TBOX also sychronizes the trigger data digitization with the beam crossing, or alternatively sends a CLEAR signal in the event of a negative decision. In the event of a positive decision, the digitized main data are sent to subdetector, and then central FASTBUS Event Builder memories. As mentioned above the typical overall rate is less than 8Hz.

The Energy Trigger

The energy trigger divides the electromagnetic, luminosity, and hadronic calorimeters into cells or "superblocks" consisting of several crystals for the BGO or several towers for the hadronic calorimeter. Energy information from the superblocks serves as input to the following 8 subtriggers, the decisions from which are OR'd together to give the final energy trigger decision:

- Total Energy Trigger
  $E_{tot} \geq 25$ GeV

- Large Angle Energy Trigger ($18^o \leq \theta \leq 162^o$)
  $E_{ECAL} > 8$ GeV OR
  $E_{tot} > 15$ GeV

- Hit Trigger
  There must be at least two superblocks with energies above the following threshholds:

  - $E_{ECAL} > 2.5$ GeV
    $E_{HCAL} > 3.0$ GeV for all superblocks except the lowest ones in θ

  - $E_{ECAL} > 3.0$ GeV
    $E_{HCAL} > 4.0$ GeV for the lowest superblocks in θ ($\theta < 18^o$ for ECAL, $\theta < 17^o$ for HCAL)

- Cluster Trigger
  A cluster is defined as the sum of energies in superblocks at the same (θ, ϕ) coordinates. ECAL or HCAL clusters must have energies above the following threshholds, which are lower if a TEC track can be spatially associated with the cluster:

  - $E_{ECAL} > 6$ GeV
    $E_{HCAL} > 6$ GeV without an associated TEC track

- $E_{ECAL} > 2.5$ GeV

    $E_{HCAL} > 2$ GeV with an associated TEC track.

- Jet Trigger

  An energy trigger "jet" is formed by combining neighboring ECAL and HCAL clusters. The "jet" energies must satisfy the following threshhold, which again is lower if a TEC track can be associated to the jet:

  $E_{JET} > 6$ GeV

  $E_{JET} > 2$ GeV with an associated TEC track.

- Single Photon Trigger

  $E_{superblock} > 1$ GeV AND

  $E_{superblock}/E_{tot} > 0.8$

- Luminosity Trigger

  One of the two following conditions on the energy in the two BGO calorimeters of the luminosity monitor:

  $E_{1,2} > 16$ GeV OR

  $E_1 > 16$ GeV AND $E_2 > 5$ GeV

- Single Electron Trigger

  The energy in one of the two BGO calorimeters of the luminosity monitor must satisfy:

  $E > 32$ GeV

The overall rate is ~ 3 Hz.

The Muon Trigger

For the p-chambers, the trigger cells correspond to the actual physical drift cells (see prior description of the muon chambers in section 4.6), while, for the z-chambers, pairs of adjacent wires are grouped together. If the ensemble of the trigger cells which have registered hits can be identified with a possible "road" leading back to the interaction point, then the event is accepted if one of the following three subtrigger conditions is satisfied:

- Single Muon Trigger

  There must be hits in 2 out of the 3 p-chamber layers AND 3 out of the 4 z-chamber layers. This subtrigger covers the angular range of $|\cos\theta| \leq 0.719$.

- Dimuon Trigger

  There must be hits in 2 out of the 3 p-chamber layers and at least 1 z-chamber hit, AND hits in 2 out of the 3 p-chamber layers in one of the five opposite octants. This subtrigger covers the angular range of $|\cos\theta| \leq 0.819$.

- Small Angle Muon Trigger

  There must be a hit in 1 out of the 3 p-chamber layers and at least 1 z-chamber

41

hit AND the same conditions in one of the opposite three octants. The two "tracks" thus formed must be in the forward/backward region. This subtrigger covers the angular range of $|\cos\theta| \leq 0.914$.

The overall rate is ~ 9.5 Hz, which reduces to ~ 1.5 Hz after requiring at least one "in-time" scintillation counter to veto cosmic muons coincidentally passing through the interaction point.

The TEC Trigger

Each of the outer 24 TEC sectors (see section 4.1) serves as a trigger cell, and signals from the 14 anode wires in each are searched for "tracks". The trigger requires at least one pair of tracks, each with $|\vec{p}| > 150$ MeV, with acoplanarity angle less than $41°$. The typical rate varies between 1 and 4 Hz, depending on beam conditions.

The Scintillator Trigger

The nonzero signals from the 30 scintillation counters described in section 4.4 are used as trigger data. In addition to performing the cosmic-muon veto function described above, the scintillator trigger is used to identify high-multiplicity hadronic events by requiring that there be hits registered for at least 5 of the 30 counters, of which at least 2 must be back-to-back. The typical rate is ~ 0.2 Hz.

4.7.2 The Level-2 Trigger

The function of the microprocessor level-2 trigger is to reject background events such as noise and beam-gas events which were mistakenly accepted by level-1, as well as to reevaluate marginally accepted level-1 events (those accepted by only one of the four subtriggers). Level-2 receives the trigger data and level-1 decisions and looks for correlations between the subdetectors over a typical decision time of 5ms. If the level-2 decision is negative, the whole system is again cleared. If it is positive, the digitized data from each subdetector waiting in the central Event Builder memory is combined and sent along with the trigger data to level-3. Level-2 rejects on the average 20 to 30% of all events accepted by level-1, so the rate sent to level-3 is typically less than 6Hz.

4.7.3 The Level-3 Trigger

The level-3 trigger is made up of Vaxstation 4000/90's. Like level-2, it only evaluates events selected by only one of the four level-1 subtriggers with the exception that events selected only by the luminosity subtrigger of the energy trigger are automatically passed. Level-3 applies complex algorithms motivated by the level-1 trigger which originally selected the event, now able to apply tighter cuts to the finely digitized main data with a typical decision time of 100ms. The output rate, to be written to tape, is typically 2-3 Hz. The written events are stored in ZEBRA bank data structures.

42

Chapter 5

Data Sample and Event Reconstruction

5.1 The Data Sample

The data used in this analysis was collected by the L3 detector from April 1991 to November 1993. In addition to the data accumulated at center-of mass energies at or near the Z pole ($\sqrt{s} = 91.254$ GeV in 1991, 91.294 GeV in 1992 and 91.210 in 1993), which make up $\sim 55\%$ of the sample, included are data acquired by scanning around the peak value in 1991 (at 88.48, 89.47, 90.228, 91.222, 91.967, 92.966 and 93.716 GeV) and 1993 (at 89.452, 91.319 and 93.036 GeV). The average DAQ efficiency of the L3 detector during the time period covered by this study was $\sim 79\%$. The sample amounts to an integrated luminosity of $67.9 pb^{-1}$, corresponding to $\sim 1,921,000$ Z decays.

5.2 Measurement of Luminosity

The integrated luminosity delivered to the L3 experiment is determined by counting the number of small-angle Bhabha scattering ($e^+e^- \rightarrow e^+e^-(\gamma)$) events, N_{BB}, and is then given by the expression

$$\int \mathcal{L} \, dt = \frac{N_{BB}}{\sigma_{BB}} \tag{5.1}$$

where σ_{BB} is the theoretical Bhabha scattering cross-section which is known to 0.25%. The total systematic uncertainty in the luminosity measurement reaches 0.6% and includes 0.5% from experimental systematic errors (0.4% from the geometry of the luminosity monitor calorimeters, 0.3% from the Bhabha event selection, and 0.1% from Monte Carlo statistics) and 0.25% from theoretical uncertainty on the value of the Bhabha reaction cross-section. Full details of the luminosity analysis and calculation can be found in [5-1].

5.3 Data Reconstruction

The raw data that is written to tape as the final step in the L3 DAQ process (see section 4.7.3) consists only of hits in each subdetector. These are first reconstructed into local "objects" (such as tracks or clusters) using reconstruction routines specific to that subdetector; then the local objects are combined into global objects by a detector-wide routine, AXL3. All the routines are part of the main L3 reconstruction program, REL3. Following are two examples of globally reconstructed objects used extensively in this analysis:

- AMUI (Across-L3 reconstructed MUon)–First, hits in the individual layers of the p- or z- muon chambers are formed into local p- and z- track segments, which are in turn combined with equivalent segments from other layers to form a local muon track (MUI). If the MUI contains at least 2 out of 3 p-segments, AXL3 extrapolates it back through the inner detectors to the interaction point, correcting for $\frac{dE}{dx}$ energy losses in the calorimeters (which average ~ 2.6 GeV [5-2]) and combines it with a nearby track from the TEC (if one exists, which helps to resolve any remaining left-right ambiguities of the MUI), forming the AMUI. Full details of MUI and AMUI reconstruction are discussed in [5-3].

- ASRC (Across-L3 Smallest Resolvable Cluster)–These calorimetric clusters are formed by combining subclusters from both electromagnetic and hadronic calormeters, and along with AMUI's are used as input into the jet clustering algorithm described in the next chapter. First, the local ECAL and HCAL clusters (called EBMP's and HGCL's, respectively) are formed from hits in individual BGO crystals and HCAL readout towers which are above a certain threshhold (2 MeV for the ECAL, 9 MeV for the HCAL). In the case of the ECAL, the most energetic crystal is identified and grouped with all adjacent crystals to form an EBMP; for the HCAL all sets of contiguous hits are grouped into HGCL's. AXL3 then forms ASRC's from EBMP's and HGCL's at the same (θ, ϕ) direction. The spatial ASRC coordinates are redefined as the vector sum of those of all the component hits, referred to the interaction point as origin. The energies are adjusted using calibration constants known as G-factors. For a full discussion see [5-4].

Chapter 6

Event Selection

In the reaction $e^+e^- \longrightarrow Z \rightarrow \chi\chi'$, where the χ' decays via $\chi' \longrightarrow \chi + Z^*$, $Z^* \longrightarrow f\bar{f}$, the final state will consist of two of the lightest neutralinos χ accompanied by a fermion pair. The assumptions, stated in prior chapters, that the lifetime of the χ' is such that it decays within the detector, and that the χ as the LSP is stable (from R-Parity conservation) and interacts only weakly with matter, imply that the χ will be invisible and remain undetected, much like a neutrino. Therefore we expect the signature for a single χ' decay to consist of a fermion pair (either a lepton [electron,muon] pair or a hadronic jet pair or monojet, depending on the kinematics resulting from the differences between the Z, χ and χ' masses) recoiling against isolated missing energy (i.e. there is little calorimetric or track activity in the detector around the missing energy direction) and significant missing transverse momentum. The fermion pair may also be acoplanar[1] as a function of the particle mass differences. In the case of hadronic final states this signature can also be used to probe the reaction $e^+e^- \longrightarrow Z \rightarrow \chi'\chi'$ where each χ' decays according to $\chi' \longrightarrow \chi + Z^*$ and $Z_1^* \longrightarrow q\bar{q}$, $Z_2^* \longrightarrow \nu\bar{\nu}$ (i.e. the decay products of one of the Z^* invisible.)

This chapter presents, for each of the 3 χ' decay channels mentioned above, a detailed description of final state identification (i.e. pairs of electrons, muons, or hadronic mono- or di-jets), the selection used to distinguish events fitting the signature profile from those from background processes, and a discussion of the resulting signal selection efficiencies for values in the allowed region of the $(m_\chi, m_{\chi'})$ plane.

6.1 Event Preselection

After reconstruction by the L3 offline reconstruction program (see chapter 5), data events pass through a very loose preselection which selects and assigns events, according to their potential suitability, to seperate data sets (streams) corresponding to different areas of physics analysis. These then pass through a second-level preselection which requires that events fit into categories describing a variety of possible signatures considered rare or not expected within the context of the Standard Model.

---

[1]The acoplanarity angle between two objects is defined as the supplement of the angle between their projections onto the $R - \phi$ plane, transverse to the beam direction.

All the events used for this study were selected to one of the following 3 categories:

- Events with two or more jets, acolinear[2] ($\theta_{acol} \geq 15^o$) with some missing energy (6 GeV$\leq E_{vis} \leq$ 80 GeV): This eliminates the majority of events resulting from the Standard Model processes $e^+e^- \to Z \to q\bar{q}$ or $\tau^+\tau^-$, in which the two jets are expected to be back-to-back and the visible energy expected to closely approximate the center-of-mass energy (here, $M_Z \sim$ 91.2 GeV).

- Events with only one jet, with no tracks within a cone of 30^0 half-angle in the $R - \phi$ plane opposite the jet direction: The requirement on tracks opposite the jet direction helps to supress "fake" monojet events where charged particles on the opposite side of the detected jet have passed through dead calorimetric regions or acceptance gaps, but have nevertheless produced tracks in the TEC.

- Di-lepton events (e,μ) with isolated significant missing momentum ($|\vec{p}| > 3$ GeV), again no tracks within a cone of 30^0 half-angle of the momentum imbalance direction, calorimetric energy within this cone ≤ 3 GeV) and energy (same limit on visible energy as in multi-jet case above): As with the multi-jet events, Standard Model dilepton events ($e^+e- \to Z \to l^+l^-$) are expected to have no missing energy, and the requirement of no tracks within 30° half-angle of the missing energy direction eliminates many events "faking" this condition.

In addition, all three of the above categories require that $|\cos\theta_{imb}| < 0.9$, i.e. that the polar angle of the momentum imbalance vector not point within 25° of the beam direction. This is intended to veto events where final state particles may escape down the beam pipe, again "faking" missing energy.

Jets are constructed during this second-level preselection from calorimetric clusters and identified muons from the muon chambers using the LUCLUS [6-1] jet clustering algorithm with the d_{join} option, which groups objects into jets based on their relative p_T with respect to a common jet axis. For each pair of objects, the quantity d_{ij}, which is the p_T of either object with respect to the direction given by the sum of their 3-momenta, is calculated. For small θ_{ij} (the 3-space angle between the objects) this can be approximated as:

$$d_{ij} \approx \frac{|\vec{p_i} \times \vec{p_j}|}{|\vec{p_i} + \vec{p_j}|} \tag{6.1}$$

The two objects with the smallest d_{ij} are then vectorially added to form a new object, provided that $d_{ij} < d_{join}$. After each such joining, all the original objects are reassigned to the "closest" (in terms of d_{ij}) new object. This process continues iteratively until $d_{ij} > d_{join}$ for all possible pairs of objects. The LUCLUS/d_{join} algorithm has some advantages over some other algorithms which use pairwise invariant mass as

---

[2]The acolinearity angle between two objects is defined as the supplement of the 3-space angle between them.

a "distance measure" between jets as opposed to an upper limit on an object's relative p_T: These tend to cluster low-momentum objects first, and then high-momentum objects around these, which may introduce inaccuracies in calculation of jet directions since it is the high-momentum objects in the jet whose directions should primarily influence the jet direction. Another result might be the presence of one jet artificially containing all the low-momentum particles. For this analyisis the parameter d_{join} has been set as follows:

$$d_{join} = max(2.5\text{GeV}, 0.1 \times E_{vis}) \qquad (6.2)$$

where E_{vis} is the amount of visible energy recorded in the detector.

Events surviving the second level of preselection then proceed to a seperate final selection for each fermionic final state, as described below.

6.2 Monte Carlo Simulation of Neutralino Events and Background Processes

In order to study in detail the signature profile of neutralino decay events, formulate the final selection for each final state channel, and eventually calculate the signal selection efficiency, this analysis made use of the STALINO [6-2] Monte Carlo generator, which simulates the production of $\chi\chi'$ or $\chi'\chi'$ pairs and the subsequent decay of the χ' via various modes, including $\chi' \longrightarrow \chi + Z^*$, $Z^* \longrightarrow f\bar{f}$. This generator can operate in both model-independent (accepting as inputs explicit values of m_χ and $m_{\chi'}$) and MSSM (accepting as inputs explicit values of the 3 model parameters M, μ and $\tan\beta$) modes. Other generators, depending on the specific final state considered and detailed below, were used to estimate the background. In all cases, the generated events were fully simulated in the L3 detector using the L3 detector simulation [6-3], which in addition to the detector geometry includes the effects of energy loss, multiple scattering, showering and decays in the detector materials and in the beam pipe. They were then reconstructed using the same L3 offline reconstruction program as the data events, and subjected to the same two-level preselection as described above.

6.3 Selection of Leptonic Final State Events

6.3.1 Final State Identification

Identification of Electron Pair Final State Events

Electrons are identified as electromagnetically showering particles in the BGO calorimeter. They distinguish themselves from photons only in being accompanied by a track in the TEC, indicating that they are charged.

To evaluate the electromagnetic vs. hadronic character of a cluster in the BGO crystals, shower profile information is used: For an isolated electromagnetic shower,

the ratio of the energies deposited in a 3×3 crystal array to that in a 5×5 array both centered on the most energetic crystal in the cluster, $\sum_9 / \sum_{25}$, is approximately Gaussian [6-4] with $\mu = 1.0$ and $\sigma = 1\%$ (A position-dependent leakage correction to both measurements has been applied). For strongly-interacting particles such as pions the transverse shower shape is much more diffuse (see Figure 6-1).

Shower Shapes in the BGO
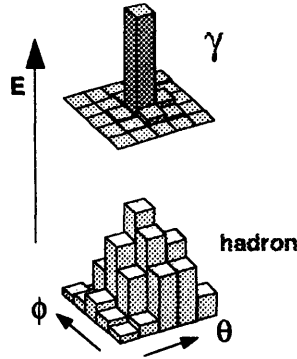
Figure 6-1: *Typical energy deposition in a 5×5 BGO crystal array for a photon (above) and a hadron(below)*

This analysis considers a BGO cluster to be an electron if:

- $E > 2$ GeV where E is the cluster energy

- $\sum_9 / \sum_{25} \geq 0.9$ if $N_{clus} < 15$
  ≥ 0.92 if $N_{clus} > 15$
  where $\sum_9 / \sum_{25}$ has been defined above and N_{clus} is the total number of calorimetric clusters

- There is a TEC track within $\delta\phi = 40mr$ of the BGO cluster if $N_{clus} < 15$, and within $\delta\phi = 20mr$ if $N_{clus} > 15$. For high-multiplicity events, the matching requirement must be tighter to ensure matching tracks to the correct cluster.

This analysis also imposes requirements on the quality of the tracks in the TEC, which are considered to have represented the passage of a charged particle if:

- The number of hits > 30

- The distance of closest approach (DCA) to the beam axis in the $R - \phi$ plane< 5mm

- The track transverse (with respect to the beam direction) momentum> $100MeV$.

48

Events are selected and classified as electron pair final-state events if they satisfy all of the following requirements:

- There are exactly 2 good electrons as defined above

- There are exactly 2 good TEC tracks as defined above

- The event contains no reconstructed muons

- The event contains no more than 10 electromagnetic clusters with $E > 100MeV$. This last requirement helps to assure a sample of "clean" events

These events proceed to a final selection, which will be described below.

Identification of Muon Pair Final State Events

Muons are identified as track segments in the 3 "P" ($R - \phi$ plane) and 4 "Z" ($R - Z$ plane) layers of the L3 muon chambers (MUCH). At the time of event reconstruction, if there exist at least 2 out of 3 P-segments, the segments are combined into one track and extrapolated back through the inner detectors to the interaction region, and further combined with TEC track information (see prior chapter on Data Sample and Reconstruction) as needed to form a single reconstructed muon object (AMUI).

For this study, only primary muons originating at the interaction point were of interest. However, some reconstructed muons may have other origins:

- "Punchthrough" particles–These are strongly-interacting secondarily-produced particles such as pions and kaons which have enough energy to "punch through" the muon filter and leave tracks in the muon chambers which are reconstructed as good muons. However as secondary particles their distance of closest approach to the interaction point is much higher than that of primary muons which originate at the vertex.

- Decay muons–Sometimes the pions and kaons mentioned above do not themselves penetrate to the muon chambers, but muons produced as a result of their decays do. They are also characterized by a large distance of closest approach (DCA) to the beam axis in the $R - \phi$ plane.

- Cosmic muons–Most cosmic-ray muons also "miss" the interaction point, and thus have large DCA's. But some coincidentally pass through the interaction point. However, the probability that these will pass coincident with the beam crossing time is extremely low. Therefore their measured time-of-flight (ToF) between the interaction point and the ring of scintillation counters located between the electromagnetic and hadronic calorimeters will be large compared to that of primary muons, that is, several σ away from the measured primary muon value (whose distribution was shown before in Figure 4-8), whose resolution is $\sigma = 0.46$ ns.

In order to veto these non-primary muons, the following requirement is imposed on reconstructed muons:

ΔR_{vertex} and Δz_{vertex} (the R and z coordinates, respectively of the DCA) are both
$$\leq 100mm$$

Events are then selected and classified as muon pair final-state events if:

- There are exactly 2 good reconstructed muons as defined above

- There is at least one but no more than 2 good TEC tracks (defined as for the case of electron-pair events above)

- There is at least one scintillator with ToF < 3 ns (relative to the beam crossing). This should veto events consisting only of cosmic muons.

- As with the electron-pair events, there should be no more than 10 electromagnetic clusters with $E > 100 MeV$.

The selected events proceed to the final selection described below.

6.3.2 Final Selection: $Z \rightarrow \chi\chi', \chi' \longrightarrow \chi + Z^* \longrightarrow \chi l^+ l^-$

The expected signature of a neutralino decay in this case is a pair of (possibly acoplanar) leptons recoiling against isolated missing energy and significant missing transverse momentum. However, there are processes within the Standard Model which, under certain conditions, can mimic this behavior. These are listed below along with the Monte Carlo generators used to study them and to formulate the final selection (along with the generated signal Monte Carlo (STALINO) events):

- $e^+e^- \longrightarrow ee(\gamma), \mu\mu(\gamma), \tau\tau(\gamma)$, i.e. leptonic decays of the Z or electromagnetic scattering accompanied by initial/final-state radiation. If the photon(s) escape detection via passage through an acceptance gap, dead region, or the beam pipe, there will be "missing" energy, and in the case of $\tau\tau$, possibly significant "missing p_T". To study the $ee(\gamma)$ process the generator BHAGENE3 [6-5] was used; for $\mu\mu(\gamma)$ and $\tau\tau(\gamma)$, the KORALZ [6-6] generator.

- Z, γ (s-channel) or $\gamma\gamma, \gamma Z$ or ZZ (t-channel) $\longrightarrow ee\mu\mu, eeee, \mu\mu\mu\mu, ee\tau\tau$, the so-called "four-fermion" processes. These processes may proceed through any of the 4 Feynman diagrams shown in figure 6-2. In this case it is two of the final state electrons or muons which may escape into acceptance gaps, dead regions, down the beamline, or a combination. The remaining fermion pair may show some "acoplanarity". To study these events the DIAG36 [6-7] generator was used.

Table 6.1 shows, for each background process, the amount of equivalent luminosity generated, and the equivalent percentage of the statistics required to equal that for the 1991-1993 data sample used.
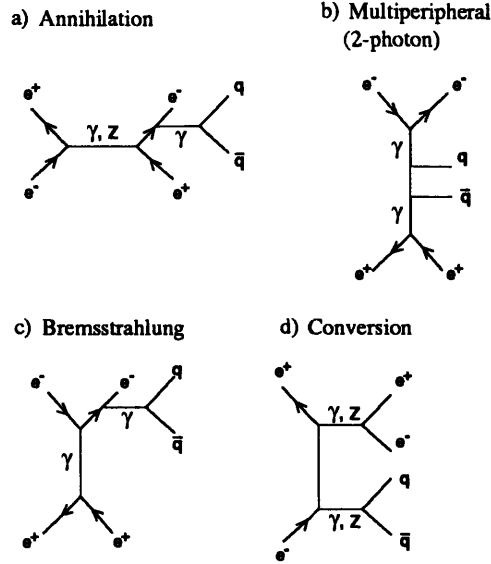
Figure 6-2: *The four possible Feynman diagrams through which "four-fermion" processes constituting background to neutralino production and decay(ee$f\bar{f}$ final state) can proceed, shown here for $f = q$ although possible for all fermions.*

Z Leptonic Decay Processes with Initial/Final State Radiation

Process	$\int \mathcal{L}$ dt Generated [pb^{-1}]	% of 1991-1993 Statistics
$ee(\gamma)$	49.30	72.6
$\mu\mu(\gamma)$	82.5	121.5
$\tau\tau(\gamma)$	206.21	303.7

Four-Fermion Processes

Process	$\int \mathcal{L}$ dt Generated [pb^{-1}]	% of 1991-1993 Statistics
$ee\mu\mu$	42.57	62.7
$ee(ee)$	14.26	21.0
$\mu\mu(\mu\mu)$	99.88	147.1
$(ee)\tau\tau$	55.27	81.4

Table 6.1: *Background Monte Carlo samples and statistics for fermionic final states*

51

A final selection was optimized to veto events from the above background processes while preserving events fitting the signature profiles, as represented by the signal Monte Carlo, for a variety of χ and χ' mass combinations. The following requirements were imposed:

- $\not{p}_T > 4$ GeV where $\not{p}_T$ is the total missing transverse (to the beam direction) momentum. Figure 6-3 shows the distributions of this variable for the electron and muon-pair final states for data, Monte-Carlo-simulated events from background processes and for two signal mass combinations $(m_\chi, m_{\chi'})$. [3] This cut removes much of the background from $Z \to eell$ and to some extent, $Z \to ll(\gamma)$. As shown, it cannot be made any tighter without compromising possible signal detection in cases where there is little visible energy, i.e. where both the χ and χ' are close in mass and where $m_\chi + m_{\chi'} \sim m_Z$. The apparent excess (ranging from $\sim 2 - 4\sigma$) in the electron-pair final state of data events in the range 9 GeV$< \not{p}_T < 30$ GeV corresponding to the regime occupied by $\tau\tau(\gamma)$ and $ee(\gamma)$ events is probably due to dead crystals in the electromagnetic calorimeter which have not been included in the detector simulation. The energy from one electron is lost in the dead crystal, leading to "fake" transverse momentum imbalance. The acoplanarity distribution that follows (Figure 6-4) supports this hypothesis by showing that the "excess" falls largely in the first and second bins, indicating a back-to-back topology.

- $\Phi_{acop} > 10^\circ$ where Φ_{acop} is the acoplanarity angle between the two final-state leptons (the supplement of the angle between their projections on the $R - \phi$ (transverse to the beam) plane), shown in Figure 6-4 for data, background Monte Carlo events and for two neutralino mass combinations. This is particularly effective against background from $Z \to \tau\tau(\gamma)$ (due to the high Lorentz boost of the τ system the decay products are highly collimated and hence strongly favor a back-to-back topology) and to some extent $Z \to ll(\gamma)$ since in most cases the "missing" initial- or final- state photon is emitted in a direction close to the emitting lepton direction. Once again the cut cannot be made too tight because the only kinematical case resulting in uniformly large acoplanarity of the χ' decay products is that where the decaying system is highly boosted, i.e. where the sum of the χ and χ' masses are very small compared to m_Z. Otherwise, as shown in the figure, the acoplanarity distribution is quite flat. Note that the slight "excess" of data events described above is eliminated by this cut.

- $E_{l_1} + E_{l_2} > 12$ GeV, the sum of the two final-state lepton energies. As shown in Figure 6-5, this cut eliminates most of the remaining four-fermion background,

---

[3] In all distributions, the number of background Monte Carlo events has been normalized to the total integrated luminosity of the data sample ($67.9 \ pb^{-1}$). The signal Monte Carlo events have been normalized arbitrarily for visibility. The actual predicted event rates are very model-dependent however and will be discussed in section 7.2.1.
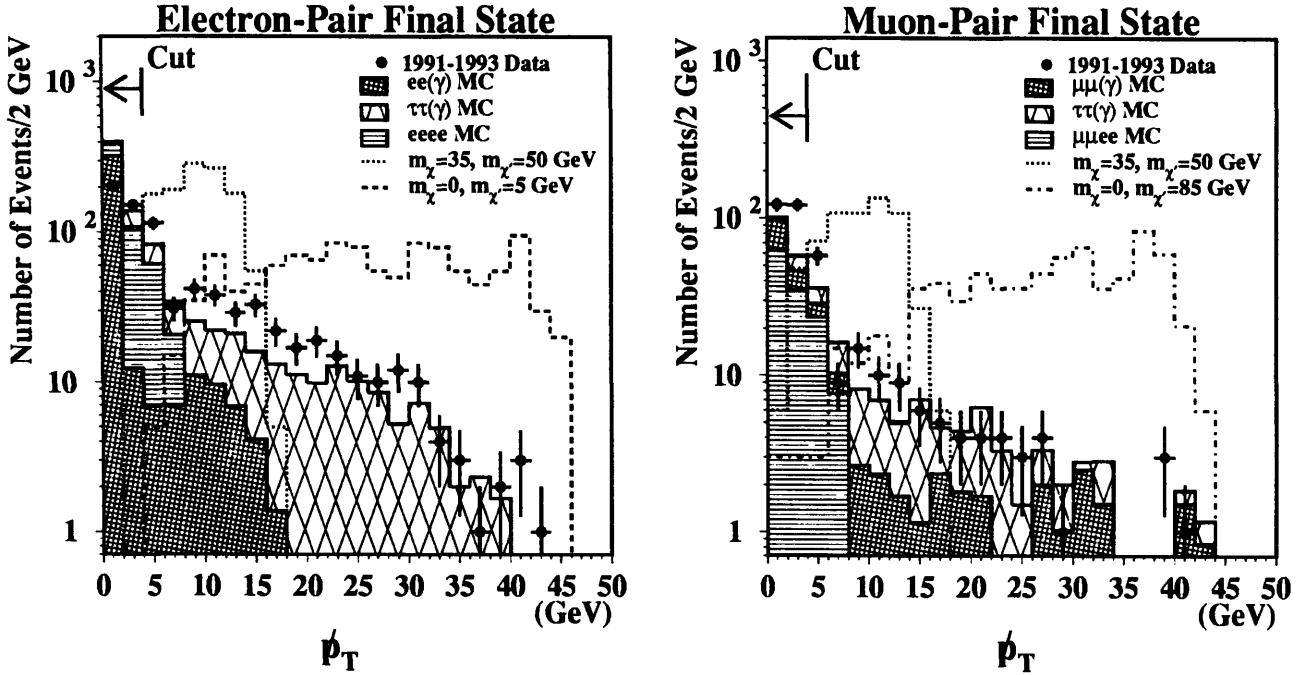
Figure 6-3: *Distribution of missing transverse momentum for (left) electron- and (right) muon-pair final states, for data, Monte-Carlo background processes and Monte-Carlo signal events for selected neutralino mass combinations.*
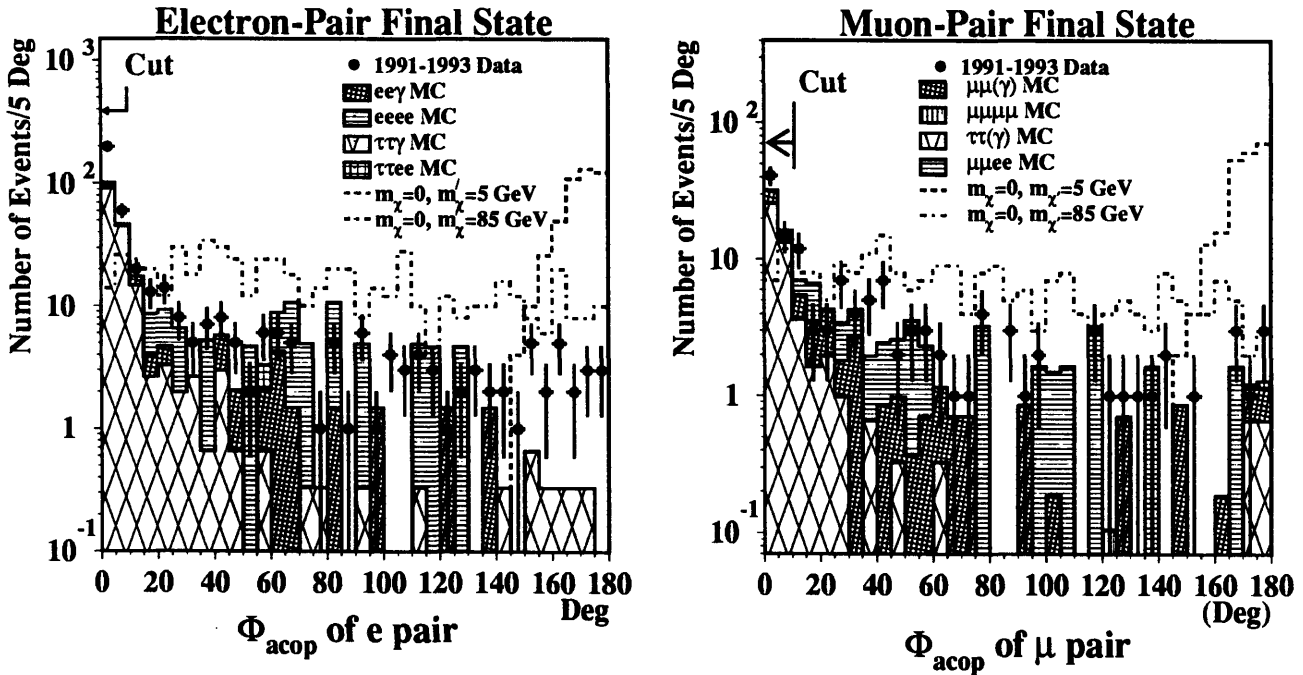
Figure 6-4: *Distribution of acoplanarity angle (supplement of angle between projections of two particle vectors on the $R - \phi$ (transverse to the beam) plane) for (left) electron- and (right) muon-pair final states, for data, Monte-Carlo background processes and Monte-Carlo signal events for selected neutralino mass combinations.*

since the extra pair of leptons resulting from these processes tends to be very low in energy. However the correlation of this cut to visible energy once again limits the threshhold that can be set, if only one selection is to be maintained for all ranges of kinematical variables.
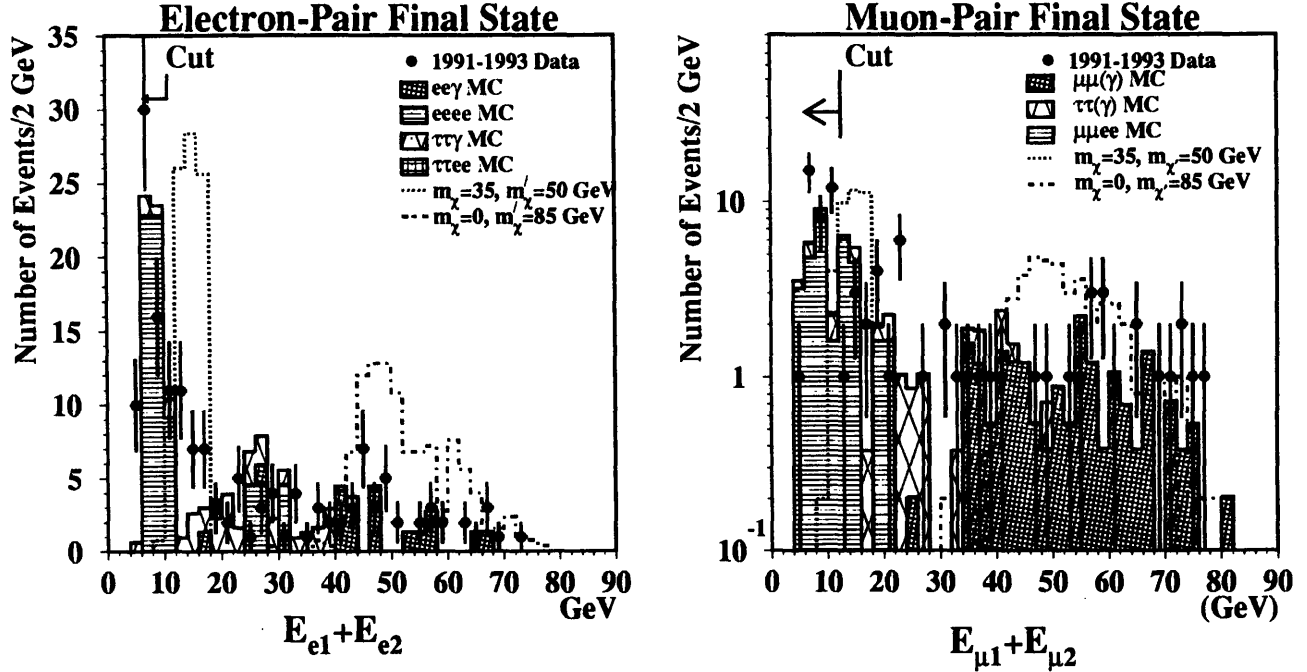
Figure 6-5: *Distribution of sum of final-state lepton energies for (left) electron- and (right) muon-pair final states, for data, Monte-Carlo background processes and Monte-Carlo signal events for selected neutralino mass combinations.*

- $\Phi_{acop} > 45°$ OR $E_{l_1} + E_{l_2} > 40$ GeV. Figures 6-6 and 6-7 show the distribution of data and Monte Carlo-generated events from background processes in the lepton-pair-energy/acoplanarity phase space. A good agreement is seen between the kinematics of the data and the ensemble of the background process distributions. The figures show the clustering of the $Z \to \tau\tau(\gamma)$ and 4-fermion $eeee$ events in the low-acoplanarity, low-energy region. Figures 6-8 and 6-9 show the distribution of Monte-Carlo generated signal events for three kinematically representative combinations of neutralino masses superposed on the data and background events. The cut was chosen to eliminate most of the remaining $Z \to \tau\tau(\gamma)$ and $eeee$ background, relying on the fact that the τ decay products are both fairly back-to-back and generally relatively low in energy, while preserving signal selection efficiency as indicated. In cases of low visible energy this cut cannot always distinguish between the kinematic behavior of lepton pairs arising from neutralinos and those from τ pairs through a portion of the phase space.
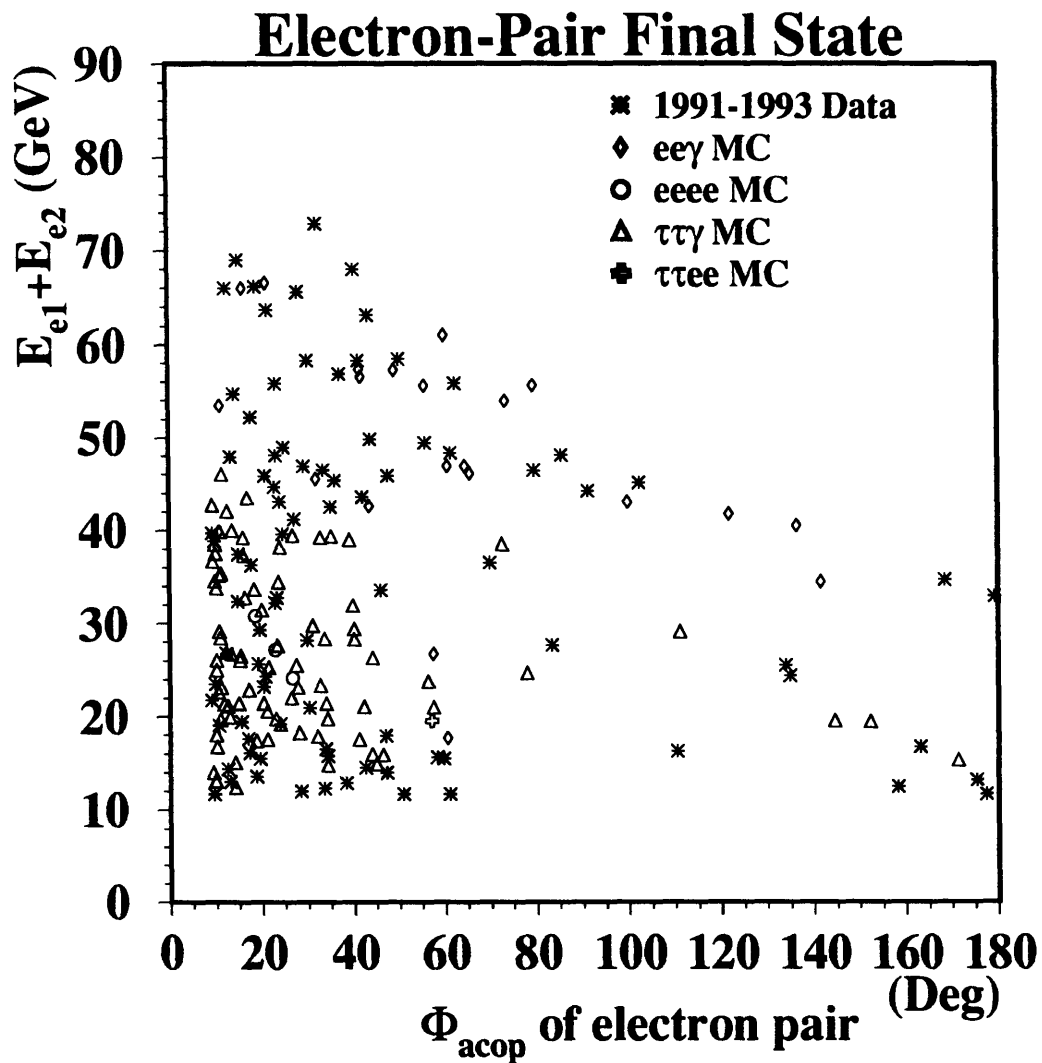
Figure 6-6: *Distribution of sum of final-state electron energies vs. acoplanarity angle for data and Monte-Carlo background processes.*
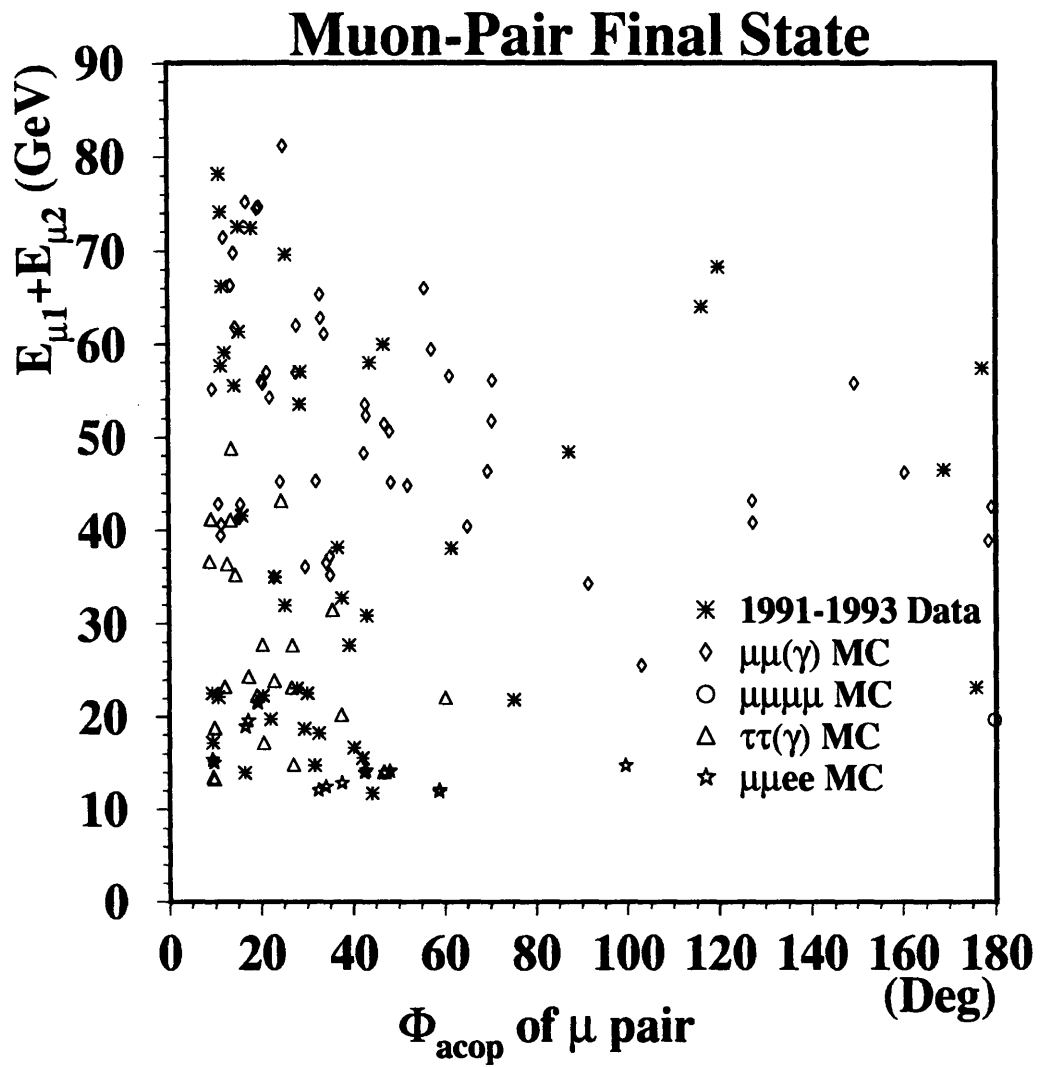
Figure 6-7: *Distribution of sum of final-state muon energies vs. acoplanarity angle for data and Monte-Carlo background processes.*
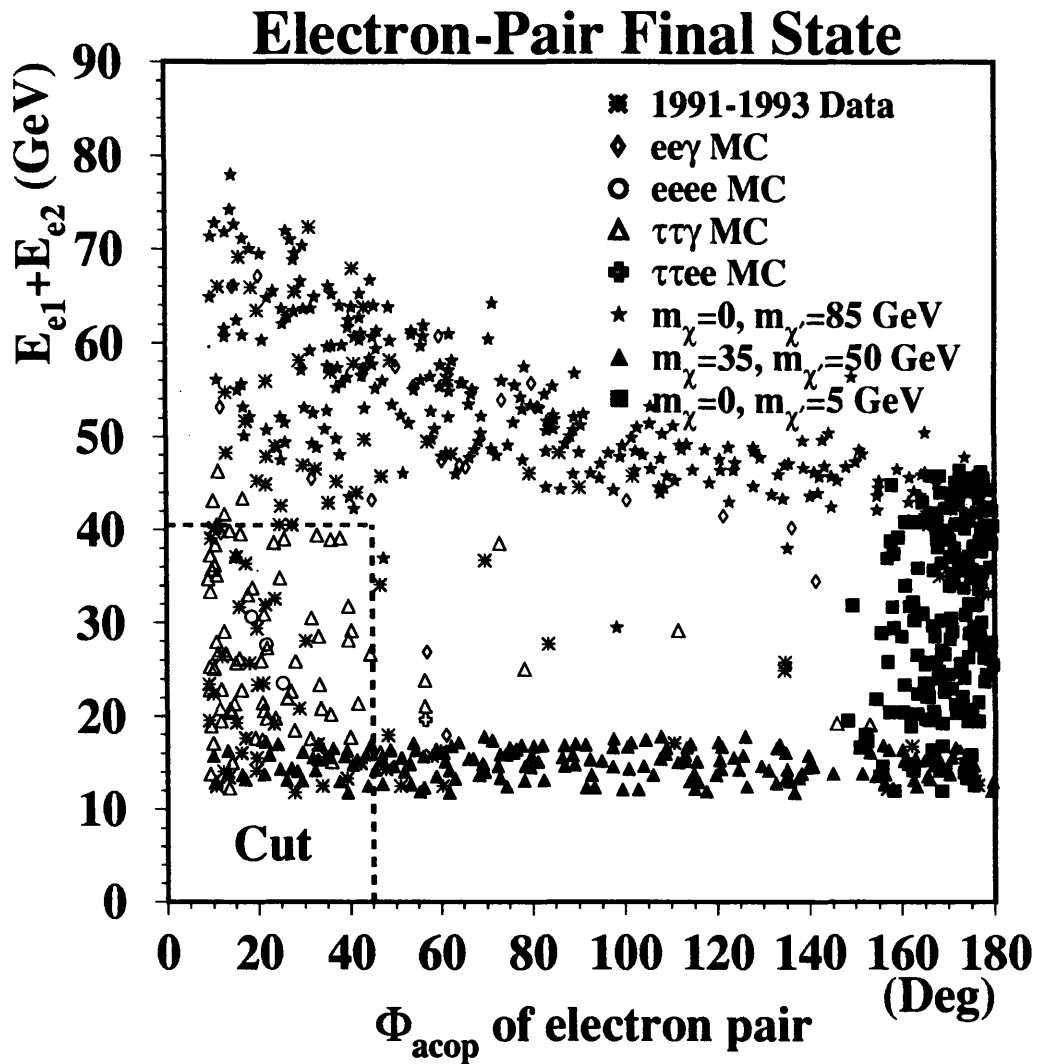
Figure 6-8: *Distribution of sum of final-state electron energies vs. acoplanarity angle for data and Monte-Carlo background processes with Monte-Carlo signal events for selected neutralino mass combinations superposed.*

Muon-Pair Final State

$E_{\mu1}+E_{\mu2}$ (GeV)

90
80
70
60
50
40
30
20
10
0

✱ 1991-1993 Data
◊ $\mu\mu(\gamma)$ MC ★ $m_\chi=0$, $m_{\chi'}=85$ GeV
○ $\mu\mu\mu\mu$ MC ▲ $m_\chi=35$, $m_{\chi'}=50$ GeV
△ $\tau\tau(\gamma)$ MC ■ $m_\chi=0$, $m_{\chi'}=5$ GeV
★ $\mu\mu ee$ MC

Cut

0 20 40 60 80 100 120 140 160 180
(Deg)

Φ_{acop} of μ pair

Figure 6-9: *Distribution of sum of final-state muon energies vs. acoplanarity angle for data and Monte-Carlo background processes with Monte-Carlo signal events for selected neutralino mass combinations superposed.*

- Limits on energy deposited in the electromagnetic (ECAL), hadronic (HCAL) calorimeters and luminosity monitor (FLUM): The remaining background consists largely of $Z \to ll(\gamma(\gamma))$ events with one or more visible or "missing" (i.e. undetected due to their passage through acceptance gaps, temporarily dead regions, or down the beam pipe) photons. The following cuts successfully remove virtually all of this background.

  - Limits on energy in the calorimeters:

    * $|E_{ECAL} - E_{2e}| \leq 2$ GeV where E_{2e} is the sum of the electron energies, for the electron-pair final state
      $E_{ECAL} \leq 5$ GeV for the muon-pair final state

    * $E_{HCAL} \leq 3$ GeV for the electron-pair final state
      $E_{HCAL} \leq 10$ GeV for the muon-pair final state

    * There should be no energy deposit in the luminosity monitor.

    These cuts target visible photons by limiting, in the case of the dielectron final state, the total amount of energy deposited in the ECAL not arising from the electron pair, or, in the case of the dimuon final state, above the level expected from two MIPs. However, if these photons pass through ECAL acceptance gaps (notably those between $37^\circ - 42^\circ$ and $138^\circ - 142^\circ$) they will nevertheless with high probability deposit some energy in the HCAL, and can be rejected on that basis. The higher limit for the muon-pair final state again allows for the interaction of muons as MIPs in the HCAL. Figure 6-10 shows the distributions of these two variables and the effectiveness of this cut. The check for energy in the luminosity monitor covers the case of photons escaping down the beam pipe. The case of two radiative photons is also addressed by these cuts, since the missing energy direction no longer represents that of one particle and therefore the check on calorimetric energy surrounding it, described below, does not help.

  - Limits on calorimetric energy in the vicinity of the missing energy direction:

    * $E_{ECAL,30} \leq 200$ MeV where $E_{ECAL,30}$ is the energy in the electromagnetic calorimeter in a 3-space cone of 30° half-angle around the missing energy direction

    * $E_{HCAL,30} \leq 1$ GeV where $E_{HCAL,30}$ is the energy in the hadronic calorimeter in a 3-space cone of 30° half-angle around the missing energy direction

    These cuts target "missing" photons which, even after passing through non-hermetic or temporarily dead regions, in most cases still leave "footprints", small deposits of energy in neighboring active regions. However, in order to apply these limits and avoid vetoing signal events the threshholds must be set above the normal noise pedestals present in the calorimeters. These were estimated by studying calorimetric energy levels in beam-gate events. Since the procedure and threshholds obtained were common to all channels, and since it was also used to adjust signal selection efficiencies, it will be described later in section 6.5.1.
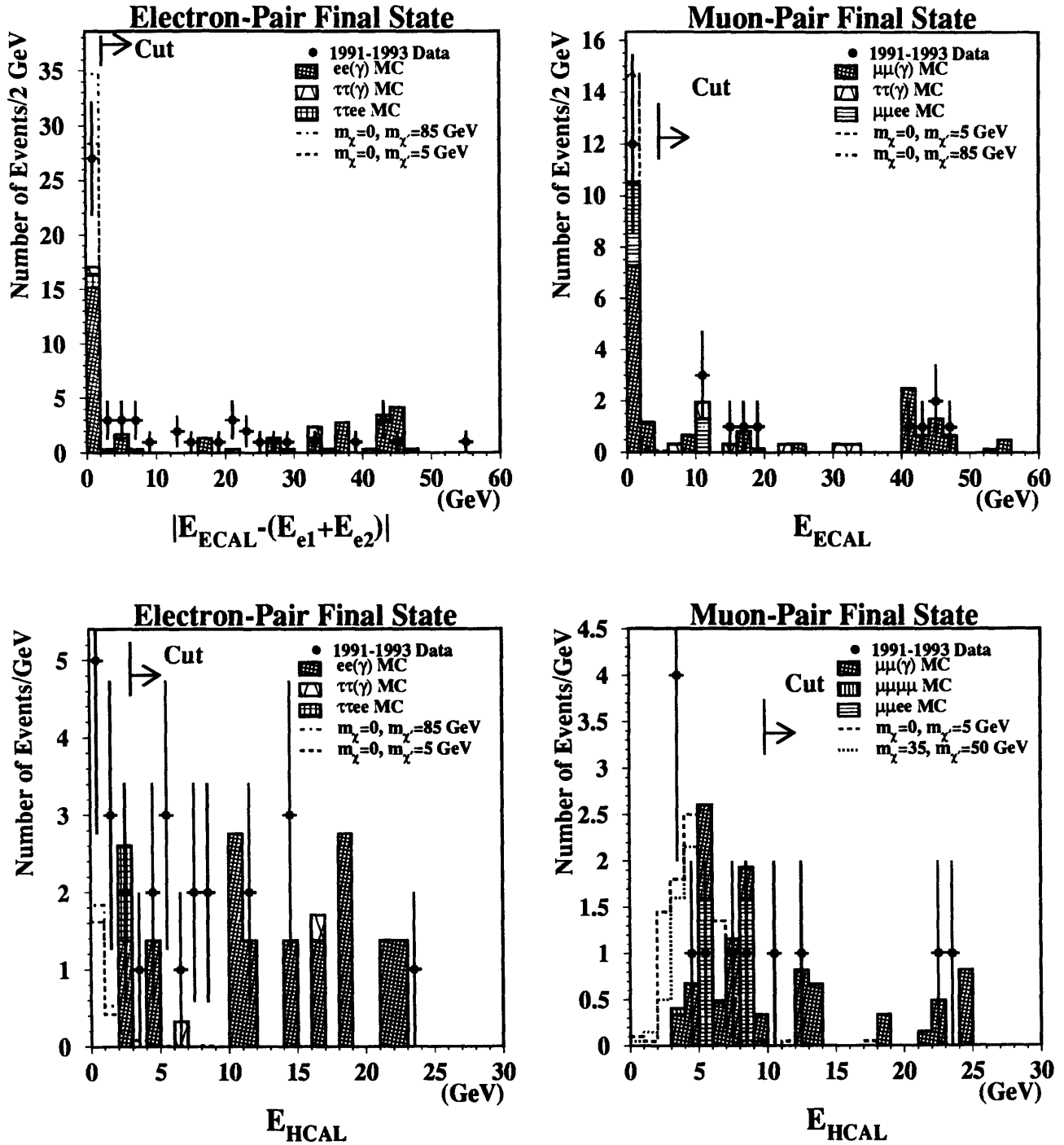
Figure 6-10: *Distributions of (top) electromagnetic and (bottom) hadronic calorimetric energies for (left) electron- and (right) muon-pair final states, for data, Monte-Carlo background processes and Monte-Carlo signal events for selected neutralino mass combinations.*

Table 6.2 shows the number of surviving data events and expected events from the various Standard Model background processes after application of all cuts described above. The agreement with Standard Model predictions is excellent.

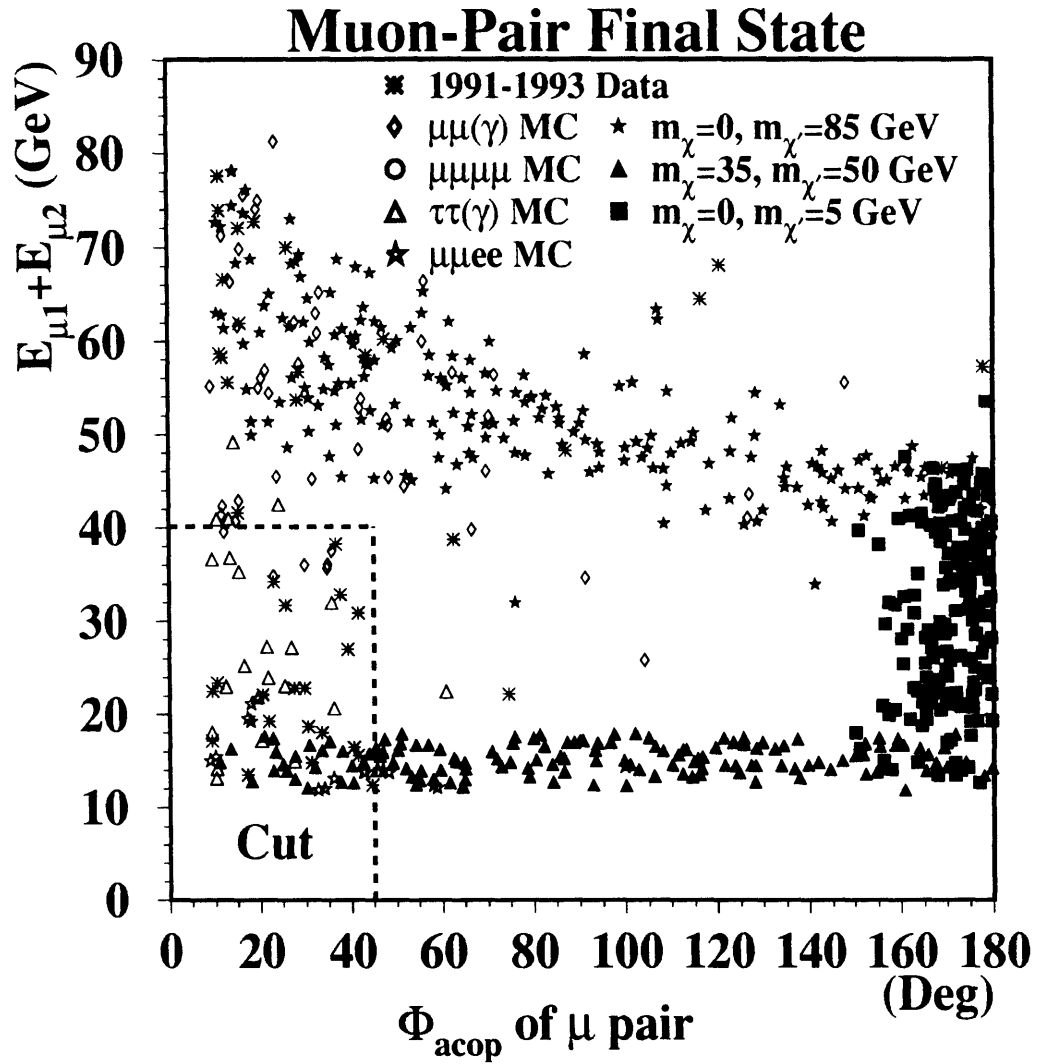| Final State	Data	SM Background Monte Carlo
e^+e^- pair	2	$(1.4 \pm 1.4)(ee\gamma) + (1.2 \pm 1.2)(\tau\tau ee) = 2.6 \pm 1.8$
$\mu^+\mu^-$ pair	4	$(3.2 \pm 1.4)(\mu\mu ee) + (0.7 \pm 0.5)(\mu\mu\gamma) + (0.1 \pm 0.1)(\mu\mu\mu\mu) = 4.0 \pm 1.5$

Table 6.2: *Number of data and expected background events for each leptonic final state channel after all cuts, based on a total integrated luminosity of $67.9\ pb^{-1}$ (~ 1.9 million Z's.)*

Figure 6-11 shows some of the surviving data events as they were recorded in the L3 detector.

6.4 Selection of Hadronic Final State Events

6.4.1 Final State Identification–$q\bar{q}$ Final State

Hadronic (strongly-interacting) particles containing quarks interact with matter via inelastic collisions with detector material nuclei as opposed to the pair-production and bremsstrahlung processes which are at the origin of electromagnetic showers produced by the passage of electrons and photons through matter. The dimension which characterizes both the transverse and longitudinal development of hadronic cascades in a material, the nuclear interaction length λ_I, goes as $A^{1/3}$ and is generally larger than the equivalent dimension for electromagnetic showers, the radiation length X_0, which, for high-Z materials, scales approximately as $\frac{A}{20Z^2}$. Therefore hadrons will cascade in the electromagnetic calorimeter with a broader spatial profile than that of electromagnetically interacting particles (see again Figure 6-1). Furthermore, the cascade will not be contained in the electromagnetic calorimeter, but will continue into the hadronic calorimeter, where most of its energy will be deposited. In this analysis, cascades representing the fragmentation and hadronization of one or more quarks are grouped into jets by the algorithm already described in section 1.1 during the preselection stage. In the hadronic neutralino decay mode $\chi' \longrightarrow \chi + Z^*$, $Z^* \longrightarrow q\bar{q}$, the di-quark final state will consist of one ("monojet" final state) or two ("dijet" final state) such jets depending on:

- The Lorentz boost of the χ', which depends on the difference between m_Z and $m_{\chi'}$. In the case of a large boost, the χ' decay products, including the Z^* and hence the two quarks, will be highly collimated and with high probability will be detected as a monojet.

- The visible energy available to the Z^* system, a function of the difference between m_χ and $m_{\chi'}$. In cases of low visible energy, the lower-energy of the two quarks may either not produce a detectable cascade or will be grouped by the
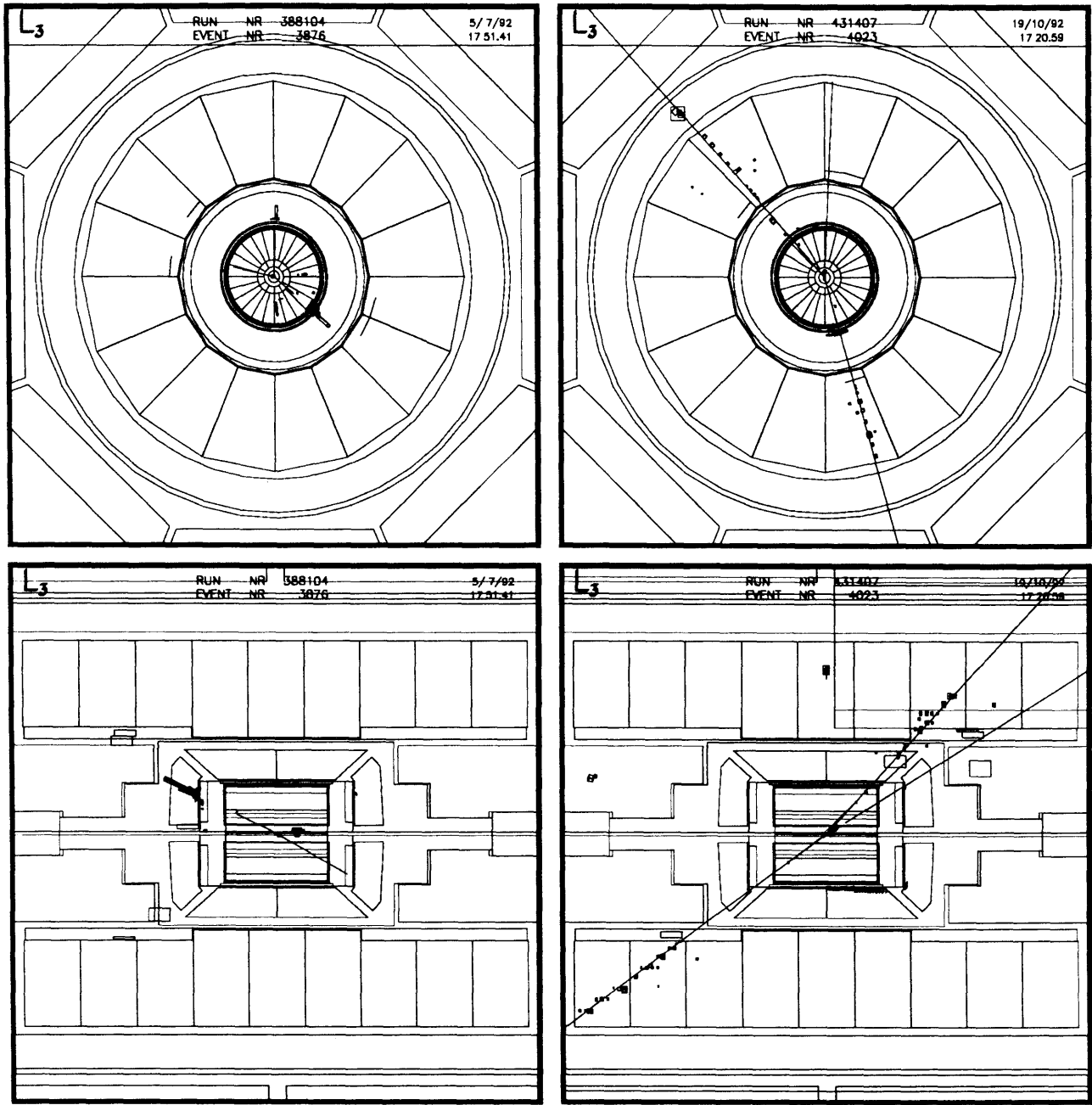
Figure 6-11: *Examples of surviving data events in the (left) electron-pair and (right) muon-pair final state channels. The arrow pointing from the interaction point represents an approximation to the missing energy direction. For the electron-pair event, one of the electrons is pointing out the barrel of the detector, although foreshortening makes it appear as if were pointing down the beam pipe.*

jet algorithm, due to its low relative p_T, into the jet resulting from the other quark, thus again creating a monojet event.

To assure the selection of only hadronic events in the quark-pair final-state category, the following identification criteria were imposed:

- The event contains 1 or 2 jets.

- There are at least 3 good TEC tracks as defined in the prior section on leptonic final-state identification. This requirement vetoes most dilepton events, which should have only two such tracks.

- The invariant mass of each jet should be nonzero. This requirement vetoes jets consisting solely of photons.

The selected events proceed to a final selection, described below.

6.4.2 Final Selection: $Z \to \chi\chi', \chi' \longrightarrow \chi + Z^* \longrightarrow \chi q\bar{q}$

The expected signature of a neutralino decay in the hadronic case largely resembles that for the previously-described leptonic final states: a pair of (possibly acoplanar) hadronic jets recoiling against isolated missing energy and significant missing transverse momentum. To this is added the possibility of single-jet or apparent "monojet" events satisfying similar requirements. The Standard Model processes which constitute background along with the Monte Carlo generators used to study them and, along with the generated signal events, formulate the final selection are detailed below:

- $e^+e^- \longrightarrow q\bar{q}(\gamma)$, i.e. hadronic decays of the Z accompanied by initial/final state radiation. As with the equivalent leptonic processes, the nondetection of the radiation photon(s) may masquerade as fake "missing" energy. To study this process the JETSET [6-1] generator was used.

- $e^+e^- \longrightarrow \tau\tau(\gamma)$ where each τ decays hadronically. As in the leptonic case, the neutrinos present in the τ decays may result in significant "missing" p_T. The KORALZ [6-6] generator was again used to study this process.

- Z, γ (s-channel) or $\gamma\gamma, \gamma Z$ or ZZ (t-channel) $\longrightarrow$ $eeqq$ and $ee\tau\tau$, resulting from the same "four-fermion" processes already described as background to the leptonic final states (see again Figure 6-2), where the two final-state electrons again escape detection. The DIAG36 [6-7] generator was once again used to study this process.

Table 6.3 shows, for each of the above processes, the amount of equivalent luminosity generated, and the eqivalent percentage of the statistics required to equal that for the 1991-1993 data sample used.

As with the leptons, the final selection was optimized to preserve events fitting the signature profiles while vetoing events from the above background processes, by imposing the following requirements:

63

Process	$\int \mathcal{L}\, dt$ Generated $[pb^{-1}]$	% of 1991-1993 Statistics
$q\bar{q}(\gamma)$	49.3	72.6
$\tau\tau(\gamma)$	206.21	303.7
$(ee)qq$	61.45	90.5
$(ee)\tau\tau$	55.27	81.4

Table 6.3: *Background Monte Carlo samples and statistics for hadronic final states.*

- $\not{p}_T > 6$ GeV where $\not{p}_T$ is again the total missing transverse momentum. Figure 6-12 shows the $\not{p}_T$ distributions for hadronic final states (mono- or di-jet) for data, background Monte Carlo events and for two neutralino mass combinations. This cut, analogously to the case of the leptonic final states, is most effective against the 4-fermion processes $Z \to eeqq$ and $ee\tau\tau$, and also somewhat against the radiative process $Z \to q\bar{q}(\gamma)$. In further analogy to the leptonic case, the threshhold cannot be tightened without compromising possible signal detection in the cases where there is little visible energy, as shown. The apparent excess of data events in the range 17 GeV$< \not{p}_T < 25$ GeV is analogous to that observed for the electron-pair final state and has the same probable origin in dead electromagnetic calorimeter crystals. The following distributions of the number of tracks indicate that these events are low-multiplicity (probably $\tau\tau(\gamma)$) events and support the hypothesis of missing electromagnetic energy faking $\not{p}_T$.

- $N_{track} > 3$ for monojets, and
  $N_{track} > 4$ for dijet events, where N_{track} is the number of good TEC tracks as defined previously. The distributions of the number of TEC tracks for mono- and dijet events for data, background Monte Carlo and for two neutralino mass combinations are shown in Figure 6-13. Because of the low multiplicity of decaying τ lepton events this cut removes most of the background due to $Z \to \tau\tau(\gamma)$ and all due to $Z \to ee\tau\tau$. The threshhold for monojets must be set lower than that for dijets because, as can be seen, a highly-boosted χ' system (large difference between m_Z and m'_χ) will replicate the highly-collimated, low-multiplicity behaviour of a τ system. The "excess" of data events described above is largely eliminated by this cut.

- Limits on the number of TEC tracks in the vicinity of the missing energy direction:

  - $N_{track,60} = 0$, where $N_{track,60}$ is the number of good TEC tracks in an $R - \phi$ cone of $60°$ half-angle around the missing energy direction, for monojet events

  - $N_{track,45} \leq 1$, where $N_{track,45}$ is the number of good TEC tracks in an $R - \phi$ cone of $45°$ half-angle around the missing energy direction, for dijet events

  These cuts enforce the isolation of the missing energy direction by targeting charged particles which, by passing through acceptance gaps or temporarily
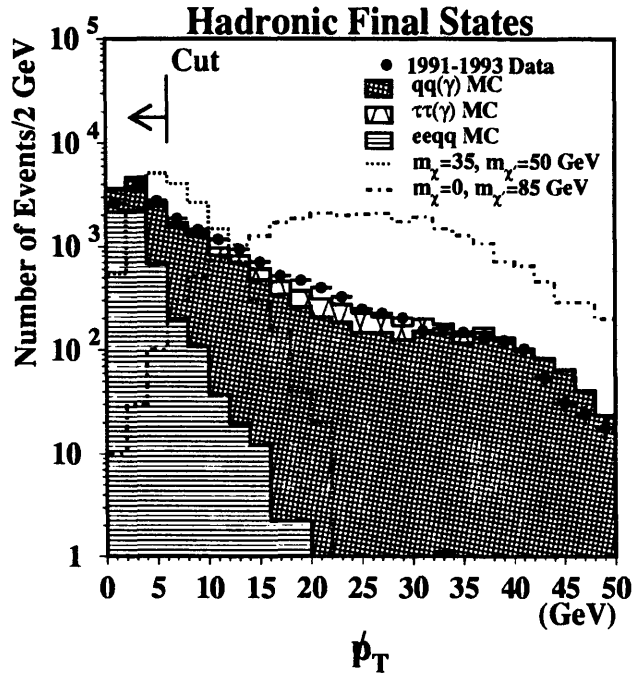
Figure 6-12: *Distribution of missing transverse momentum for hadronic final states, for data, Monte-Carlo background processes and Monte-Carlo signal events for selected neutralino mass combinations.*
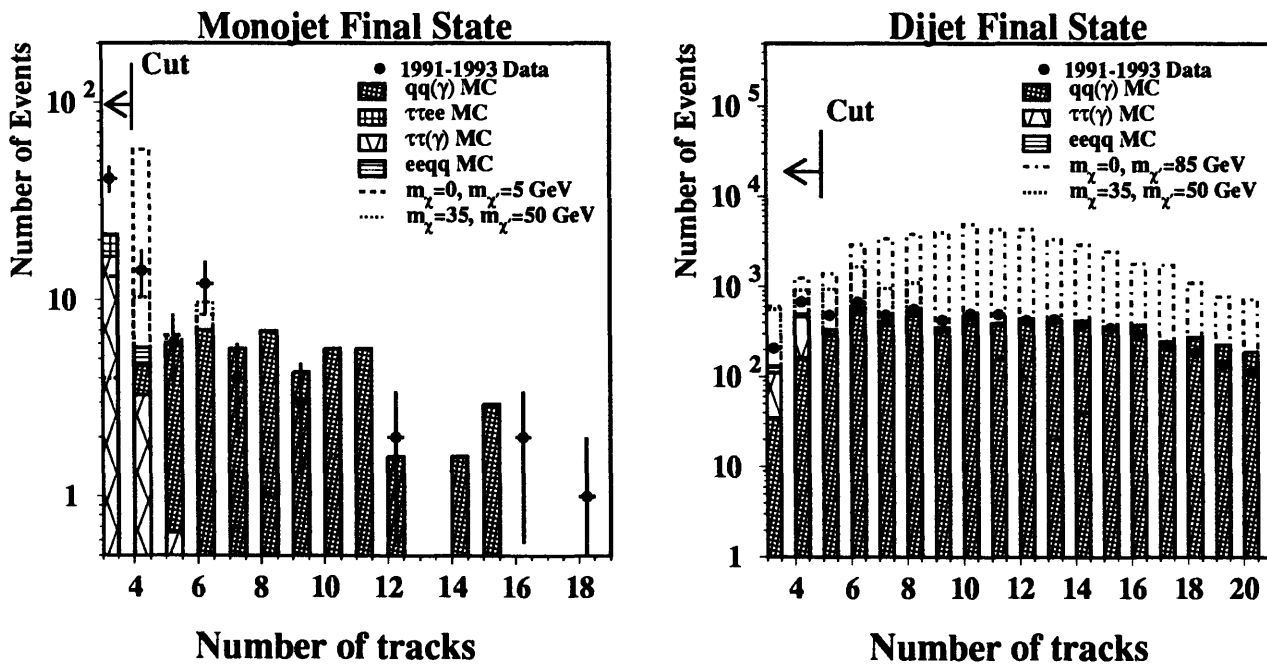
Figure 6-13: *Distribution of the number of TEC tracks for (left) monojet and (right) dijet final states, for data, Monte-Carlo background processes and Monte-Carlo signal events for selected neutralino mass combinations.*

dead calorimetric regions, may masquerade as "missing" energy, while nevertheless leaving a charged track in the TEC. These cuts eliminate most of the remaining background from $Z \to \tau\tau(\gamma)$ and are also effective against $Z \to qq(\gamma)$ background events, as seen from Figure 6-14, which shows the distributions of the two variables.
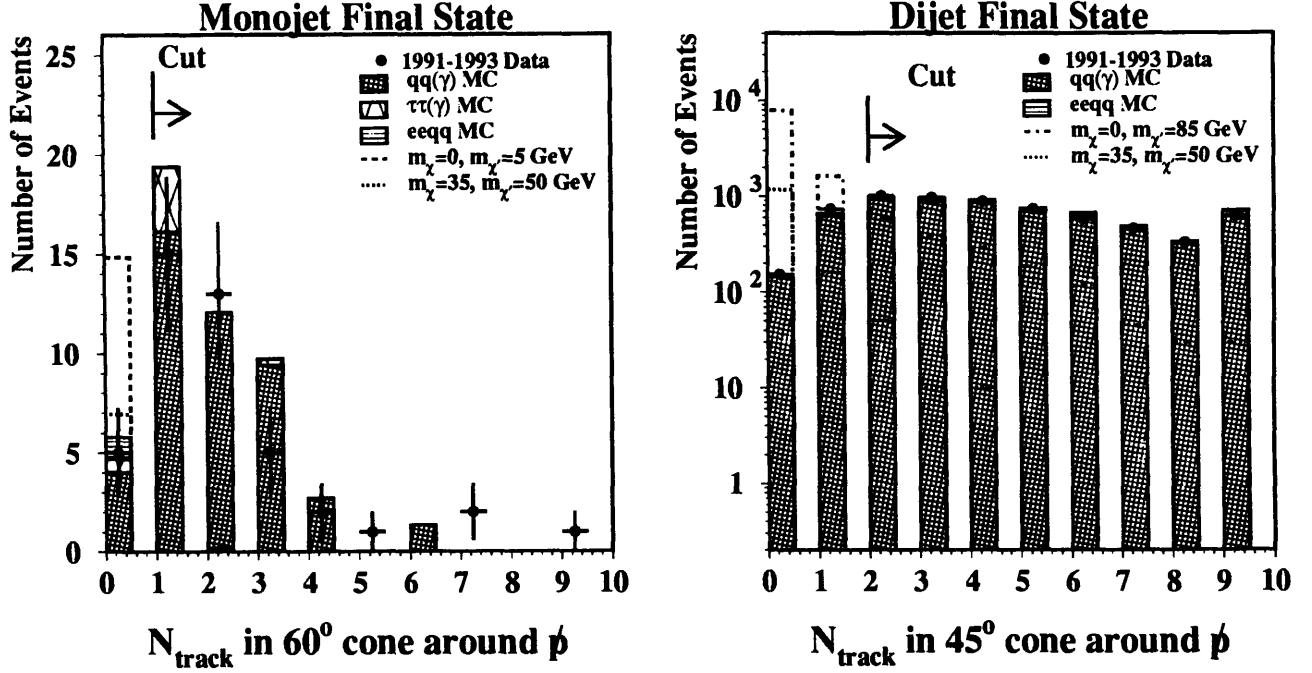
Figure 6-14: *Distribution of the number of TEC tracks in $R - \phi$ cones around the missing energy direction for (left) monojet and (right) dijet final states, for data, Monte-Carlo background processes and Monte-Carlo signal events for selected neutralino mass combinations.*

- $\Phi_{acop} > 40°$ where Φ_{acop} is the acoplanarity angle between the two jets, defined as the supplement of the angle between their projections onto the $R - \phi$ plane transverse to the beam direction, shown for dijet events in Figure 6-15 for data, background Monte Carlo events and for two neutralino mass combinations. For the same reasons as in the leptonic cases, this cut removes virtually all of the remaining background events from the $Z \to \tau\tau(\gamma)$ (due to their characteristic back-to-back topology mentioned previously) and $Z \to eeqq$ processes, and much of the remaining background from $Z \to qq(\gamma)$. In the hadronic case, however, the threshhold must be set higher since some of the cuts used in the leptonic selection (those involving the sum of final-state particle energies) are no longer useful due to the broader energy spectrum observed for hadronic τ decays.

- Limits on calorimetric energy in the vicinity of the missing energy direction: As in the leptonic case, cuts are imposed which target "missing" radiative photons
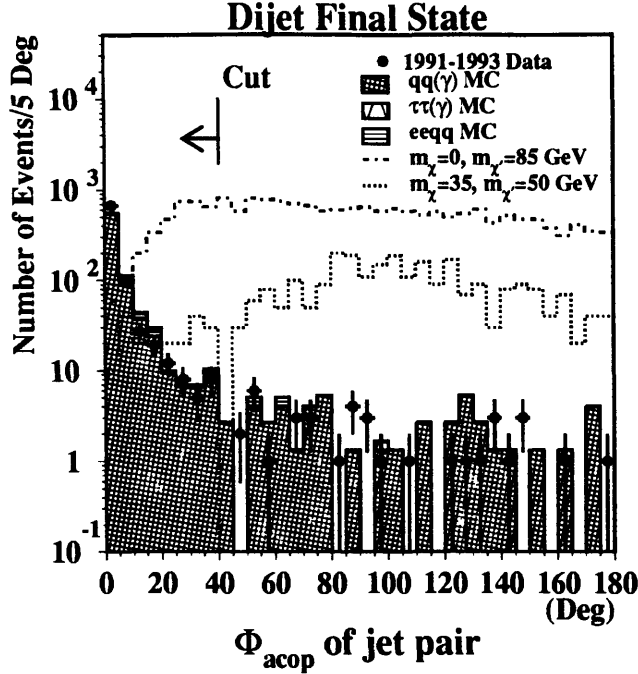
Dijet Final State

Figure 6-15: *Distribution of acoplanarity angle for dijet final states, for data, Monte-Carlo background processes and Monte-Carlo signal events for selected neutralino mass combinations.*

from the remaining background, made up almost totally of $Z \to q\bar{q}(\gamma)$ events. In addition to the same limits in the $30°$ 3-space cone used for the leptonic final states, limits are placed on the calorimetric energy in a $60°$ cone as well for monojets, and for dijets with sufficient acollinearity to assure that the isolation cone includes no jet particles. The following cuts successfully remove virtually all remaining background:

- For both monojet and dijet events:

  * $E_{ECAL,30} \leq 200$ MeV where $E_{ECAL,30}$ is the energy in the electromagnetic calorimeter in a 3-space cone of $30°$ half-angle around the missing energy direction

  * $E_{HCAL,30} \leq 1$ GeV where $E_{HCAL,30}$ is the energy in the hadronic calorimeter in a 3-space cone of $30°$ half-angle around the missing energy direction

- For monojets and dijet events with acolinearity angle (ϕ_{acol}) greater than $20°$:

  * $E_{ECAL,60} \leq 200$ MeV where $E_{ECAL,60}$ is the energy in the electromagnetic calorimeter in a 3-space cone of $60°$ half-angle around the missing energy direction

  * $E_{HCAL,60} \leq 1.5$ GeV where $E_{HCAL,60}$ is the energy in the hadronic calorimeter in a 3-space cone of $60°$ half-angle around the missing energy direction

67

As mentioned previously, these limits were set through the study of beam-gate events which will be discussed in the following section on efficiencies.

• Requirements to eliminate noise events and bad jet reconstructions: From time to time noise from the readout electronics in the HCAL and TEC give rise to "events" characterized by numerous hits all throughout the TEC and at least one HCAL sector in ϕ which may successfully masquerade as mono-or dijet events with "missing" energy. These events, which are not incorporated in the detector simulation used in the reconstruction of signal and background Monte Carlo, distinguish themselves from those involving the passage of true hadronic particles in that there is virtually no signal observed from the ECAL. Although most such events are removed by the above cuts on the number of TEC tracks in the vicinity of the missing energy direction, the following requirements successfully veto the remainder of them:

   – There is at least one electromagnetic cluster with $E \succ 100$ MeV, and the total energy in the electromagnetic calorimeter is at least 200 MeV, for monojet events

   – There are at least three electromagnetic clusters with $E \succ 100$ MeV, for dijet events

Occasionally there are monojet events which are badly reconstructed by the jet algorithm. If the event truly has only one jet, the event thrust direction, $\hat{n}$, (the direction with respect to which each particle's transverse momentum is minimized), defined through

$$T \equiv max \frac{\sum_i |\vec{p_i} \bullet \vec{n}|}{\sum_i |\vec{p_i}|} \tag{6.3}$$

where i indexes the particles in the event, should be the same as or very close to the direction opposite the missing energy direction, and the absolute value of the component of thrust along the missing energy unit direction should be close to 1. The following requirement removes such events:

   – The absolute value of the component of event thrust along the missing energy direction should be at least 0.75

Table 6.4 shows the number of surviving data and expected Standard Model background process events in the hadronic final state channels after application of all cuts described above. As with the leptonic channels the agreement with Standard Model predictions is excellent.

Figure 6-16 shows some surviving data events as they were recorded in the L3 detector.
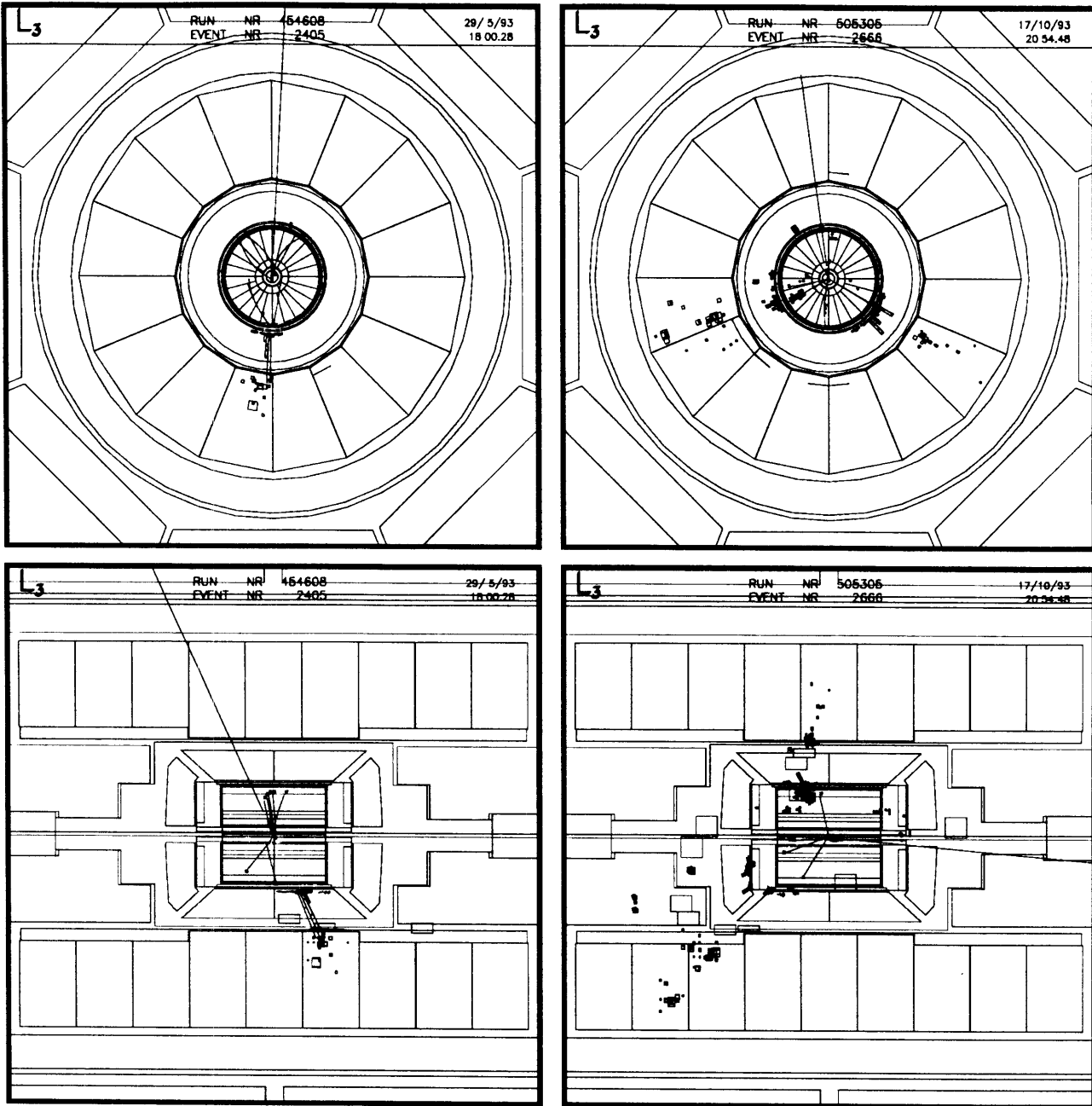
Figure 6-16: *Examples of surviving data events in the (left) monojet and (right) dijet final state channels. The top (R − φ plane) view of the monojet event shows that the tracks apparently opposite to the calorimeter/scintillator activity in the lower (side) view are low-momentum and mostly non-vertex. The arrow pointing from the interaction point represents an approximation to the missing energy direction.*

Final State	Data	SM Background Monte Carlo
Monojet	1	$(1.1 \pm 1.1)(eeqq) + (0.7 \pm 0.5)(\tau\tau(\gamma)) = 1.8 \pm 1.2$
Dijet	2	$(1.1 \pm 1.1)(eeqq)$

Table 6.4: *Number of data and expected background events for each hadronic final state channel after all cuts, based on a total integrated luminosity of $67.9 \, pb^{-1}$ (~1.9 million Z's).*

6.5 Efficiencies

6.5.1 Inefficiency due to Cut on Isolation of Missing Energy Direction

The limits on calorimetric energy in the vicinity of the missing energy direction described in Section 6.3.2 can only be acceptably applied if they are above normal noise pedestals; if not, then there is a danger of vetoing potential signal events. In order to measure these pedestals, a study of the calorimetric energies in various 3-space cones around a random direction (simulating the "missing energy" direction) in beam-gate events was performed. The energy distributions are shown in Figure 6-17, from which the threshholds were chosen so as to retain maximum signal efficiency. These are summarized in Table 6.5, which indicates the likelihood, for any arbitrary (including a possible signal) event, that calorimetric energies observed at or above the threshhold levels in the given cones around the missing energy direction were due to noise alone. This corresponds to the rate at which signal events would be vetoed by these cuts, and the signal and background selection efficiencies must be reduced by applying these percentages.

Energy/Cone around $\vec{p}$	Threshhold (GeV)	% of Beam-Gate Events Above
$E_{ECAL}, 30°$	0.2	0.5
$E_{HCAL}, 30°$	1.0	2.4
$E_{ECAL}, 60°$	0.2	1.3
$E_{HCAL}, 60°$	1.5	2.4

Table 6.5: *Threshholds set for calorimetric energies in various cones around the missing energy direction and percentage of sample of beam-gate events with cone energies above these threshholds.*

6.5.2 Trigger Efficiencies

In addition to the response of the detector, it is important to evaluate the impact of the L3 trigger system (described previously in Chapter 4) on both signal selection efficiencies and estimation of numbers of surviving events from background processes. For the most part the L3 trigger system is not included in the overall detector simulation and event reconstruction software applied to Monte-Carlo-generated events.

Beam-Gate Events
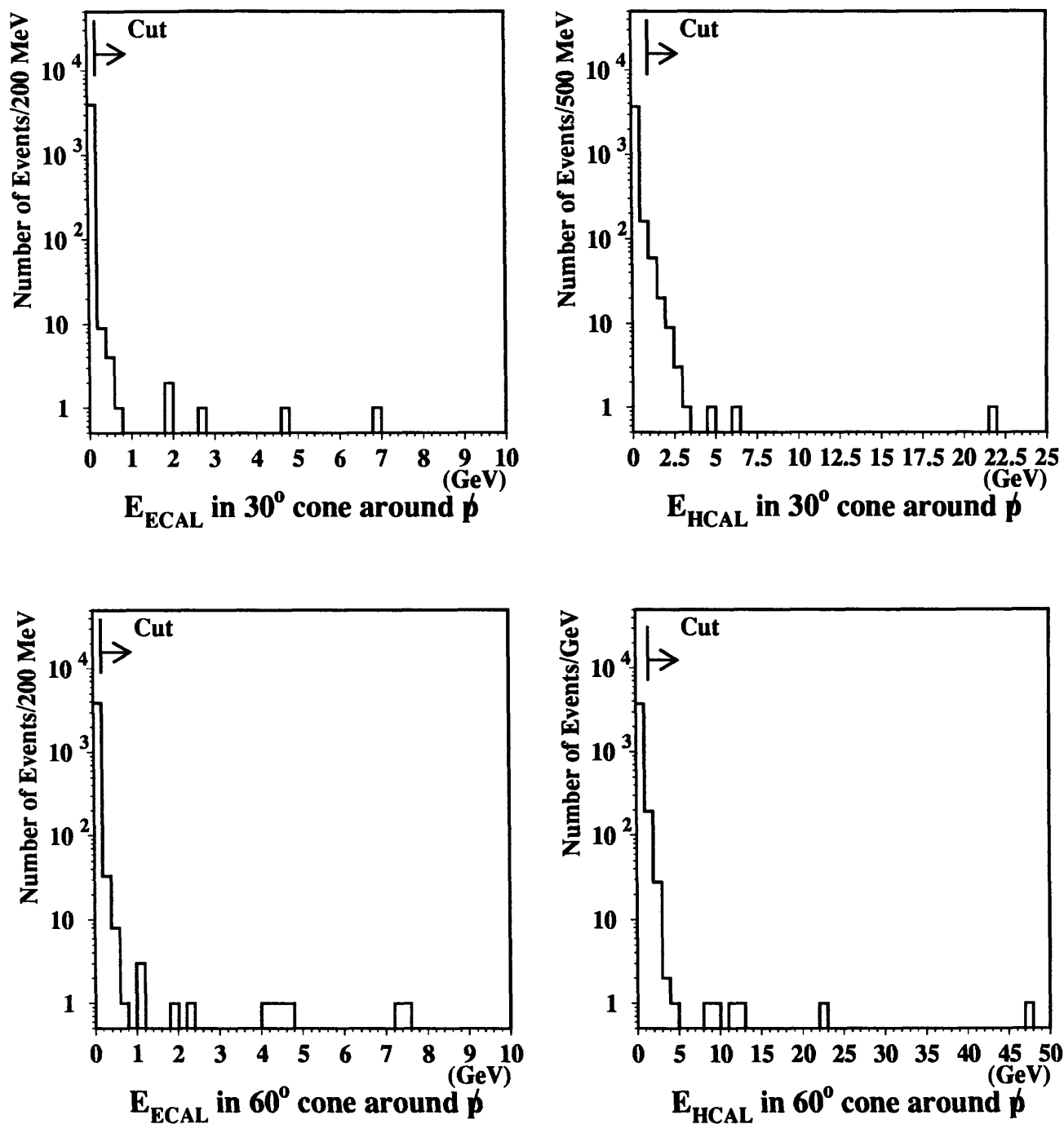
Figure 6-17: *Distributions of (left) electromagnetic and (right) hadronic calorimetric energies within (top) 30° and (bottom) 60° half-angle 3-space cones around a random direction (simulating the missing energy direction), for beam-gate events. The indicated threshholds were chosen from the distributions so as to retain maximum signal efficiency.*

Therefore its effect was estimated by studying the response of similar data events to the triggers, and then applying any needed adjustments to signal efficiencies and background Monte-Carlo event survival rates.

Leptonic Final-State Channels

Electron-pair final-state events are triggered independently by the level-1 energy and TEC triggers. Muon-pair final-state events are triggered independently by the level-1 muon and TEC triggers. In each case, the efficiency of member "A" of the given pair of triggers was estimated by calculating the ratio of the events triggered by both triggers to the number triggered by member "B" alone. The data sample used consisted of events passing the preselection and electron-pair and/or muon-pair final state identification described above in sections 6.1 and 6.3.1, plus the following two physics cuts described in section 6.3.2:

- $\not{p}_T > 4$ GeV. This cut removes most events with forward/backward leptons, for which the TEC itself (whose polar angle coverage is limited to $|\cos\theta| < 0.88$) and hence the TEC trigger starts to show a decrease in efficiency.

- $E_{l_1} + E_{l_2} > 12$ GeV. The energy trigger is less efficient for the low-visible-energy events removed by this cut, due to the presence of fewer overlapping subtriggers.

The efficiency of the energy trigger was found to be 100% for the above-described initial samples, so the $\not{p}_T$ cut, which is largely independent of the energy trigger decision criteria, was dropped and the energy trigger efficiency recalculated based on a larger statistical sample, in order to be able to gain a better idea of the combined trigger efficiencies. Table 6.6 shows the results of the study. The efficiencies of the TEC trigger as measured from both the energy and muon triggers are in excellent agreement with each other. They are lower than for those of the other two triggers due to the non-exclusion from the study sample of data runs where the TEC experienced high voltage or DAQ problems. Since the combined trigger efficiencies are very close to 1 with small error, no adjustment to signal selection efficiencies or background Monte-Carlo rates due to trigger efficiencies was made for the leptonic final-state channels.

Level-1 Trigger	ϵ: Electron-Pair Final State (%)	ϵ: Muon-Pair Final State (%)
Energy	$99.12 \pm 0.34(561/566)$	—
TEC	$88.69 \pm 1.83(298/366)$	$88.42 \pm 3.49(84/95)$
Muon	—	$> 99.99 \pm 0.32(84/84)$
Combined	99.96 ± 0.04	$> 99.99 \pm 0.04$

Table 6.6: *Calculated trigger efficiencies for leptonic final state channels. The statistics used for the study of each channel are shown in parentheses.*

Hadronic Final-State Channels

Hadronic final-state events (both monojet and dijet) are, like the electron-pair events, triggered independently by the level-1 energy and TEC triggers. Their efficiencies in this case were studied using the same methodology as described above for the leptonic final-state channels. The data sample again consisted of events passing the preselection described in Section 6.1 and the $q\bar{q}$ final-state identification described in Section 6.4.1, plus the following physics cut described in section 6.4.2:

- $\not{p}_T > 6$ GeV. In addition to removing many forward/backward mono- and dijet events, this cut removes many with low visible energy, for which the energy trigger is less efficient (see below).

However, unlike the electron case, the energy trigger efficiency is no longer a near-constant, but rather a function of the visible energy in hadronic events. This is because, in the interest of preserving signal selection efficiencies for neutralino mass combinations with very little visible energy (e.g. $m_\chi = 30, m_{\chi'} = 40$ GeV), no explicit cut on the minimum total energy, other than that introduced implicitly by the $\not{p}_T$ cut mentioned above, was made for hadronic final-state events. Hence their visible energy is now allowed to enter a regime below the threshhold of two of the 5 relevant energy subtriggers: the total energy trigger (threshhold at 25 GeV) and the total large angle ($18° < \theta < 162°$) energy trigger (threshhold at 8 GeV for ECAL energy and 15 GeV for ECAL+HCAL energy–see prior description of the energy trigger in Chapter 4). The remaining available subtriggers (cluster, jet and hit) set seperate threshholds on the energy within individual trigger cells and/or require a multiplicity of such cells. These factors combined with the fact that hadronic jets in general are much more diffuse in space than electrons produce a decrease in efficiency of the energy trigger as a function of visible energy starting at about 30 GeV (see Figure 6-18), which must be fitted.

Attempts to fit the energy trigger efficiency are complicated by the statistical dearth of events with $E_{vis} < 12$ GeV and the absolute absence of them with $E_{vis} < 8$ GeV, even after enrichment of the existing data sample with additional events from the τ-pair data stream, not used in the original analysis, but passing the above cuts. Since the two lowest subtrigger threshholds (HCAL cluster trigger with associated TEC track, jet trigger with associated TEC track) are at 2.0 GeV, the additional assumption that the energy trigger efficiency was zero for $E_{vis} < 2$ GeV was made to constrain the fit. Figure 6-18 shows the energy trigger efficiency determined using 14,384 TEC-triggered events, plotted as a function of E_{vis}, fitted to the superimposed function:

$$\epsilon_{Etrig}(E_{vis}) = 1 - \frac{2}{E_{vis}} \tag{6.4}$$

The efficiency of the TEC trigger is also non-uniform for hadronic final-state events. As stated in Chapter 4, this trigger accepts events with at least one pair of tracks each with $|\vec{p}| > 150$ MeV, with acoplanarity angle less than $41°$. It follows that the TEC trigger efficiency should decrease dramatically for hadronic mono- and

73

dijet events having a maximum region in the $R - \phi$ plane devoid of tracks (henceforth referred to as the largest track-deserted region or ATD) larger than $\sim 220°$, and this is what is observed from 14,706 energy-triggered events. Figure 6-18 shows TEC trigger efficiency plotted as a function of the largest track-deserted region, which was fitted to the Fermi-like function (shown superimposed):

$$\epsilon_{TECtrig}(ATD) = \epsilon_0 - \frac{\Delta\epsilon}{1 + Ae^{\frac{ATD_{thr}-ATD}{\Delta ATD}}} \tag{6.5}$$

where

$$\begin{aligned} \epsilon_0 &= 0.98724 \\ \Delta\epsilon &= 0.79 \\ A &= 5.8114 \\ ATD_{thr} &= 210.95 \text{ GeV} \\ \Delta ATD &= 9.6312 \text{ GeV} \end{aligned} \tag{6.6}$$

are the fitted values. The fact that the efficiency is asymptotic to a finite nonzero value is due partially to spurious triggers from noise and partially to the fact that the raw tracks seen by the trigger are not the same as the reconstructed objects used in the calculation of the ATD, and hence are not subject to some of the quality requirements mentioned in section 6.3.1 such as maximum distance of closest approach to the vertex.

6.5.3 Signal Selection Efficiencies

Signal selection efficiencies were estimated throughout the phase space determined by the χ and χ' masses, constrained only by the assumption that the χ is the lightest supersymmetric particle, and by the center-of-mass energy available at LEP I, i.e.:

- $m_\chi < m'_\chi$

- $m_\chi + m'_\chi \leq \sqrt{s}$ for $Z \to \chi\chi'$
  $m'_\chi \leq \frac{\sqrt{s}}{2}$ for $Z \to \chi'\chi'$

Leptonic Final-State Channels

For the electron- and muon-pair final states, signal selection efficiencies for 150 $(m_\chi, m_{\chi'})$ mass combinations throughout the extent of the allowed phase space were determined via a fast Monte Carlo simulation [6-8] which was calibrated with the previously-mentioned full detector signal simulation/event reconstruction and event selection performed for mass combinations at the extrema of the region. The efficiency for an arbitrary point in the allowed phase space was then calculated via interpolation. The fast simulation took the following into account:

- Detector geometry:
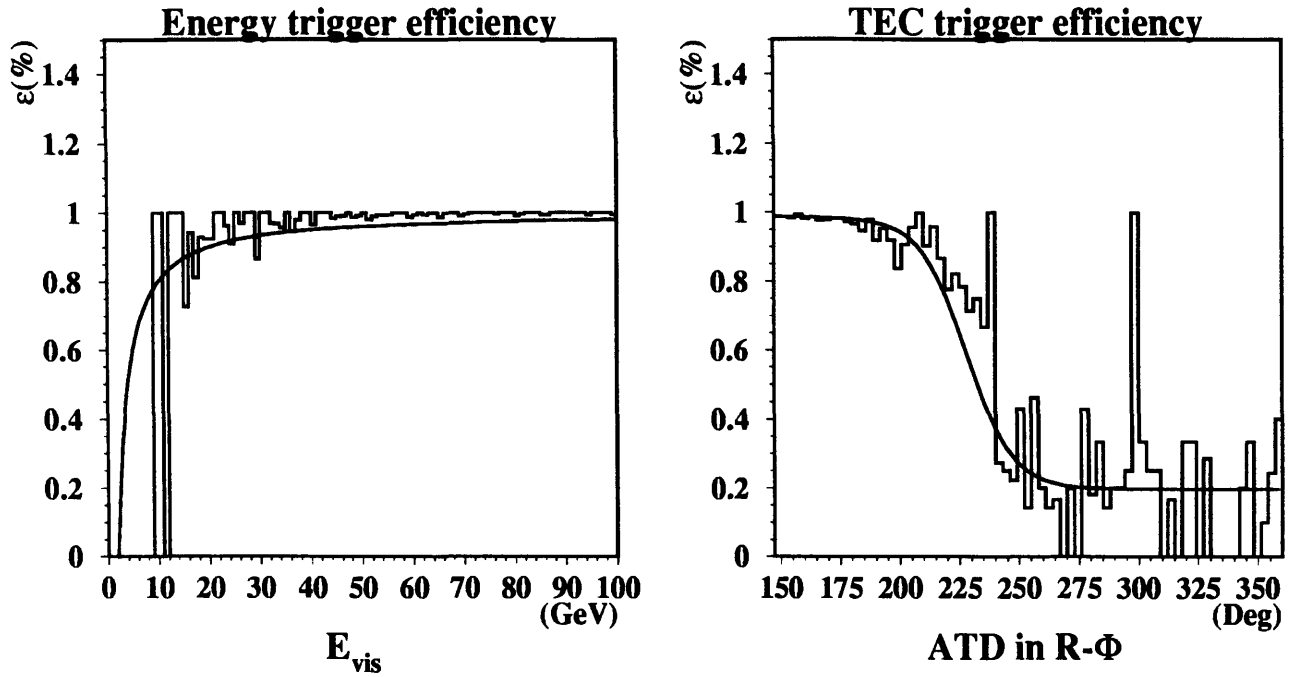
Figure 6-18: *Efficiency of the energy trigger as a function of visible energy, from TEC-triggered hadronic final-state events (left), and efficiency of the TEC trigger as a function of the largest track-deserted region(ATD), from energy-triggered hadronic final state-events (right), with the fitted functions superimposed.*

- For electron-pair final states:

  * Acceptance of the TEC, limited to $|\cos\theta| < 0.88$

  * Inter- and intra-sector TEC acceptance gaps in ϕ of 20mr

  * Acceptance gaps between the BGO barrel and endcaps at $0.7986 \geq |\cos\theta| \geq 0.7431$

- For muon-pair final states:

  * Acceptance of the MUCH, limited to $|\cos\theta| < 0.809$

  * Intra-octant MUCH acceptance gaps in ϕ of 140mr

  * Acceptance gap in θ between the two MUCH half-barrels at $|\cos\theta| < 0.08$

- For muons with $|\vec{p}| < 10$ GeV, probability of detection by the muon chambers [6-9]

- Preselection/Final state identification cuts described in Sections 6.1, and 6.3.1:

  - Requirement that the missing energy vector not point along the beam direction, i.e. $|\cos\theta_{imb}| < 0.9$

  - Minimum energy for electron candidates of 2 GeV

75

- Final selection cuts as described in Section 6.3.2:

  - $\not{p}_T > 4$ GeV

  - $\Phi_{acop} > 10^o$

  - $E_{l_1} + E_{l_2} > 12$ GeV

  - $\Phi_{acop} > 45^o$ OR $E_{l_1} + E_{l_2} > 40$ GeV

- Inefficiencies resulting from cuts on isolation of the missing energy direction as discussed above in Section 6.5.1

The resulting efficiencies for electron and muon-pair final states of the decay $\chi' \to \chi + Z^* \to \chi + l^+l^-$ obtained from the fast simulation are shown in Figure 6-19. Throughout a majority of the allowed mass-combination phase space the efficiency for the electron-pair channel is at least 30%, attaining values in excess of 50%, with an average of near 35% in the populated region; for the muon-pair channel, at least 23%, attaining values in excess of 40%, with an average of near 26%. The relatively lower efficiencies in the muon-pair channel are due to the smaller geometric acceptance of the muon chambers compared to that of the TEC. For 10% of the mass combinations in both leptonic channels the efficiency was 0%, corresponding to situations of insufficient visible energy to be seen in the detector; cases where either $\Delta(m_\chi, m_{\chi'}) < 2$ GeV or extremely low-boost situations $(m_{\chi'} >\sim 0.45 m_Z)$ coupled with low visible energy $(\Delta(m_\chi, m_{\chi'}) < 10$ GeV). Table 6.7 shows a comparison between efficiencies as determined via the fast versus the full simulation. The fast simulation in most cases is more conservative than the full simulation.

		Electron-Pair Final State		Muon-Pair Final State	
m_χ	$m_{\chi'}$	Fast Sim.(%)	Full Sim.(%)	Fast Sim.(%)	Full Sim.(%)
0	5	40.9	41.8	33.5	41.0
0	85	48.8	50.6	37.1	41.4
35	50	33.5	31.4	24.1	26.6

Table 6.7: *Comparison of signal selection efficiencies for electron- and muon-pair final states determined via fast and full simulations. In most cases the fast simulation result is the more conservative.*

Hadronic Final-State Channels

For the mono- and dijet event final states, full detector signal simulation and event reconstruction of the reaction $Z \to \chi\chi', \chi' \longrightarrow \chi + Z^*$, $Z^* \longrightarrow q\bar{q}$ were performed for 33 (m_χ, m'_χ) mass combinations throughout the allowed phase space, and of the reaction $Z \to \chi'\chi', \chi' \longrightarrow \chi + Z^*, Z_1^* \longrightarrow q\bar{q}, Z_2^* \longrightarrow \nu\bar{\nu}$, for 11 mass combinations. Figure 6-20 shows the resulting signal selection efficiencies after application of the preselection, final-state identification and final selections described in previous sections. The efficiency for detecting $Z \to \chi'\chi'$ is about half that for detecting $Z \to \chi\chi'$ for the same mass combination. This is mostly due to the implicit requirement that

Electron-Pair Final State　　　　　　　　　　　**Muon-Pair Final State**
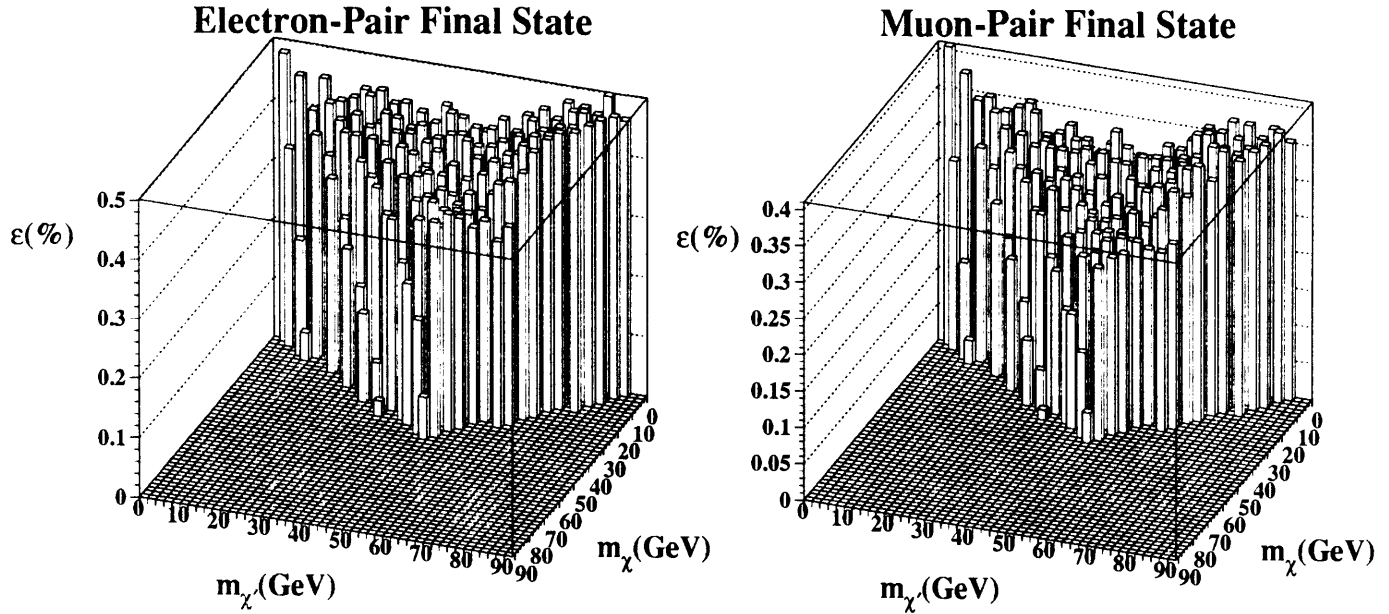
Figure 6-19: *Detection efficiencies for the decay* $\chi' \to \chi + Z^* \to \chi + l^+l^-$ *for electron- and muon-pair final states obtained via the fast simulation, in the allowed region of the* $(m_\chi, m_{\chi'})$ *phase space.*

one or the other of the Z^* decay into a pair of neutrinos, for which the branching ratio is $\sim 20\%$, multiplied by a combinatorial factor of two. The remaining 10% is a contribution from situations where both χ' are highly boosted and both Z^* decay into highly collimated $q\bar{q}$ which are detected as monojets. For $Z \to \chi\chi'$, the detection efficiency is greater than 40% throughout more than half of the allowed phase space, attaining values in excess of 55%, with an aveage of near 33% in the populated region; for $Z \to \chi'\chi'$ the average is 13.5%. As for the leptonic channels, an efficiency of 0% was obtained for about 10% of the mass combinations, in the same kinematic region (low visible energy). The efficiency for an arbitrary point in the allowed phase space is then calculated via interpolation.

6.6　Poisson Upper Limits on the Number of Events from $Z \to \chi\chi'$ or $\chi'\chi'$, $\chi' \longrightarrow \chi + Z^*$, $Z^* \longrightarrow f\bar{f}$

Once the expected number of background events has been corrected for the selection and trigger inefficiencies described above in sections 6.5.1 and 6.5.2 (see Table 6.8), the Poisson upper limit at 95% confidence can be set on the number of signal events N in each final-state channel, shown in Table 6.9. The corrections are very slight and the agreement between data and Standard Model predictions remains excellent. However, because of the size of the errors on the number of expected background Monte Carlo events, the Poisson upper limits were recalculated using a value 1σ

Hadronic Final States: Z→χχ′   **Hadronic Final States: Z→χ′χ′**
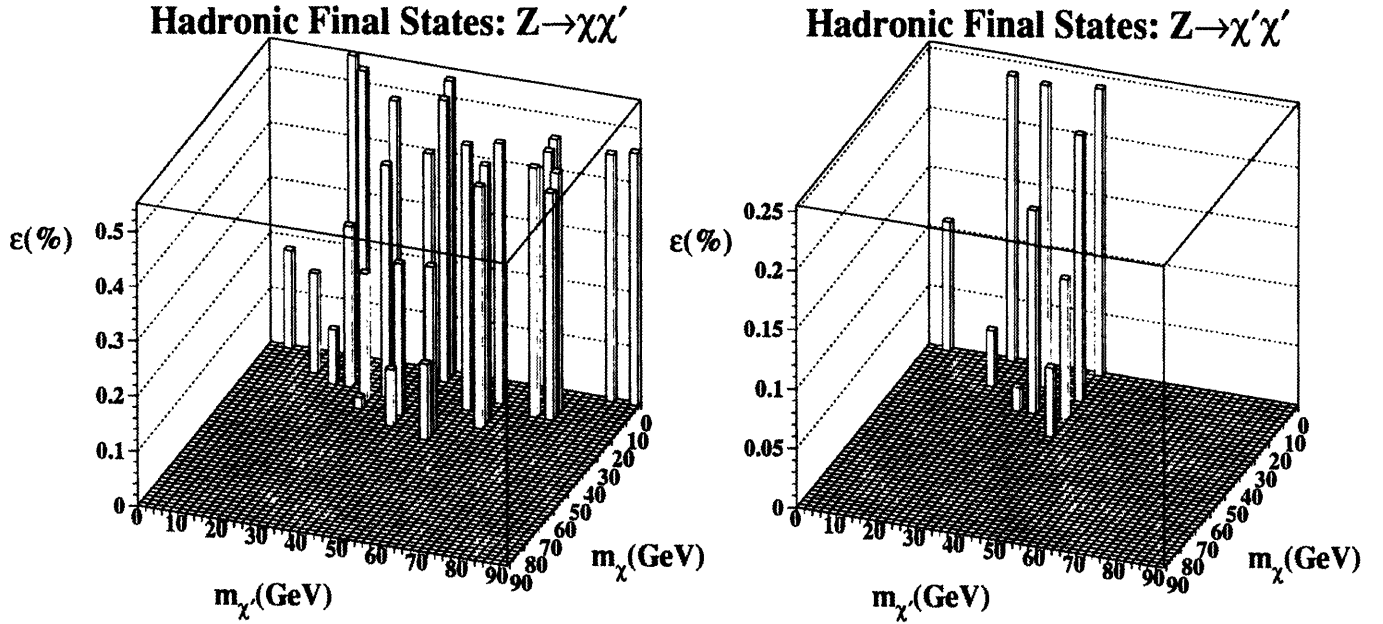
Figure 6-20: *Detection efficiencies for the decays* $Z \to \chi\chi'$, $\chi' \to \chi + Z^* \to \chi + q\bar{q}$ *(left) and* $Z \to \chi'\chi'$, $\chi' \longrightarrow \chi + Z^*$, $Z_1^* \longrightarrow q\bar{q}$, $Z_2^* \longrightarrow \nu\bar{\nu}$ *(right), in the allowed regions of the* $(m_\chi, m_{\chi'})$ *phase space, obtained via full detector simulation and identification via the selection for hadronic final states.*

away from the central value, in order to be able to estimate the effect on the final results. The Poisson upper limits were found to increase in this case by 20.7%, 23.7% and 18.7% respectively for the electron, muon and hadronic final-state channels. The systematic error this introduces into the final results will be discussed in the next chapter.

Final State	Data	SM Background Monte Carlo
e^+e^-	2	$(1.4 \pm 1.4)(ee(\gamma)) + (1.2 \pm 1.2)(\tau\tau ee) = 2.6 \pm 1.8$
$\mu^+\mu^-$	4	$(3.1 \pm 1.3)(\mu\mu ee) + (0.7 \pm 0.5)(\mu\mu(\gamma)) + (0.1 \pm 0.1)(\mu\mu\mu\mu) = 3.9 \pm 1.4$
$q\bar{q}$	3	$(2.0 \pm 1.4)(eeqq) + (0.6 \pm 0.5)(\tau\tau(\gamma)) = 2.7 \pm 1.5$

Table 6.8: *Number of observed data and expected background events for each final state channel after all cuts plus correction for selection and trigger inefficiencies, based on a total integrated luminosity of 67.9 pb^{-1} (~1.9 million Z's.)*

Final State	N at 95% C.L.
e^+e^-	4.60
$\mu^+\mu^-$	5.52
$q\bar{q}$	5.56

Table 6.9: *Poisson upper limit N at 95% confidence on the number of signal events for each leptonic final state channel after all cuts plus correction for selection and trigger inefficiencies.*

Chapter 7

Results

The Poisson upper limit at 95% confidence on the number of Z decays into $\chi\chi'$ and $\chi'\chi'$ pairs, and the signal selection efficiencies for each $f\bar{f}$ channel described in chapter 6 are constrained only by LEP I kinematics and are directly translateable into model-independent limits on the branching ratio of Z into neutralinos throughout the neutralino mass-combination phase space. Then these results can be interpreted within the context of the MSSM, because the neutralino masses are eigenvalues of the four-dimensional MSSM mixing matrix $M^{(0)}$ with parameters M, μ, $\tan\beta$ and $\sin\theta_W$ (recall discussion in Chapter 2). Therefore, any triplet of values $(M, \mu, \tan\beta)$ can be uniquely associated with a mass combination $(m_\chi, m_{\chi'})$, and the number of experimentally predicted neutralino events for a given point in the 3-dimensional MSSM representation obtained from the corresponding point in the two-dimensional mass-combination representation. Through comparison with MSSM-predicted theoretical event rates, area in the MSSM parameter space can be thus excluded, aided by measured constraints on $\Delta\Gamma_Z$, the width available for Z decays from new physics processes, and $\Delta\Gamma_{inv}$, the width available for Z decays from new invisible processes (i.e. in addition to that from $Z \to \nu\bar{\nu}$.)

7.1 Model-Independent Limits on Z Branching Ratios into Neutralinos

For each pair of neutralino masses $(m_\chi, m_{\chi'})$ in the allowed phase space for which the signal selection efficiency is nonzero, a limit at 95% confidence on the branching ratio for $Z \to \chi\chi'$ and $Z \to \chi'\chi'$ for each final state $f\bar{f}$, where $\chi' \to \chi + Z^*$ is calculated as follows:

$$Br(Z \to \chi\chi' \text{ or } \chi'\chi', \chi' \to \chi + Z^*, Z^* \to f\bar{f}) < \frac{N_{f\bar{f}}}{N_Z * \epsilon_{(m_\chi, m_{\chi'})}} \qquad (7.1)$$

where $N_{f\bar{f}}$ is the Poisson upper limit at 95% confidence on the number of Z decays into neutralinos in the $f\bar{f}$ final state channel, N_Z the number of Z decays used in the analysis (1,921,216) [7-1], and $\epsilon_{(m_\chi, m_{\chi'})}$ the signal selection efficiency for the mass-combination $(m_\chi, m_{\chi'})$ in the relevant allowed phase space (for either $Z \to \chi\chi'$ or

$Z \to \chi'\chi')$. The value for an arbitrary point is then calculated via interpolation. The limits on the individual final-state channels are then summed to yield overall limits on $Br(Z \to \chi\chi')$ and $Br(Z \to \chi'\chi')$ where $\chi' \to \chi + Z^*$, shown in Figure 7-1 as equal-value contours in the $(m_\chi, m_{\chi'})$ plane. In both cases the limits are of the order of a few 10^{-5}. For $Z \to \chi\chi'$ they are below 4×10^{-5} throughout approximately $3/4$ of the probed phase space, with a maximum of 5.5×10^{-5} at $(m_\chi = 30 \text{ GeV}, m_{\chi'} = 45$ GeV); for $Z \to \chi'\chi'$ they are inferior to 4×10^{-5} in about half of the allowed area, with a maximum of 5.2×10^{-5} at $(m_\chi = 29 \text{ GeV}, m_{\chi'} = 30 \text{ GeV})$. The maxima correspond predictably to the neutralino mass combinations of lowest signal selection efficiency, close to the kinematic limit where there is little visible energy.

The error on these results introduced by the uncertainty in background Monte Carlo statistics mentioned at the end of the last chapter was estimated as follows: The revised Poisson upper limits for each final-state channel that were calculated assuming that the number of expected background events was 1σ away from the central value were used to recalculate the branching ratio limits for that channel, which were then added to yield a final result. The amount by which this revised branching ratio limit was higher (worse) than the one calculated using the central values was found to be of the order of 18%, which can be considered as a systematic error in the analysis.

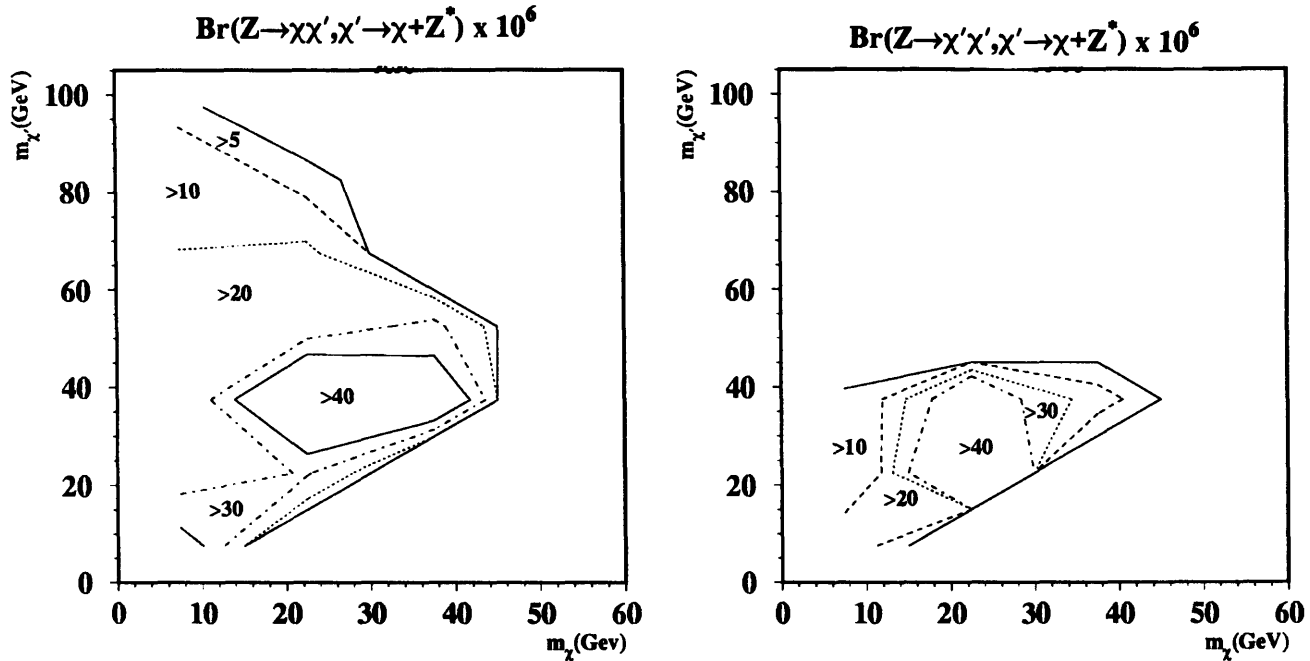
Figure 7-1: *Equal-value contours of the 95% confidence-level limit on (left) $Br(Z \to \chi\chi')$ and (right) $Br(Z \to \chi'\chi')$ for $\chi' \to \chi + Z^*, Z^* \to f\bar{f}$, in the allowed regions of the $(m_\chi, m_{\chi'})$ phase space.*

7.2 Interpretation within the MSSM

The above model-independent results rely on a very few simple assumptions: That a lightest supersymmetric particle (LSP) exists and that it is the lightest neutralino, the χ; that it interacts only weakly with matter and hence is invisible in the L3 detector; that it couples to the other neutralinos and the Z, and that R-parity is conserved so that the χ is stable and single production of SUSY particles is forbidden, but $Z \to \chi\chi'$ and $Z \to \chi'\chi'$ are allowed.The implications of the signal selection efficiencies and the Poisson upper limits on the number of Z decays into neutralinos thus derived in Chapter 6 can now be extended to test a specific theoretical model of supsersymmetry, the Minimal Supersymmetric Standard Model (MSSM). As previously discussed in Chapter 2, this model asumes a global N=1 supersymmetry, spontaneously broken at high energies by a super-Higgs sector containing a Goldstone fermion ("goldstino") and explicitly broken at low ($\sim M_W$) energies at an "effective", unitarity-satisfying scale (obtained by fixing the gravitino mass) by the introduction of explicit ("soft breaking") mass terms in the Lagrangian, containing the universal mass parameters m (for scalars) and M (for gauginos). After low-energy renormalization, in the gaugino-higgsino sector of the model, M becomes a parameter in the charged and neutral mixing matrices which are the coefficients of the charged and neutral gaugino fields in the relevant mass terms, along with μ (the universal higgs-higgsino mass) and $\tan\beta$ (the ratio between the vacuum expectation values v_1 and v_2 of the required two Higgs doublets). Diagonalization of the neutral mixing matrix yields the neutralino masses m_{χ_i} ($i = 1 \ldots 4$) as well as the couplings A_{ij} between them (via $A_{ij} = N_{i3}N_{j3} - N_{i4}N_{j4}$, where N_{ij} is the diagonalizing matrix). Hence the physics of the model is totally specified by the 3 parameters M, μ and $\tan\beta$, and specification of a triplet of their values also specifies a doublet of $(m_\chi, m_{\chi'})$ values in the model-independent phase space. Hence the model-independent results can be used to exclude given triplets of (M,μ,$\tan\beta$) values. Exclusion of a triplet then implies the exclusion of the corresponding pair of neutralino masses, enabling the establishment of mass limits on χ and χ' within the context of the model.

7.2.1 Exclusion by Direct Search

For a given triplet of MSSM parameters (M,μ,$\tan\beta$), the number of theoretically predicted events in the ith decay channel is calculated via:

$$N_{th}(M, \mu, \tan\beta) = \int \mathcal{L} \ dt \times \sigma_i(M, \mu, \tan\beta) \qquad (7.2)$$

where $\int \mathcal{L} \ dt$ is the integrated luminosity used for the study (67.9 pb^{-1}– see previous description of luminosity measurement procedure in Chapter 5), and $\sigma_i(M, \mu, \tan\beta)$ is the product of the neutralino production cross-section and decay branching ratio into the ith channel, calculated according to Equations (2.33) and (2.34) within the STALINO [7-2] generator running in MSSM mode, assuming the following input values:

$$m_{\tilde{f}} = 500 \ \text{GeV} \quad m_Z = 91.181 \ \text{GeV} \quad \Gamma_Z = 2.501 \ \text{GeV}$$

$$m_W = 80.44 \text{ GeV} \qquad m_t = 150 \text{ GeV} \qquad \sin^2 \theta_W = 0.2315 \qquad (7.3)$$

$$m_H = 100 \text{ GeV}$$

Here, $m_{\tilde{f}}$ is the universal sfermion mass, set high enough so as to effectively suppress the contribution of the t-channel diagram (via the exchange of a sfermion) to neutralino production, expected at the Z-pole. The number of experimentally predicted events in the same channel i for the same triplet of values is obtained by dividing the Poisson upper limit at 95% confidence for that channel by the relevant signal selection efficiency for the corresponding $(m_\chi, m_{\chi'})$ mass-combination (both resulting from the model-independent search):

$$N_{exp}(M, \mu, \tan \beta) = \frac{N_i}{\epsilon_i(M, \mu, \tan \beta \leftrightarrow m_\chi, m_{\chi'})} \qquad (7.4)$$

The triplet $(M, \mu, \tan \beta)$ and the corresponding mass combination $(m_\chi, m_{\chi'})$ are then excluded for that channel if $N_{th}(M, \mu, \tan \beta) > N_{exp}(M, \mu, \tan \beta)$. The total area thus excluded in $M - \mu - \tan \beta$ space is then the union of the areas excluded by the individual channels. Figure 7-2 shows this total area excluded at 95% confidence by direct search for $Z \to \chi \chi'$ and that by direct search for $Z \to \chi' \chi'$ in the $M - \mu$ plane, for four values of $\tan \beta$. There is some overlap with the area excluded by constraints on $\Delta \Gamma_Z$ and $\Delta \Gamma_{inv}$ (see discussion and Fig 7-3 in next section). For reference the kinematical constraints ($m_\chi \leq m_Z/2$ for $Z \to \chi\chi$ and $m_\chi + m_{\chi'} \leq m_Z$ for $Z \to \chi \chi'$) delimiting the portion of the parameter space accessible to LEP I, through both invisible and visible channels, are also shown.

7.2.2 Exclusion by Measured Constraints on $\Delta \Gamma_Z$ and $\Delta \Gamma_{inv}$

Area in the $M - \mu - \tan \beta$ MSSM parameter space can also be excluded by limits on $\Delta \Gamma_Z$ and $\Delta \Gamma_{inv}$, the widths available for Z decays from all non-Standard-Model processes and those that involve only invisible final states, respectively. These two quantities can be calculated by comparing recent L3 measurements [7-1, 7-3] of the total and invisible Z widths (Γ_Z^{L3} and $(\frac{\Gamma_{inv}}{\Gamma_l})^{L3}$) with the theoretical values predicted by the Standard Model (Γ_Z^{SM} and $(\frac{\Gamma_{inv}}{\Gamma_l})^{SM}$). At 95% confidence, they are defined by:

$$\frac{\Gamma_Z^{SM} + \Delta \Gamma_Z - \Gamma_Z^{L3}}{\delta \Gamma_Z^{L3}} = 1.64 \qquad (7.5)$$

and

$$\frac{(\frac{\Gamma_{inv}}{\Gamma_l})^{SM} + (\frac{\Delta \Gamma_{inv}}{\Gamma_l}) - (\frac{\Gamma_{inv}}{\Gamma_l})^{L3}}{\delta (\frac{\Gamma_{inv}}{\Gamma_l})^{L3}} = 1.64 \qquad (7.6)$$

where Γ_l is the Z width into leptonic final states. Inserting the follwing values:

$$\Gamma_Z^{L3} = 2494 \pm 10 \text{ MeV} \qquad \Gamma_Z^{SM} = 2473 \text{ MeV}$$

$$\frac{\Gamma_{inv}}{\Gamma_l}^{L3} = 5.95 \pm 0.1 \qquad \frac{\Gamma_{inv}}{\Gamma_l}^{SM} > 5.97 \qquad (7.7)$$

$$\Gamma_l = 83.1 \text{ MeV} \text{ [7-4]}$$

Excluded Regions in the MSSM Parameter Space
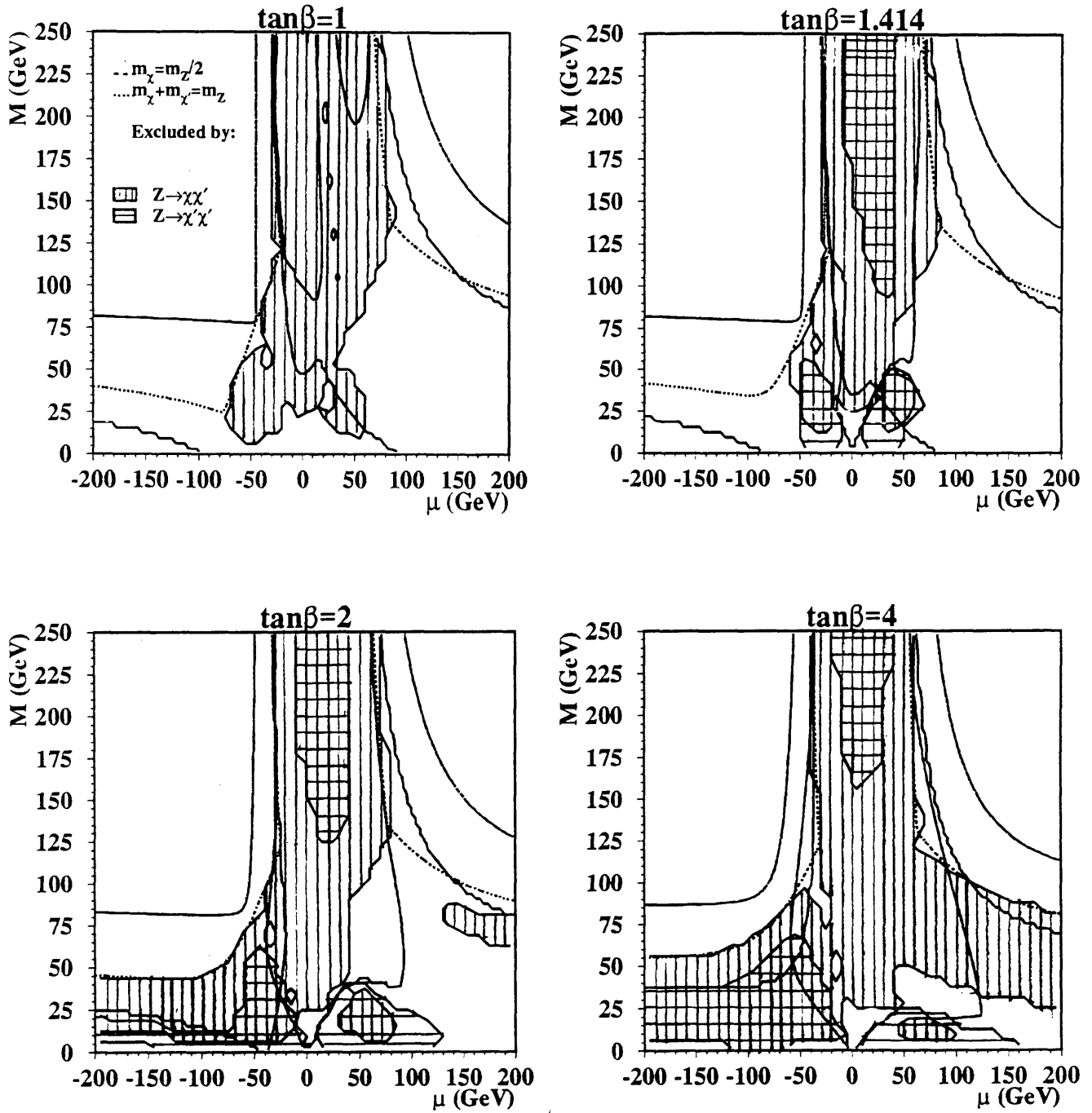

Figure 7-2: *Regions excluded at 95% confidence in the $M - \mu$ plane (hatched) by direct search for $Z \to \chi\chi'$ and $Z \to \chi'\chi'$, for four values of $\tan\beta$, shown against the plotted constraints $m_\chi = m_Z/2$ and $m_\chi + m_{\chi'} = m_Z$, which delineate the portion of the parameter space kinematically accessible to LEP I.*

(where the theoretical computations have assumed $m_t = 100$ GeV, $m_{H^0} = 1$ TeV and $\alpha_s = 0.117$), the following constraints are obtained at the 95% confidence level:

$$\Delta\Gamma_Z < 37.4 \text{ MeV} \quad \Delta\Gamma_{inv} < 15 \text{ MeV} \tag{7.8}$$

With the total width from all Z decays into neutralinos and from those into invisible final states sucn as $\chi\chi$ and $\chi\chi\nu\bar\nu$ calculable once again for any $(M, \mu, \tan\beta)$ triplet via equations (2.32) and (2.34), points in the MSSM parameter space and their counterparts in the $(m_\chi, m_{\chi'})$ phase space can be excluded if either $\Gamma_{Z\to\chi\chi',\chi'\to\chi f\bar f}$ $(M, \mu, \tan\beta) > 37.5$ MeV or $\Gamma_{[Z\to\text{neutralinos (invisible)}]} > 15$ MeV. The area excluded by these constraints is shown in Figure 7-3, superposed on that excluded by the direct search, along with the area not yet excluded. It can be seen that the majority of the exclusion is indeed performed by these constraints, but for values of $\tan\beta$ below 4, the direct search excludes significant and different portions of the parameter space. Starting from $\tan\beta = 2$, most of the space accessible to LEP I through visible channels is excluded; at $\tan\beta = 4$ the exclusion of the LEP I-accessible space is virtually complete.

By considering the union of the sets of neutralino mass combinations excluded by both the direct search and the constraints on $\Delta\Gamma_Z$ and $\Delta\Gamma_{inv}$, lower limits at 95% confidence on m_χ and $m_{\chi'}$ can be set within the context of the MSSM. Figure 7-4 shows, for four values of $\tan\beta$, the region of the $(m_\chi - m_{\chi'})$ mass plane probed and the subset of that region excluded by combining the direct search with the constraints on $\Delta\Gamma_Z$ and $\Delta\Gamma_{inv}$. Obviously for $\tan\beta < \sqrt{2}$ no lower limit can be set; for $\tan\beta = \sqrt{2}$ there are still windows for light neutralino pairs; say for $(m_\chi = 3, m_{\chi'} = 13$ GeV). For $\tan\beta \geq 2$ lower limits can be set by considering the minimum values of m_χ and $m_{\chi'}$ along the border between the excluded and non-excluded areas. These are shown in table 7.1 along with the corresponding mass combination points.

$\tan\beta$	$m_\chi >$ [GeV]	$m_{\chi'} >$ [GeV]
2	20 (20, 81)	47 (41, 47)
4	25 (25, 78)	53 (38, 53)
8	26 (26, 81)	54 (36, 54)

Table 7.1: *Lower limits at 95% confidence on the masses of the two lightest neutralinos, for various values of* $\tan\beta$, *as a consequence of the direct search combined with constraints on* $\Delta\Gamma_Z$ *and* $\Delta\Gamma_{inv}$. *The mass point associated with the limiting value is shown in parentheses.*

The limits on m_χ correspond to mass combinations for which the production center-of-mass energy is well beyond the reach of LEP I (101 GeV); therefore further improvement must wait for LEP 200. For the $m_{\chi'}$ values, the associated mass combinations lie at or near the kinematic limit; so an improvement up to this limit (1 or 2 GeV) could be possible with greater statistics.

Excluded Regions in the MSSM Parameter Space
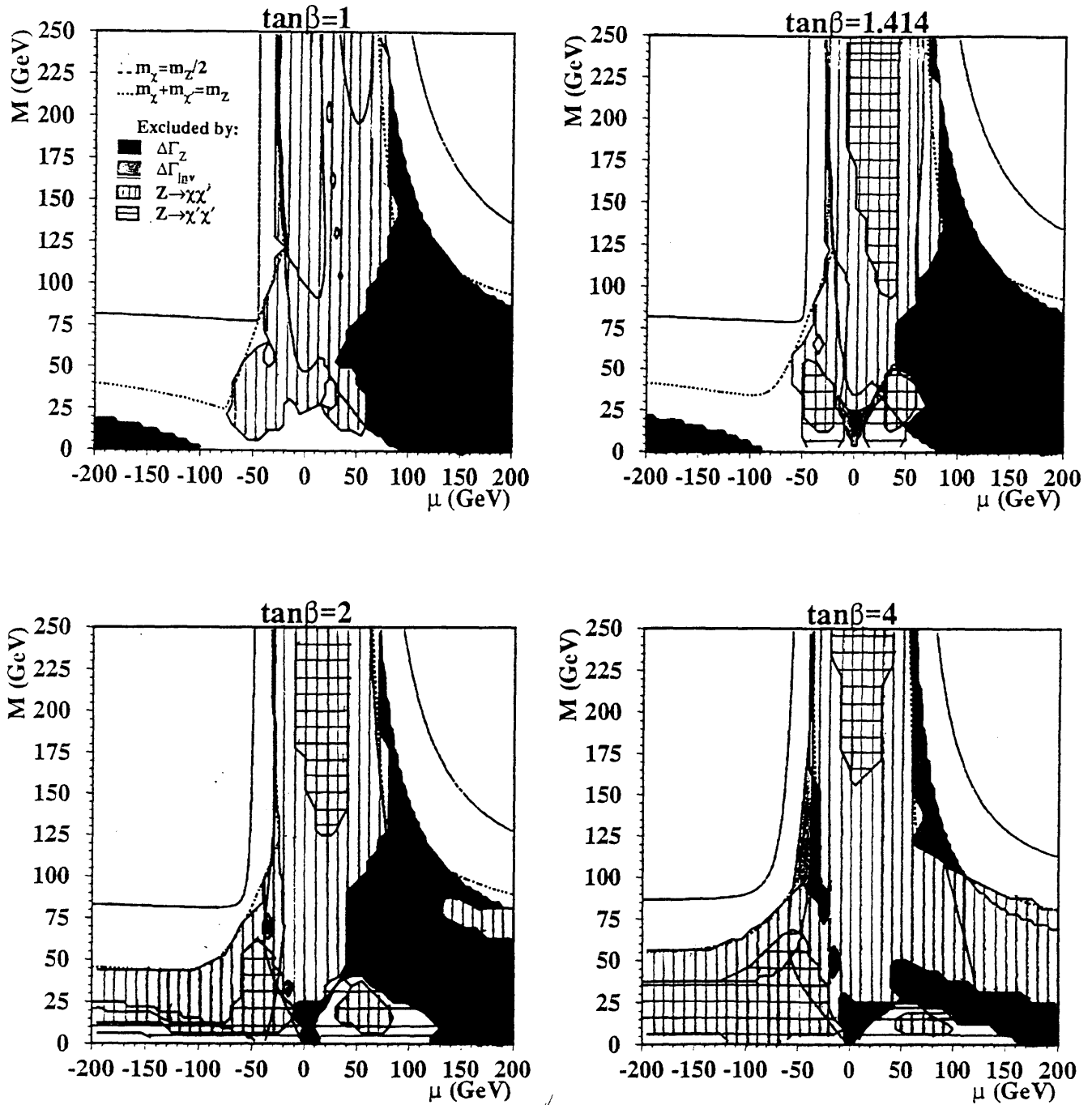
Figure 7-3: *Regions excluded at 95% confidence in the $M - \mu$ plane (shaded) by $\Delta\Gamma_Z < 37.4$ MeV and $\Delta\Gamma_{inv} < 15$ MeV, for four values of $\tan\beta$, shown against the plotted constraints $m_\chi = m_Z/2$ and $m_\chi + m_{\chi'} = m_Z$, which delineate the portion of the parameter space kinematically accessible to LEP I. The hatched area is the region excluded by direct search. Shown in white is the area not yet excluded.*
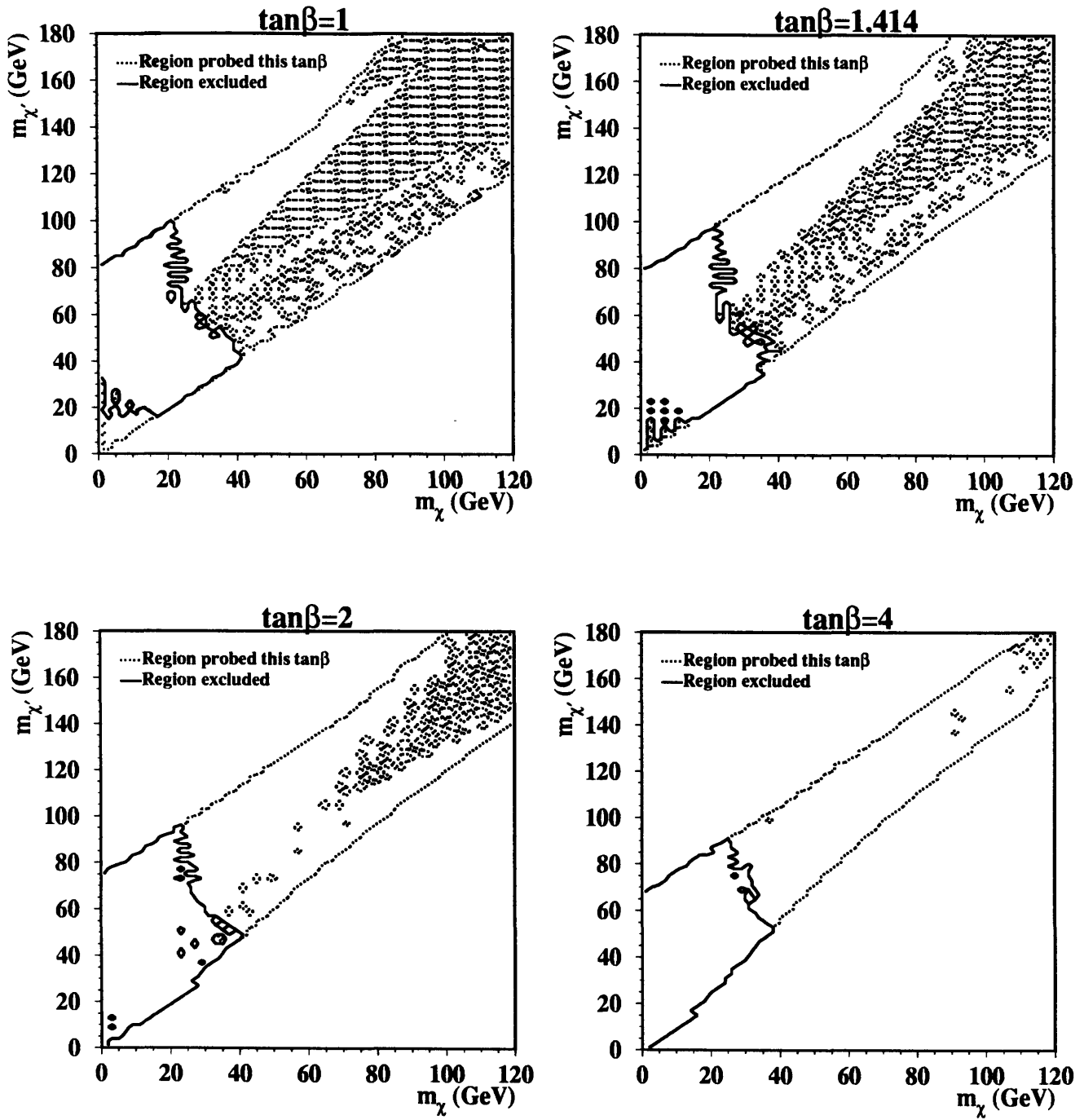
Figure 7-4: *Probed and excluded regions in the* $(m_\chi - m_{\chi'})$ *mass plane, for four values of* $\tan\beta$, *obtained by combining direct search with constraints on* $\Delta\Gamma_Z$ *and* $\Delta\Gamma_{inv}$. *For* $\tan\beta \geq 2$, *lower limits on* m_χ *and* $m_{\chi'}$ *can be set at 95% confidence.*

Chapter 8

Conclusion

Using data recorded by the L3 detector at LEP during 1991, 1992 and 1993, corresponding to 67.9 pb^{-1} of integrated luminosity, a search for supersymmetric particles, in particular the two lightest neutralinos, χ and χ', via the reactions $e^+e^- \longrightarrow Z \rightarrow \chi\chi'$ and $e^+e^- \longrightarrow Z \rightarrow \chi'\chi'$ has been performed. The assumption is made that the χ' decays into a stable and only weakly-interacting (hence invisible) χ plus a fermion pair via $\chi' \longrightarrow \chi + Z^*$, $Z^* \longrightarrow f\bar{f}$. Therefore the signature searched for is an electron, muon or hadronic jet pair or monojet recoiling against isolated missing energy and significant missing transverse momentum. After applying a selection guided by this signature, no significant excess over predicted event rates from Standard Model-predicted background processes was found, and a Poisson upper limit at 95% confidence was set on the number of events from Z decays into neutralinos for each final-state channel, shown below (Table 8.1):

Final State	N at 95% C.L.
e^+e^-	4.60
$\mu^+\mu^-$	5.52
$q\bar{q}$	5.56

Table 8.1: *Poisson upper limit N at 95% confidence on the number of signal events for each leptonic final state channel after all cuts plus correction for selection and trigger inefficiencies*

Combining these upper limits with signal selection efficiencies over the kinematic region accessible to LEP I, which averaged $\sim$ 35% for the electron-pair, $\sim$ 26% for muon-pair final states, $\sim$ 33% for hadronic final states (mono- and di-jet) from $Z \rightarrow \chi\chi'$ and $\sim$ 13.5% for those from $Z \rightarrow \chi'\chi'$, model-independent limits at 95% confidence on Z branching ratios into neutralinos of a few 10^{-5} could be set, with the following maxima:

$$Br(Z \rightarrow \chi\chi') < 5.5 \times 10^{-5} \qquad (8.1)$$
$$Br(Z \rightarrow \chi'\chi') < 5.2 \times 10^{-5}$$

These are comparable or compare favorably with equivalent results from the other LEP experiments, shown in Table 8.2:

	This Analysis	ALEPH [8-1]	DELPHI [8-2]	OPAL [8-3]
$Br(Z \to \chi\chi')$	$< 5.5 \times 10^{-5}$	Few 10^{-5}	$< 5 \times 10^{-4}$	$< 5 \times 10^{-4}$
$Br(Z \to \chi'\chi')$	$< 5.2 \times 10^{-5}$	Few 10^{-5}	$< 5 \times 10^{-4}$	$----$
Data Years	$1991 - 1993$	$1989 - 1990$	$1990 - 1991$	$1989 - 1990$
$\int \mathcal{L}$ dt $[pb^{-1}]$	67.9	8.5	Not stated	2.1
N_Z	1.9×10^6	2×10^5	3.3×10^5	Not stated

Table 8.2: *Upper limits at 95% confidence on $Br(Z \to \chi\chi')$ and $Br(Z \to \chi'\chi')$ from this analysis and the other LEP experiments, along with statistics on the data used in each case.*

The model-independent results in this study were then interpreted in the context of the currently most widely-accepted specific model of supersymmetry, the MSSM (Minimal Supersymmetric Standard Model). By exploiting the fact that a given triplet of MSSM parameters $(M, \mu, \tan\beta)$ maps to an unique pair of neutralino masses $(m_\chi, m_{\chi'})$, the number of experimentally-predicted events for each such triplet was computed and compared to the theoretically-predicted number, and the theory excluded for those points where the theoretical prediction exceeded the experimental. The theory was also excluded for parameter-space points where the calculated theoretically-predicted width from either all Z decays into neutralinos or those into only invisible final states was larger than the current L3 limits on $\Delta\Gamma_Z$ (37.5 GeV) or $\Delta\Gamma_{inv}$ (15 GeV), respectively. For values of $\tan\beta$ greater than or equal to 2 the latter was the more powerful method of exclusion, although for small $\tan\beta$ values the direct search excluded a significant and different portion of the parameter space. In total, within the kinematical region accessible to LEP I through visible neutralino-decay channels, starting with $\tan\beta = 2$ most of the MSSM parameter space was excluded; for $\tan\beta \geq 4$ the exclusion of the MSSM at LEP I energies can be considered total. (These results are compatible with those reported by the other LEP experiments [8-1, 8-2, 8-3].) This led to the establishment of lower limits at 95% confidence for $\tan\beta \geq 2$ on the neutralino masses m_χ and $m_{\chi'}$. These are shown in Table 8.3, along with the results reported by the ALEPH collaboration [8-1] [1] (the only other one of the LEP experiments to have published neutralino mass limits):

During the 1994 data-taking period which has just ended, the L3 detector has collected another ~ 50 pb^{-1} of integrated luminosity, and, with the advent of bunch trains [8-4] in the LEP accelerator permitting higher currents, an additional ~ 100 pb^{-1} is expected for 1995, the last year of LEP I. With approximately triple the number of Z decays used in this study, a decrease in the model-independent branching ratio limits to approximately one-third of the values reported in this study can be expected, along with some slight improvement in exclusion in the MSSM parameter space for small ($\tan\beta < 2$) values of $\tan\beta$, and a corresponding increase ($\sim 1 - 2$ GeV) in the χ' mass limit.

---

[1]The ALEPH values were taken from a plot in the article and are therefore approximate.

tan β	$m_\chi >$ [GeV]		$m_{\chi'} >$ [GeV]	
	This Analysis	ALEPH	This Analysis	ALEPH
2	20	13.5	47	40
4	25	22	53	45
8	26	26	54	45

Table 8.3: *Lower limits at 95% confidence on the masses of the two lightest neutralinos, for various values of* tan β, *from this analysis and from the ALEPH collaboration.*

In 1996 LEP will move into its second phase (LEP 200), with center-of-mass energies approaching 200 GeV. This will increase by approximately a factor of 5 the mass-combination phase space available to be probed for the existence of supersymmetric particles. However it is likely that at first the focus will be not on neutralinos, but rather on the search for the charginos $\chi^\pm$ (the linear combinations of the winos and charged higgsinos). This is because at LEP 200 energies the MSSM-predicted production cross-sections for charginos are approximately two orders of magnitude greater than for neutralinos, for the same MSSM parameter-space triplets [8-5]. Pair-produced charginos would each decay into a W^* and an invisible neutralino, resulting in signatures whose final states resemble those of W pairs, except for missing energy and mass, and of course reconstructed invariant mass. For this reason W pairs constitute the most redoubtable source of irreducible background to chargino production and decay. Nevertheless, preliminary studies by Grivaz [8-6] and others have estimated that, assuming a total LEP 200 integrated luminosity of $500pb^{-1}$, a discovery-level sensitivity $(S/\sqrt{B} \geq 5\sigma)$ could be attained for chargino-pair production cross-sections in excessof 170fb. Once again making use of the mapping between the MSSM parameter space and the gaugino-mass space, this means that the entire mass range up to the LEP 200 kinematic limit could be explored for chargino cross-sections of this order of magnitude. However from a model-independent standpoint there is no *a priori* reason why the search for neutralinos, whose signature remains simpler, should not proceed concurrently. LEP 200 may well reveal SUSY as the solution to the Standard Model's renormalizeability problems.

Bibliography

[1-1] S.L. Glashow, Nucl. Phys. **22** (1961) 579;
S.L. Glashow, J. Ilipoulos and L. Maiani, Phys. Rev. **D 2** (1970) 1285;
S. Weinberg, Phys. Rev. Lett. **19** (1967) 1264;
A. Salam and J.C. Ward, Phys. Lett. **13** (1964) 168;
A. Salam, "Elementary Particle Theory", edited by N. Svartholm (Almquist and Wiksell, Stockholm, 1968) 367.

[1-2] UA1 Collaboration, G. Arnison *et al.*, Phys. Lett. **B 122** (1983) 103; Phys. Lett. **B 126** (1983) 398;
UA2 Collaboration, P. Bagnaia *et al.*, Phys. Lett. **B 129** (1983) 130;
UA2 Collaboration, R. Ansari *et al.*, Phys. Lett. **B 186** (1987) 440.

[1-3] CDF Collaboration, F. Abe *et al.*, Fermilab-Pub-94/097-E

[1-4] P.W. Higgs, Phys. Lett. **12** (1964) 132; Phys. Rev. Lett. **13** (1964) 508; Phys. Rev. **145** (1966) 1156;
F. Englert and R. Brout, Phys. Rev. Lett. **13** (1964) 321.

[1-5] Barger and Phillips,Collider Physics, Addison-Wesley, 1987, pp. 514-515;
E. Gildner, Phys. Rev. **D 14** (1986) 1667.

[1-6] M. Peskin, Proc. Int. Symposium on Lepton and Photon Interactions at High Energies, Bonn, 1981, ed. W. Pfeil (Univ. Bonn, 1981), 180.

[1-7] R. Kaul, Rev. Mod Phys. **55** (1981) 449;
E. Farhi and L. Susskind, Phys. Rep. **74** (1981) 277.

[1-8] Y. Gol'fand and E. Rikhtman, JETP Lett. **13** (1970);
D. Volkov and V. Akulov, JETP Lett. **16** (1972) 438;
J. Wess and B. Zumino, Nucl. Phys. **B70** (1974) 39.

[1-9] M. Chen, C. Dionisi, M. Martinez and X. Tata, Physics Reports **159** (1988), 201.

[1-10] S. Wolfram, Phys. Lett **82B** (1979) 65;
C. B. Dover, T. K. Gaisser and G. Steigman, Phys. Rev. Lett. **42** (1979) 1117;
P. F. Smith and J.R.J. Bennett, Nucl Phys. **B149** (1979) 525;
P.F. Smith *et. al.*, Nucl. Phys. **B206** (1982) 333; E. Norman, S. Gazes and D. Bennett, Phys. Rev. Lett. **58** (1987) 1403.

[1-11] Particle Data Group, M. Aguilar-Benitez *et al.,* "Review of Particle Proper-
        ties", Phys. Rev. **D50** (1994) 1799ff.

[1-12] DELPHI Collaboration, P. Abreu *et. al.,* International Conference on High
        Energy Physics, Dallas, Texas, USA, August 5-12 1992.

[2-1]   Chew, S-Matrices, Benjamin Press.

[2-2]   See Reference [1-9]

[2-3]   Barger and Phillips,Collider Physics, Addison-Wesley, 1987, pp. 514-515.

[2-4]   Barger and Phillips,Collider Physics, Addison-Wesley, 1987, pp. 516-517

[2-5]   R. Barbieri,Il Nuovo Cimento **2** (1988) 16

[2-6]   See Reference [1-4].

[2-7]   P.J. Franzini and P Taxil, *et al.,* "Z Physics at LEP 1", edited by G. Altarelli
        et al., CERN 89-08, Vol. 3, (1989) 93.

[2-8]   F. Zwirner, talk at Workshop "Ten Years of SUSY Confronting Experiment"
        , CERN, Geneva, Switzerland, Sept 1992.

[2-9]   R. Barbieri, Il Nuovo Cimento **2** (1988) 17.

[2-10] P.J. Franzini and P Taxil, *et al.,* "Z Physics at LEP 1", edited by G. Altarelli
        et al., CERN 89-08, Vol. 3, (1989) 92.

[2-11] J. Ellis *et al.,* Phys. Lett. **132B** (1983) 436.

[2-12] R. Barbieri, *et al.,* "Z Physics at LEP 1", edited by G. Altarelli *et al.,* CERN
        89-08, Vol. 3, (1989) 137;
        J. Ellis *et al.,* Phys. Lett. **132B** (1983) 437.

[2-13] R. Barbieri,Il Nuovo Cimento **2** (1988) 16;
        R. Barbieri, S. Ferrara and C. Savoy, Phys. Lett. **119B** (1982) 343;
        A. Chamseddine, R. Arnowitt and P. Nath, Phys. Rev. Lett. **49** (1982) 970;
        H. Nilles, Phys. Lett. **115B** (1982) 193;
        L. Ibanez, Phys. Lett. **118B** (1982) 73;
        H. Nilles, Phys. Rep. **110** (1984) 1.

[2-14] R. Barbieri,Il Nuovo Cimento **2** (1988) 18.

[2-15] R. Barbieri,Il Nuovo Cimento **2** (1988) 18;
        R. Barbieri *et al.,* "Z Physics at LEP 1", edited by G. Altarelli *et al.,* CERN
        89-08, Vol. 3, (1989) 127-128.

[2-16] R. Barbieri,Il Nuovo Cimento **2** (1988) 18;
K. Inoue *et al.,* Prog. Theor. Phys., **68** (1982) 927;
J. Ellis, D. Nanopoulos and K. Tamvakis, Phys. Lett. **121B** (1983) 123;
L. Alvarez-Gaumé, J. Polchinsky and M. Wise, Phys. Lett. **221B** (1983) 495;
C. Kounnas *et al.,* Phys. Lett. **132B** (1983) 95;
L. Ibanez, Nucl. Phys. **218B** (1983) 514;
L. Ibanez and C. Lopez, Phys. Lett. **126B** (1983) 54;
L. Ibanez, C. Lopez and C. Munoz, Nucl. Phys. **256B** (1985) 218.

[2-17] OPAL Collaboration, M Akrawy *et al.,* Phys. Lett. **B 248** (1990) 211-219.;
R. Barbieri *et al.,* Phys. Lett. **195B** (1987) 500.

[2-18] R. Barbieri *et al.,* "Z Physics at LEP 1", edited by G. Altarelli *et al.,* CERN
89-08, Vol. 3, (1989) 136-138.

[2-19] ALEPH Collab. D. Decamp *et al.,* "Searches for New Particles in Z Decays
Using the ALEPH Detector", CERN-PPE/91-149, September 1991, submitted
to Phys.Reports.

[3-1] LEP Design Report, Vol. I II, CERN-LEP/84-01, June 1984.

[3-2] Ian Wilson and Heino Henke, "The LEP Main Ring Accelerating Structure",
CERN 89-09 (1989).

[3-3] L3 Collaboration (O. Adriani *et al.*), "Results from the L3 Experiment at
LEP", Physics Reports (236) 1,2 (1993).

[3-4] The Working Group on LEP Energy (L. Arnaudon *et al.*) "Measurement of the
Mass of the Z Boson and the Energy Calibration of LEP", CERN-PPE/93-53
(1993).

[4-1] L3 Collaboration, B. Adeva *et al.,* "The Construction of the L3 Experiment",
NIM A 289 (1990) 35, and the references therein.
L3 Technical Proposal to CERN-LEPC (May 1983).

[4-2] ALEPH Collab. D. Decamp *et al.,* "ALEPH: A Detector for Electron-Positron
Annihilations at LEP", **NIM A 294** (1990) 121;
DELPHI Collab. P. Aarnio *et al.,* "The DELPHI Detector at LEP", **NIM A
303** (1991) 233;
OPAL Collab. M.Z.Akrawy *et al.,* "The OPAL Detector at LEP", **NIM A
305** (1991) 275.

[4-3] The L3 SMD Collab. M.Acciarri *et al.,* "The L3 Silicon Microvertex Detector",
CERN-PPE/94-122, July (1994), submitted to NIM A.

[4-4] See Reference [3-3]

[4-5] J.A. Bakken *et al.,* "Performance of A prototype BGO Calorimeter in An Electron Beam from 2 to 50 GeV ", **NIM A 254** (1987) 535;
M. Schneegans, "Progress of the L3/BGO Calorimeter", **NIM A 257** (1987) 528.

[4-6] A. Bay *et al.,* "The Xenon Monitor of the L3 Electromagnetic Calorimeter", Preprint UGVA-DPNC 1992/01-150, University of Geneva, 1992, submitted to Nucl.Instrum. Meth.

[4-7] S. Burov *et al.,* CERN-EP/88-84, March (1988), submitted to NIM.

[4-8] B. Adeva *et al.,* "Muon Detection in the L3 Experiment at LEP", **NIM A 277** (1989) 187;
Y. Peng, "The Muon Spectrometer of the L3 Detector at LEP", thesis, Univ. of Amsterdam (1988);
J. Onvlee, "The Behaviour of the L3 Muon Chambers in a Magnetic Field", thesis, Univ. of Amsterdam (1989).

[4-9] R. Bizzarri *et al.,* **NIM A 283** (1989) 799;
M. Fukushima, "L3 Level-1 Muon Trigger", L3 notes # 515 (1987);
T.S. Dai and M. Fukushima, "Level 1 Muon Trigger Schematics" L3 notes # 668, May (1989);
J. Perrier, "Level 1 TEC Trigger" L3 notes # 622, Nov. (1988);
M. Bourquin *et al.,* **NIM A 306** (1991) 151.

[5-1] L3 Collab. M. Acciarri *et al.,* "Measurement of Cross Sections and Leptonic Forward-Backward Asymmetries at the Z Pole
and Determination of Electroweak Parameters" **Z.Phys.C 62** (1994) 551-573;
L3 Collab., B. Adeva *et al.,* Z. Phys. **C 51** (1991) 179.

[5-2] T.S. Dai, "Heavy Flavor Production in Z^0 Decays", Ph.D Thesis, MIT (1991), unpublished.

[5-3] T. Foreman, "Bottom Quark Production at the Z Resonance", Ph.D Thesis, University of Amsterdam (1993), unpublished.

[5-4] O. Adriani *et al.,,* **NIM A 302** (1991) 53.

[6-1] T. Sjöstrand, PYTHIA 5.6 and JETSET 7.3, CERN-TH.6488/92 T. Sjöstrand and M. Bengtsson, Comput. Phys. Commun. **43** (1987) 367

[6-2] K. Shultze, R. Starosta, L3 Internal Note 1002 (1991). A. Bartl, H. Fraas, W. Majerotto, Nucl. Phys. B278 (1986) 1; H. E. Haber, D. Wyler, Nucl. Phys. B323 (1989) 267.

[6-3] GEANT Version 3.13, September 1989; See R. Brun *et al.,* GEANT 3, CERN report DD/EE/84-1 (Revised) (Sept. 1987);
H. Fesefeldt, RWTH Aachen Preprint PITHA 85/02 (1985).

[6-4]   L3 Collaboration, B. Adeva *et al.*, Phys. Lett. **B 283** (1992) 454-464.

[6-5]   J. H. Field, Phys. Lett. **B 323** (1994) 432-438.

[6-6]   KORALZ, S. Jadach *et al.*, "Z Physics at LEP 1", edited by G. Altarelli, R. Kleiss and C. Verzegnassi, CERN Report 89-08, Vol.III, 69, to be published in Comp. Phys. Comm..

[6-7]   F.A. Berends, P.H. Daverveldt and R. Kleiss, Nucl. Phys. **B 253** (1985) 441. F.A. Berends, P.H. Daverveldt and R. Kleiss, Comp, Phys. Com. **40** (1986) 285.

[6-8]   L3 Collaboration B. Adeva *et al.*, "Search for Neutralinos with the L3 Detector at LEP", to be submitted to Phys. Lett. B.

[6-9]   M. Sarakinos, private communication.

[7-1]   See Reference [5-1]

[7-2]   See Reference [6-2]

[7-3]   A. Hasan,S. Shevchenko,V.Shoutko and J.Ulbricht, "Search for Neutralinos in Z^0 Decays with the L3 Detector, L3 Internal Note 1594.

[7-4]   See Reference [3-3]

[8-1]   See Reference [2-19]

[8-2]   DELPHI Collab. P. Abreu *et al.*, paper submitted to the XXVI International Conference in High Energy Physics, August 1992, Dallas, Texas, USA.

[8-3]   See Reference [2-17]

[8-4]   S. Myers, ed. 1994 Chamonix Conference on LEP Performance

[8-5]   M. Felcini, talk at Workshop "Ten Years of SUSY Confronting Experiment" , CERN, Geneva, Switzerland, Sept 1992.

[8-6]   J.-F. Grivaz, talk at the INFN Eloisatron Project 23d Workshop,"The Decay Properties of SUSY Particles", Erice, Italy, Oct 1992.